



Universiteit
Leiden
The Netherlands

Geometric phases in soft materials

Abbaszadeh, H.

Citation

Abbaszadeh, H. (2021, January 27). *Geometric phases in soft materials*. *Casimir PhD Series*. Retrieved from <https://hdl.handle.net/1887/139164>

Version: Publisher's Version

License: [Licence agreement concerning inclusion of doctoral thesis in the Institutional Repository of the University of Leiden](#)

Downloaded from: <https://hdl.handle.net/1887/139164>

Note: To cite this publication please use the final published version (if applicable).

Cover Page



Universiteit Leiden



The handle <http://hdl.handle.net/1887/139164> holds various files of this Leiden University dissertation.

Author: Abbaszadeh, H.

Title: Geometric phases in soft materials

Issue date: 2021-01-27

GEOMETRIC PHASES IN SOFT MATERIALS

PROEFSCHRIFT

ter verkrijging van
de graad van Doctor aan de Universiteit Leiden,
op gezag van Rector Magnificus prof. mr. C.J.J.M. Stolker,
volgens besluit van het College van Promoties
te verdedigen op woensdag 27 januari 2021
klokke 16.15 uur

door

HAMED ABBASZADEH
GEBOREN TE AMOL, IRAN IN 1991

PROMOTORES:

prof. dr. V. Vitelli (University of Chicago, USA)
prof. dr. ir. W. van Saarloos

PROMOTIECOMMISSIE:

dr. A. Souslov (University of Bath, UK)
dr. J. van Wezel (University of Amsterdam)
prof. dr. A. Achúcarro
prof. dr. C. W. J. Beenakker
prof. dr. E. R. Eliel

Casimir PhD Series, Leiden–Delft, 2020–38

ISBN 978-90-8593-462-2

This thesis will be made available in electronic form at the Leiden University repository located at: <https://openaccess.leidenuniv.nl>.

The research done for this thesis was mostly conducted at the Lorentz Institute for theoretical physics, Leiden University, the Netherlands, and is financed by the Netherlands Organisation for Scientific Research (NWO).

The cover shows a domain between order and disorder. According to Daoist philosophy, happiness lays at the border between yin and yang, or order and chaos. A topological mode ought to stay at this border, even when it faces perturbations in the boundary between the domains.

To my family and Hamraz

Contents

1	Introduction	1
1.1	Adiabatic theorem and the Berry phase	3
1.1.1	Topology and geometric phases	4
1.2	Geometric phases in classical systems	6
1.3	This thesis	9
2	Sonic Landau levels and synthetic gauge fields in mechanical metamaterials	13
2.1	Mechanical graphene	14
2.2	Synthetic gauge field	17
2.3	Mechanical Landau levels	19
2.4	Sublattice-polarized domain wall modes	21
2.4.1	Connection to the Jackiw-Rebbi model	23
2.4.2	Topological robustness of the domain-wall mode	23
2.5	Selective enhancement	28
2.6	Towards mechanical lasers	31
2.7	Conclusion	32
3	Photonic waveguides in liquid crystals	33
3.1	Paraxial light propagation in uniaxial media	35
3.1.1	Large birefringent medium: interaction picture	36
3.2	Guiding regimes for light in a uniaxial medium	38
3.3	Curved waveguides	41
3.4	Fully rotating nematic waveguides	43
3.5	Appendix	46
3.5.1	Dynamics of circularly polarized waves through a uniform uniaxial medium	46
3.5.2	Dynamics of paraxial light propagation in liquid crystals with medium to low birefringence	48

3.5.3	Floquet theory for a periodically driven system	50
4	Liquid-crystal-based photonic topological insulators	55
4.1	Coupled liquid crystal waveguides	56
4.2	Photonic crystals in 1+1d: SSH chain	58
4.3	Symmetries and topological modes in 2+1d	60
4.4	Non-Hermitian description of shifted waveguides	64
4.5	Conclusion	66
4.6	Appendix	67
4.6.1	Liquid crystal configuration	67
4.6.2	Floquet tight-binding model	68
4.6.3	Time-reversal symmetry	69
4.6.4	Why is C_3 -symmetry breaking needed?	73
5	Edge modes in rotating Rayleigh-Bénard systems	77
5.1	Model equations	80
5.1.1	Symmetries of the Rayleigh-Bénard system	81
5.1.2	Simulations of the generalized Swift-Hohenberg equations	83
5.2	Linear dispersion relation	83
5.2.1	Fourier response and edge modes in 1d Swift-Hohenberg model	85
5.3	Nonlinear amplitude equations and system's discretization	88
5.4	Band structure and topology of nonlinear systems	90
5.5	Discussion and outlook	92
5.6	Appendix	93
5.6.1	Band structure of nonlinear Schrödinger/Gross-Pitaevskii equations	93
5.6.2	A nonlinear SSH chain	95
	References	97
	Summary	117
	Samenvatting	119
	List of publications	121
	Curriculum vitae	123

Contents

iii

Acknowledgments 125

This page intentionally left blank.

Chapter 1.

Introduction



Geometric phases are *extra* phase factors (additional to the dynamical ones, i.e. integral of system's energy over time), that are acquired by moving along a closed -adiabatic- path [147, 161] in the parametric space of a given Hamiltonian. The use of the term geometric here stems from the fact that this phase depends on the path taken in the phase space, and not for example on the rate of moving along that path. Consider for example the quantum mechanical wavefunction of an electron which is described in terms of an amplitude a and a phase ϕ as $\psi(\mathbf{r}) = ae^{i\phi}$. After switching on a magnetic field, the electron's wavefunction is modified into $\psi(\mathbf{r}) = ae^{i\phi - ie\mathbf{A}\cdot\mathbf{r}}$, where e is the electrical charge, and \mathbf{A} is the vector gauge field. (Throughout this thesis we set $\hbar = 1$.) Now, consider the movement of this electron on a cyclic path in space, denoted by \mathcal{C} : while the amplitude remains intact, the wavefunction acquires a phase

$$\Phi = -e \oint_{\mathcal{C}} \mathbf{A} \cdot d\mathbf{r}, \quad (1.1)$$

which is equal to the total magnetic flux inside the region that is enclosed by \mathcal{C} . This effect is independent of whether the electron experiences the magnetic field directly, especially when the magnetic field is confined in a region, this phase is independent of the path taken by the electron surrounding that region. This fundamental feature of quantum mechanics is the essence of the Aharonov-Bohm effect [185], see Fig. 1.1(a).

The notion of geometric phases was independently developed in the context of electromagnetic waves by Pancharatnam [186] and in the adiabatic Hamiltonian evolution in quantum mechanical systems by Berry [155, 161] as a more general concept. Later on, Hannay used the same mathematical

concept for classical systems [160]. The Hannay angle, which is the geometric phase that, for instance, makes the Foucault pendulum precess, is an example of how a geometric concept in quantum mechanics can lead to a new frame of looking at a classical problem. One of the tasks of this thesis is to follow a similar passage by adopting an already existing concept (usually formulated in an electronic or cold atom language) to a classical, soft matter platform.

When considering the broadness of a subject and its applicability, Berry's formulation of the quantum adiabatic phase has proven to be a very fruitful discovery of theoretical physics in the past few decades. The range of phenomena that involves this phase spans from the quantum Hall effect [153, 157, 166, 169, 170] and topological insulators [96, 100] to classical mechanics [159, 160], to optical fibers [134, 155, 186], and the rotation of a cat when falling from a height [148]. The geometrical phases are usually measured through interference experiments: the geometrical phases that are acquired by a wavefunction are different when moving along different paths in the parametric space. In the example above, this was done by the interferometry between the electrons that traverse different paths [183, 185].

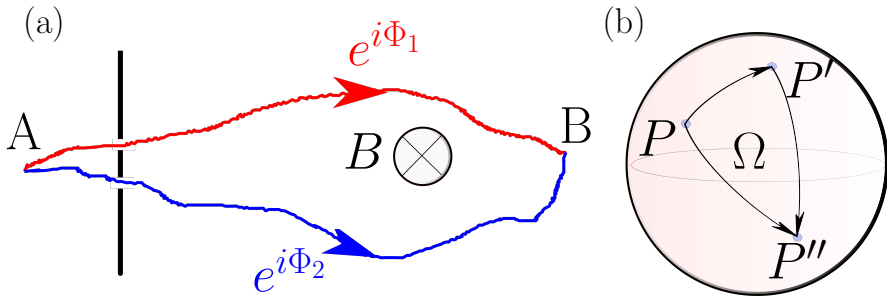


Figure 1.1: (a) The Aharonov-Bohm effect. An electron acquires different phases when its quantum mechanical paths encircle a region that contains a magnetic field. The phase difference $\Phi = \Phi_1 - \Phi_2$ is equal to the total magnetic flux multiplied by electron's electric charge and is unchanged under the smooth deformations of the paths. (b) Light polarization represented on a Poincaré sphere. Similar to the Aharonov-Bohm effect for electrons, the change in the polarization is non-transitive and after traversing a loop, the light beam acquires a geometrical Pancharatnam-Berry phase equal to $\Omega/2$, where Ω is the solid angle that is enclosed by this loop on the Poincaré sphere.

We shall now review the Berry phase and its relation to the field of topological insulators among other applications.

1.1 Adiabatic theorem and the Berry phase

In quantum mechanics, where the dynamics of a system's wavefunction is described by the Schrödinger equation,

$$i\partial_t |\psi\rangle = H |\psi\rangle, \quad (1.2)$$

the adiabatic theorem states that a system that is in one of its eigenstates continues to stay in that state as long as the changes in the Hamiltonian occur slowly enough compared to the energy gap between the corresponding eigenenergy of this state and the rest of the spectrum [45]. Let us then consider the case of a Hamiltonian that evolves along a cyclic adiabatic path in a parameter space, that we represent by a vector $\boldsymbol{\lambda}(t)$ [♣]. The adiabatic theorem above ensures that upon completion of a loop in this parametric space, the system will be in the same quantum eigenstate as the one it started from. This can be represented as $\psi_n(t) = e^{i\gamma_n} \psi_n(t_0)$, where γ_n is a phase that is acquired along the evolution, n denotes the eigenstate index, and t_0 and t are the initial and final time.

Berry showed that apart from a trivial dynamical contribution

$$\gamma_{\text{dyn}} = - \int_{t_0}^t \nabla_{\boldsymbol{\lambda}} E_n(\boldsymbol{\lambda}(t)) \cdot \frac{d\boldsymbol{\lambda}}{dt} dt, \quad (1.3)$$

the phase γ_n has a second nontrivial part that is related to the geometric features of the cyclic path of the Hamiltonian in the parameter space. The Berry phase is defined by

$$\gamma_{\text{geom}} = - \oint_{\mathcal{C}_{\boldsymbol{\lambda}}} \mathcal{A}_n(\boldsymbol{\lambda}(t)) \cdot d\boldsymbol{\lambda} \quad (1.4)$$

as the integrand of the Berry connection

$$\mathcal{A}_n(\boldsymbol{\lambda}) = -i \langle \psi_n(\boldsymbol{\lambda}) | \nabla_{\boldsymbol{\lambda}} | \psi_n(\boldsymbol{\lambda}) \rangle \quad (1.5)$$

over the cyclic path $\mathcal{C}_{\boldsymbol{\lambda}}$ in parameter space. Note the resemblance between this definition and Eq. 1.1. In fact, this similarity in the structure is not accidental, but rather suggests that the Berry connection stems from a gauge freedom [152] that is arising from the invariance of a theory under a gauge transformation $|\psi\rangle \rightarrow e^{i\alpha(\boldsymbol{\lambda})} |\psi\rangle$. Here, such a transformation leads to $\mathcal{A}_n(\boldsymbol{\lambda}) \rightarrow$

[♣]These control parameters are usually tuned through an external mechanism, such as by inducing an electromagnetic field, or shining light to the system. As we will see later on, it can also represent the Bloch momentum in the Fourier space.

$\mathcal{A}_n(\boldsymbol{\lambda}) + \nabla_{\boldsymbol{\lambda}}\alpha$ and, therefore, the loop integral in Eq. 1.4 is invariant under this transformation using the Stokes' theorem:

$$\gamma_{\text{geom}} = - \int_{\mathcal{S}} \mathcal{F} d^2\boldsymbol{\lambda}, \quad (1.6)$$

where $\mathcal{F}_{ij} = \frac{\partial \mathcal{A}_i}{\partial \lambda^j} - \frac{\partial \mathcal{A}_j}{\partial \lambda^i}$ is called the Berry curvature and \mathcal{S} is the interior region of $\mathcal{C}_{\boldsymbol{\lambda}}$ in the parameter space. (We dropped the state index n for the sake of simple notations.) There is a fundamental difference between γ_{dyn} and γ_{geom} . The former is rate dependent: one can stay at the same point in the parameter space and still acquire a dynamical phase, whereas the adiabatic phase is merely determined by the geometrical structure of the eigenmodes associated with the loop $\mathcal{C}_{\boldsymbol{\lambda}}$.

1.1.1 Topology and geometric phases

We saw above that the adiabatic phase has a geometric nature. For example, when measured *locally* (by narrowing down the loop so that \mathcal{S} is an infinitesimally small region in the parameter space), it can determine the Berry curvature on a smooth manifold. This phase is an example of a more general differential geometry concept called holonomy [167]. Let us see how this works in a real-life situation. Consider the cyclic path of a motorcycle on a wall of death in such a way that the initial and final positions coincide. It is then imaginable that the initial and final states of the motorcycle plus the cyclist are the same, except maybe some effects of time-dependent dynamical nature (the petroleum level being reduced, internal states of the cyclist and the motorcycle is changed, etc.). Note also that this lack of the geometric phase does not also depend on the path taken between the initial and final points. Now, imagine this experiment is done on a Möbius strip, as shown in Fig. 1.2(c) ♣. We can see that this time the final state of the motorcycle and the cyclist is flipped with respect to their initial state by gaining a geometric phase π . Again, this geometric phase is independent from the intermediate path that is taken between the initial and final points.

This is an example of a holonomy that is dependent on a *global* geometric character of a manifold that is determined by its topology. To affect such topological characteristics, one needs to consider discontinuous changes in the shape of the manifold, such as the one is shown by Fig. 1.2(b).

♣ This is not recommended in a real world situation, since some positive curvature is in play!

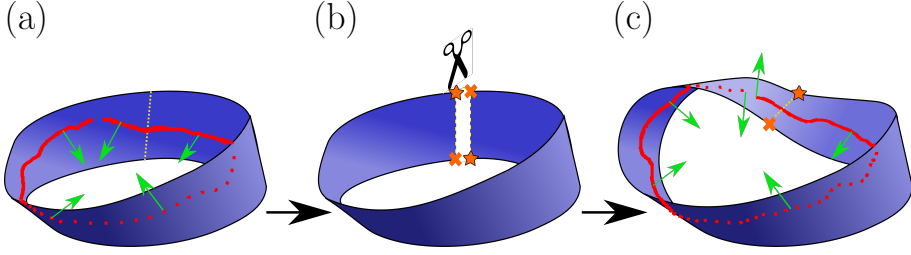


Figure 1.2: A Möbius strip can be obtained from a cylindrical object by a non-continuous deformation, as in (b). The difference between topology of the initial, (a), and final, (c), objects can be shown by tracking a director field on a loop and find the difference in its orientation between the initial and final states.

A fruitful result of Berry's geometric phases was its role in the development of topological modes which led to an explanation of the quantized Hall conductance in the quantum Hall effect [170]. While discussing this connection in full detail and in its rigorous mathematical formalism is beyond the scope of this introduction, it is worthwhile to see how this fascinating subject of modern physics was rooted in the geometric phases which we discussed above.

Let us consider a general Hamiltonian that is invariant under a translation operator. The eigenmodes of such a Hamiltonian will be Bloch waves $\psi_k(x) = u(x)e^{ikx}$, where $u(x)$ is a periodic function and k is a wavenumber that belongs to a periodic region in the reciprocal space that is called the first Brillouin zone (BZ). The eigenenergies of the system can be derived by diagonalizing the Fourier transformed Hamiltonian $H(k)$ for each wavenumber. This calculation results in a set of continuous bands of energies in the BZ, constructing the band structure of H . This procedure can be formulated as below: For each Hamiltonian $H(x)$ on a periodic boundary condition, there exists a set of Fourier transformed (Bloch) Hamiltonians $H(k)$ that are parametrized by a wavenumber $k \in 1^{st}$ BZ. Hence, if the band structure of H is gapped, one can apply the adiabatic theorem to calculate the Berry phase of the n th band on the momentum space

$$\gamma_n = i \oint_{1^{st} \text{ BZ}} \langle \psi_n(\mathbf{k}) | \nabla_{\mathbf{k}} | \psi_n(\mathbf{k}) \rangle \cdot d\mathbf{k} \quad (1.7)$$

where $|\psi_n(\mathbf{k}; t)\rangle$ is the n -th eigenstate of the Hamiltonian and \mathbf{k} is the adiabatic parameter. The integral in the right hand side is related by Stoke's theorem to the integral of the Berry curvature, $\mathcal{F} = \nabla \times \mathcal{A}$, where \mathcal{A} is the Berry connection, as defined by Eq. 1.5 in the reciprocal space. The later integral is related to the first Chern number through [187]

$$C = \frac{1}{2\pi} \int \mathcal{F} d^2\mathbf{k}, \quad (1.8)$$

which is an integer number and is the one that was used by TKNN [169] to explain the quantization of the quantum Hall conductivity which was observed by von Klitzing [170] ♣.

1.2 Geometric phases in classical systems

Geometric phases are not quantum effects. Hannay formulated them in the context of classical Hamiltonian systems [150, 160]. For example, such geometric phases lead to the precession of a pendulum in a rotating frame. Another example is in the context of light polarization dynamics, which was discovered by Pancharatnam a few decades before Berry's adiabatic phase. A monochromatic light wave with a wavevector \mathbf{k} and frequency ω that travels along a fixed direction acquires a dynamical phase

$$\Phi_{\text{dyn}} = e^{i\mathbf{k}\cdot\mathbf{r} - i\omega t}. \quad (1.9)$$

However, this contribution does not consider a polarization degree of freedom which adds a vectorial nature to the state of the light wavepacket, for example when it passes through a polarizer. The polarization can be represented by a complex vector on a Poincaré (or Bloch) 2-sphere. Passing through a polarizer, which we show by $[P \rightarrow P']$ in the example above is then represented by a geodesic path between two polarization states on the Poincaré sphere, as shown by Fig. 1.1(b).

Pancharatnam showed that such phases acquired by the light beam are non-transitive, i.e. $[P \rightarrow P'] \cup [P' \rightarrow P''] \neq [P \rightarrow P'']$ and the difference is given by the half of the solid angle of the closed loop between these three points [186], namely

$$\Phi_{\text{geom}} = \frac{1}{2} \Omega_{PP'P''}, \quad (1.10)$$

♣Notice that this sentence is describing two Nobel physics prizes!

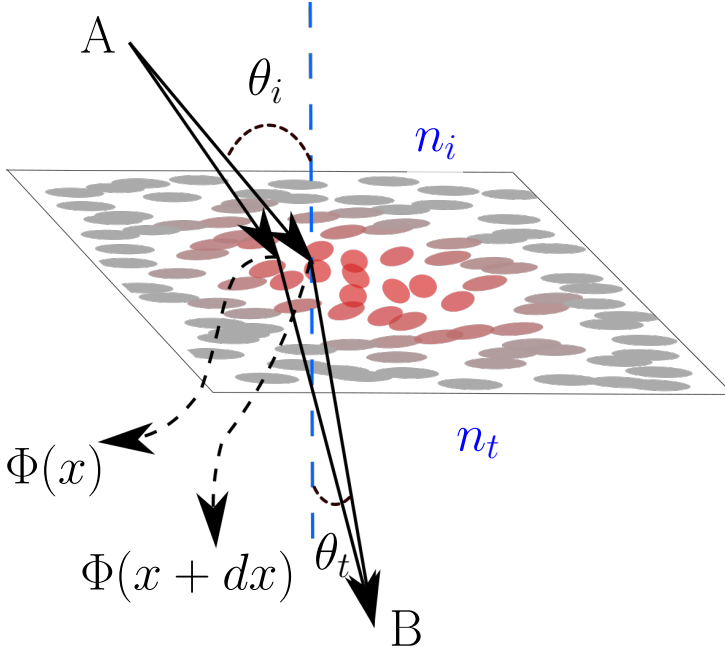


Figure 1.3: Generalized Snell's law, after Ref. [98].

see Fig. 1.1(b). Once again, it is important to note that this phase is not the same as the regular dynamical phase that the light beam acquires along its evolution. Rather, it is an extra phase that is merely determined by the geometry of the path that is taken by the polarization state of light on the Poincaré sphere. This phase is equivalent to the adiabatic phase on the Bloch sphere of an electron in a magnetic field, similar to the Aharonov-Bohm experiment [155]. This means that the Pancharatnam phase regards the light polarization state as a spin-1/2 particle, in contrast to the photon's spin-1, which for example is relevant in spin-orbit interaction of light with a non-straight pathway in space [60, 110, 111]. These non-straight pathways lead to a different geometric phase due to the change in light's momentum direction that was studied by Rytov and Vladimirskii [188, 189]. In this thesis, we will use the terms Pancharatnam-Berry phase and Rytov-Vladimirskii-Berry phase to refer to these two different geometric phases of the light beams.

As an example of the effects of the geometric phases on physical observables, we here review the effect of the Pancharatnam-Berry phase on the refraction of light. A Pancharatnam-Berry phase, unlike the dynamical or Rytov-Vladimirskii-Berry phase is independent from the spatial path that is traversed by light. Therefore, it can change abruptly on a subwavelength scale in space. To illustrate this, let us consider a two-dimensional liquid-crystalline metasurface that acts as a polarizer on an incident light beam that travels between two regions with different refractive indices, as shown in Fig. 1.3. A spatial inhomogeneity on the orientation of the liquid crystal molecules then leads to a spatial variation in the induced Pancharatnam-Berry phase of the incident light beam. The effective optical path between two points A and B is then obtained by $L_{\text{opt}} = \int_A^B \mathbf{k}(\mathbf{r}) \cdot d\mathbf{r} + \Phi_{r_s}$, where the wavevector \mathbf{k} is spatially dependent on the media's refractive index and Φ_{r_s} is the geometric phase that the light acquires at the incident point r_s to the metasurface. To find the classical path of the light beam one uses Fermat's principle, which can be stated as $\delta L_{\text{opt}} = 0$ with respect to the variations around this classical path. For the situation that is depicted in Fig. 1.3, this leads to the generalized Snell's law of refraction given by [98]

$$k_0 [n_t \sin \theta_t - n_i \sin \theta_i] = \partial_x \Phi. \quad (1.11)$$

Thus, a spatial change in the geometric phase can affect the refraction of light in a medium. For a Pancharatnam-Berry geometric phase, this effect can take place on a subwavelength scale.

Additional to various examples of geometric phases in classical models, the topological concepts are also well-known in these systems. Liquid crystal disclinations are singularities around which a parallel transport of the director field yields a $\pm\pi$ phase regardless of the path that is taken around them, similar to what happens in the Möbius strip example above. These are examples of topological defects [127, 171]. Such defects also appear in lines of curvature around a degenerate umbilical point on curved surfaces [173], and crystalline defects in solids and mechanical systems [138].

Interestingly, topology in the sense of topological states in integer quantum Hall effect is also found in classical models. The crosspoint lies at the concept of band topology: waves in classical systems, such as light waves in photonic crystals or phonon modes in mechanical systems, have a dispersion relation associated to them, similar to quantum band structure of solids [114, 136]. Thus, one can imagine Chern numbers are being calculated for isolated bands in these wave dispersions as well [82, 109, 113, 115].

1.3 This thesis

We will discuss in this thesis topology and geometric phases of the phonon modes in a metamaterial, the photonic states in an artificial lattice in liquid crystals, and hydrodynamic instabilities in a rotating Rayleigh-Bénard cell.

In chapter two, we consider phonon modes of an elastic metamaterial. For this we consider a simplified model of beads and springs [109]. The vibrational modes of this system are obtained by analysing its linear response around the equilibrium state. It is then possible to start from the Newton's second law for each bead and write down $m\ddot{\mathbf{u}} = D\mathbf{u}$, where D is the dynamical matrix, m is the bead's mass, and \mathbf{u} is the bead's displacement from the equilibrium state. Inspired by Dirac's derivation of the Klein-Gordon equations [193], Kane and Lubensky argued in 2014 in an influential paper that one can take the square root of this equation to get to a Schrodinger equation with a Hamiltonian that is given by [82]

$$H = \begin{pmatrix} 0 & Q \\ Q^T & 0 \end{pmatrix}, \quad (1.12)$$

where Q is called the equilibrium matrix that relates the force applied on the bead i to the spring tensions through [66]

$$F_i = Q_{im}T_m. \quad (1.13)$$

It is then possible to relate the phonon dispersion of the system to the band structure of the Hamiltonian H . In this chapter, we use this connection to quantum mechanics to design a mechanical metamaterial which has a Dirac cone in its band structure. We find an equivalent to a vector potential for the phonon modes that minimally couples to their momentum around the Dirac points in the BZ by applying strain or a variation of the material's local stiffness. We further find the phenomena associated with the presence of this synthetic gauge field, such as Landau levels for sound. We then find that the zeroth Landau level of this system is a specific case of a more general Jackiw-Rebbi-type topological zero mode in our model and define a sublattice polarization to connect our system to this model.

In the third chapter, we consider the propagation of a monochromatic light wave in a liquid crystal medium. Starting from Maxwell's equation, one can derive the Helmholtz wave equations for the electromagnetic wavefunction, considering a transverse electromagnetic (TEM) wave, $\psi = (E_x, E_y)$ as

$$\frac{\partial^2}{\partial z^2}\psi = -(\nabla_{\perp}^2 + k_0^2\epsilon)\psi, \quad (1.14)$$

where k_0 is the wavenumber in the free space, ∇_{\perp} is the spatial gradient in the transverse plane, and ϵ is the dielectric tensor of the host material. In a so-called paraxial regime, the wave equation above becomes first order along the propagation direction, z and the equation of motion for a monochromatic electromagnetic wave is cast as

$$i\partial_z\psi = -\frac{1}{2nk_0}\nabla_{\perp}^2\psi - V[\epsilon]\psi, \quad (1.15)$$

where n is the average refractive index, and $V[\epsilon]$ is an effective photonic potential due to the dielectric medium [104, 108]. It then becomes possible to look at the system in this regime as a quantum mechanical problem. In the liquid crystal system that we consider, when the director field's variation in the perpendicular plane is slow, the system is in the paraxial regime. A periodic modulation of the liquid crystal pattern will then map this system to a quantum mechanical problem with a time-periodic Hamiltonian that are studied with Floquet theory [61, 79]. We then show that such Floquet Hamiltonians, when the director field varies adiabatically, can induce Pancharatnam-Berry phases for a light beam. As a result of such spatially varying geometric phase, the light beam becomes transversely confined, leading to *soft light waveguides*. We then use the tools of Floquet theory to obtain the guided modes for more general nematic textures.

In the fourth chapter, we couple these soft electromagnetic waveguides to each other. We show that coupling between these waveguides, also known as coupled mode approximation in optical systems, follow the rules of a semi-classical tunneling picture, establishing an analogy with quantum mechanics in a many-waveguide level. We then develop a tight-binding model for these waveguide interactions. As a result of this model, we present two archetypal example of topological photonics to be realized in liquid crystals: a 1d SSH chain [172] and a 2d Haldane model [151]. Along the way, we develop two recipes to break the effective time-reversal symmetry by merely using the structural degree of freedom. Another result of this chapter is to have a system which has two different kinds of geometric phases: a Pancharatnam-Berry phase to achieve single waveguides and a Berry geometric phase corresponding to the topological band structure.

In the fifth chapter, we consider a rotating Rayleigh-Bénard convection cell. This time, instead of oscillatory waves we consider growing hydrodynamic instabilities that form patterns in this system. The evolution of such a system is described by a nonlinear, but deterministic set of partial differential

equations [140] such as the Swift-Hohenberg model [174]. Formally, such system can be effectively described by

$$\partial_t \psi = \mathcal{N}[\psi], \quad (1.16)$$

where \mathcal{N} is a nonlinear operator and ψ is system's state function. We will focus on the regimes that the final state of the system is a steady-state ordered pattern. The linear stability analysis around this steady state leads to a complex band structure where the real part is the growth rate and the imaginary part is the frequency of the hydrodynamic modes. We apply the insights discussed above to characterize the topology of these bands. In a separate attempt, we then try to sketch a proposal to apply nonlinear geometric phases [10] for studying patterns close to the threshold of the instability transition in this system, where one can use a perturbative method, that is called the amplitude equations approach, to simplify the full nonlinear equations.

Chapter 2.

Sonic Landau levels and synthetic gauge fields in mechanical metamaterials



Electronic systems subject to a uniform magnetic field experience a wealth of fascinating phenomena such as topological states [122] in the integer quantum Hall effect [100] and anyons associated with the fractional quantum Hall effect [123]. Recently, it has been shown that in a strained graphene sheet, electrons experience external potentials that can mimic the effects of a magnetic field, which results in the formation of Landau levels and edge states [99, 101]. Working in direct analogy with this electronic setting, pseudo-magnetic fields have been engineered by arranging CO molecules on a gold surface [92] and in photonic honeycomb-lattice metamaterials [88, 89].

In this chapter, we apply insights about wave propagation in the presence of a gauge field to acoustic phenomena in a nonuniform phononic crystal, using the appropriate mechanisms of strain-phonon coupling and frictional dissipation, in contrast to those present in electronic and photonic cases. The acoustic metamaterial context in which we implement gauge fields provides us with significant control [30, 90, 97] over frequency, wavelength, and attenuation scales unavailable in the analogous electronic realizations. For example, a metamaterial composed of stiff (e.g. metallic) components of micron-scale length may be suitable for control over ultrasound with gigahertz-scale frequencies, whereas cm-scale metamaterials may provide control over kHz-scale sound waves. We develop two strategies for realizing a uniform pseudo-magnetic field in a metamaterial based on the honeycomb lattice, i.e. “mechanical graphene” [63]. In the first strategy, we apply stress at the boundary to obtain nonuniform strain

in the bulk, which leads to a Landau-level spectrum, whereas in the second strategy, we exploit built-in, nonuniform patterning of the local metamaterial stiffness. This second strategy shows how the unique controllability of metamaterials can lead to novel designs inaccessible in the electronic context.

2.1 Mechanical graphene

We begin with a minimal, microscopic model of an acoustic metamaterial – a set of nodes positioned at the vertices of a honeycomb lattice and connected by rods to their nearest neighbors (see Fig. 2.1a) [63]. The compressional stiffness of the rods κ is determined by their fixed Young’s modulus E , variable cross-section area S , and length a via ES/a . We assume the rods to be so slender that their bending stiffness is significantly lower than their compressional stiffness. We model the rods as central-force harmonic springs, whose elastic energy U is given in terms of the strain $\delta r/a$ by $U(\delta r) = \frac{1}{2}\kappa(|\mathbf{r} + \delta\mathbf{r}| - a)^2$. For small strains, this energy can be linearized in terms of node displacements \mathbf{u}_1 and \mathbf{u}_2 as $U(\mathbf{u}_1, \mathbf{u}_2) = \frac{1}{2}\kappa(\mathbf{e} \cdot [\mathbf{u}_1 - \mathbf{u}_2])^2$, where $\mathbf{e} \equiv \mathbf{r}/|\mathbf{r}|$ is the unit vector along the spring. (In Fig. 2.1a, we define the initial configuration for the node positions and stiffnesses.) The total elastic energy associated with a unit cell at spatial point \mathbf{R} can be cast as

$$U_{\text{tot}}(\mathbf{R}) = U_1(\mathbf{R}, \mathbf{R}) + \frac{1}{2} [U_2(\mathbf{R}, \mathbf{R} - \mathbf{a}_1) + U_2(\mathbf{R} + \mathbf{a}_1, \mathbf{R})] + \frac{1}{2} [U_3(\mathbf{R}, \mathbf{R} - \mathbf{a}_2) + U_3(\mathbf{R} + \mathbf{a}_2, \mathbf{R})], \quad (2.1)$$

where by considering $\mathbf{u}_s(\mathbf{R})$ as the displacement of the s sublattice node of the unit cell centered at \mathbf{R} we defined

$$U_\alpha(\mathbf{R}_1, \mathbf{R}_2) = \frac{\kappa}{2} [\mathbf{e}_\alpha \cdot (\mathbf{u}_2(\mathbf{R}_2) - \mathbf{u}_1(\mathbf{R}_1))]^2, \quad (2.2)$$

which gives the potential energy of a single rod in the direction \mathbf{e}_α connecting two unit cells at points \mathbf{R}_1 and \mathbf{R}_2 . Note that we only considered the interaction between nearest neighbors, which guarantees that the interactions are only between the nodes from different sublattices. This consideration will lead to an effective chiral symmetry in this system, which as we will discuss later, will be crucial for the existence of topological sound modes in this setup.

Given this potential, we write down and solve the linear equation of motion for acoustic vibrations of the lattice:

$$-m\ddot{u}_i^\mu = \frac{\partial U}{\partial u_i^\mu} = \sum_{j,\nu} D_{ij}^{\mu\nu} u_j^\nu, \quad (2.3)$$

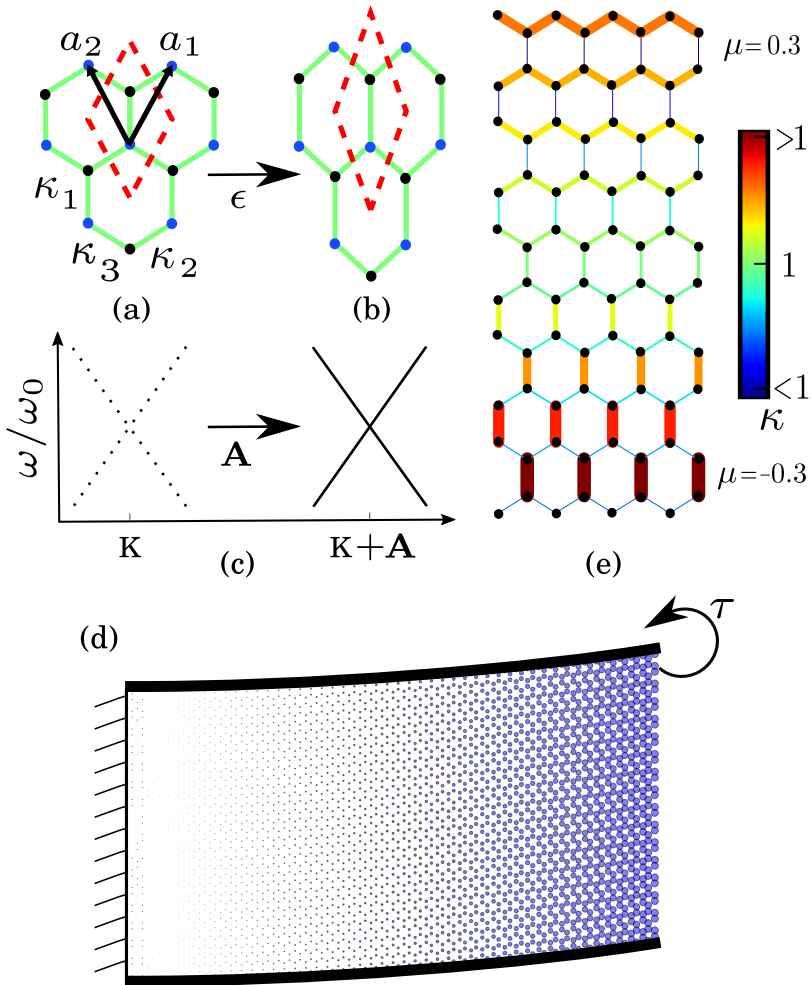


Figure 2.1: (a) Mechanical graphene – a set of rods and nodes based on the honeycomb structure. The dashed line indicates the shape of a unit cell. (b) The lattice with a pure shear strain. (c) The shift of a Dirac point within the phonon spectrum of mechanical graphene due to the applied strain can be used to define an effective vector potential. (d) An externally applied nonuniform pure shear deformation that corresponds to a constant magnetic field. The external stress is applied by a torque τ on the boundary rods. (e) A non-uniform patterning of the local material stiffness that leads to a constant magnetic field. We consider periodic boundary conditions along x and free boundary conditions along y .

where u_i^μ are the $\mu = x, y$ components of displacement of the i th site and $D_{ij}^{\mu\nu}$ are components of the dynamical matrix. In a periodic lattice, the solutions to this equation of motion are plane waves $\mathbf{u}_\mathbf{q} e^{i(\omega(\mathbf{q})t - \mathbf{q} \cdot \mathbf{x})}$, where both the dispersion relation $\omega(\mathbf{q})$ and the normal modes $\mathbf{u}_\mathbf{q}$ are found from the corresponding eigenvalue problem for each wavevector \mathbf{q} :

$$D(\mathbf{q})\mathbf{u}_\mathbf{q} = m\omega^2(\mathbf{q})\mathbf{u}_\mathbf{q}, \quad (2.4)$$

The dynamical matrix of the two-dimensional honeycomb lattice is:

$$D(\mathbf{q}) = \frac{1}{m} \sum_{\alpha=1}^3 \kappa_\alpha \begin{pmatrix} P_\alpha & -P_\alpha e^{i\mathbf{q} \cdot \delta_\alpha} \\ -P_\alpha e^{-i\mathbf{q} \cdot \delta_\alpha} & P_\alpha \end{pmatrix}, \quad (2.5)$$

where the projections $P_\alpha = \mathbf{e}_\alpha \mathbf{e}_\alpha^T$ and for the honeycomb lattice

$$P_1 = \begin{pmatrix} 0 & 0 \\ 0 & 1 \end{pmatrix}; \quad P_2 = \begin{pmatrix} 3/4 & \sqrt{3}/4 \\ \sqrt{3}/4 & 1/4 \end{pmatrix}; \quad P_3 = \begin{pmatrix} 3/4 & -\sqrt{3}/4 \\ -\sqrt{3}/4 & 1/4 \end{pmatrix} \quad (2.6)$$

The phonon dispersion relation $\omega(\mathbf{q})$ of the system can then be obtained from the square root of the eigenvalues of this dynamical matrix. This band structure exhibits a linear dispersion of the phonon modes around the Dirac point K [defined by $\mathbf{q}_K \equiv (0, 4\pi/3\sqrt{3}a)$], where the two middle bands are degenerate. Using first-order perturbation theory around the Dirac point, we find the following form for the dynamical matrix:

$$D(\mathbf{q}_K + \delta\mathbf{q}) \approx \omega_0^2 \begin{pmatrix} 0 & 0 & \frac{a(\delta q_x - i\delta q_y)}{2\sqrt{2}} & \frac{a(\delta q_x + i\delta q_y)}{2\sqrt{2}} \\ 0 & 2 & -\frac{a(\delta q_x - i\delta q_y)}{2\sqrt{2}} & \frac{a(\delta q_x + i\delta q_y)}{2\sqrt{2}} \\ \frac{a(\delta q_x + i\delta q_y)}{2\sqrt{2}} & -\frac{a(\delta q_x + i\delta q_y)}{2\sqrt{2}} & 1 & \frac{a(-\delta q_x - i\delta q_y)}{2} \\ \frac{a(\delta q_x - i\delta q_y)}{2\sqrt{2}} & \frac{a(\delta q_x - i\delta q_y)}{2\sqrt{2}} & \frac{a(-\delta q_x + i\delta q_y)}{2} & 1 \end{pmatrix}, \quad (2.7)$$

where $\omega_0 = \sqrt{3\kappa/2m}$ is the frequency of the degenerate bands at the Dirac point. We can then project the dynamical matrix for the two degenerate bands to get

$$D_r(\mathbf{q}_K + \delta\mathbf{q}) = \omega_0^2 \mathbb{1} - \frac{1}{2} \omega_0^2 a \delta\mathbf{q} \cdot \boldsymbol{\sigma} + \mathcal{O}(\delta\mathbf{q}^2), \quad (2.8)$$

where D_r is the reduced dynamical matrix for the two middle bands, $\mathbb{1}$ is the 2×2 identity matrix, $\delta\mathbf{q} \equiv \mathbf{q} - \mathbf{q}_K$, and $\boldsymbol{\sigma} \equiv (\sigma_x, \sigma_y)$ is composed of Pauli spin matrices

$$\sigma_x = \begin{pmatrix} 0 & 1 \\ 1 & 0 \end{pmatrix} \text{ and } \sigma_y = \begin{pmatrix} 0 & -i \\ i & 0 \end{pmatrix}. \quad (2.9)$$

From this reduced form, one can deduce that small perturbations on this system will lead to the following general form up to the lowest order in perturbation theory[♣]:

$$D_r(\mathbf{q}_K + \delta\mathbf{q}) = -\frac{1}{2}\omega_0^2(a\delta\mathbf{q} + \mathbf{A}) \cdot \boldsymbol{\sigma} + (1 + V)\omega_0^2\mathbb{1} + \mu\sigma_z, \quad (2.10)$$

where a gauge field \mathbf{A} minimally coupled to the momentum of the phonons[♡] and a potential V are introduced as a result. The sublattice breaking term which is proportional to the third Pauli matrix

$$\sigma_z = \begin{pmatrix} 1 & 0 \\ 0 & -1 \end{pmatrix} \quad (2.11)$$

will remain zero, as long as the perturbation does not violate the chiral symmetry. From the structure of Eq. (2.10), we note that the dispersion around \mathbf{q}_K has the form of a Dirac cone.

2.2 Synthetic gauge field

We now proceed to show that unlike uniform lattice deformations that merely shift this Dirac cone in wavevector space, nonuniform deformations can lead to an effective synthetic gauge field for sound. For uniform strain (Fig. 2.1b), \mathbf{A} and V are both constant throughout the lattice. On the other hand, for a nonuniform but slowly varying strain, the position of the local Dirac point varies from one region to another (Fig. 2.1c), which corresponds to fields \mathbf{A} and V that depend on spatial coordinates.

To see this, we consider a general deformation on the honeycomb structure with affine component \mathbf{U} and nonaffine component \mathbf{W} of the displacement denoting, respectively, the common and relative displacements of the two sublattices. The deformation of each sublattice is then given by $\mathbf{U}_{1,2} = \mathbf{U} \pm \mathbf{W}/2$, where the different signs correspond to the different sublattices. This deformation changes the components of the dynamical matrix via $\delta_\alpha \rightarrow \tilde{\delta}_\alpha$ and $P_\alpha \rightarrow \tilde{P}_\alpha$, where

$$\tilde{\delta}_\alpha = (I + \nabla\mathbf{U})\delta_\alpha + \mathbf{W} \quad (2.12)$$

$$\begin{aligned} \tilde{P}_\alpha &= P_\alpha + (\nabla\mathbf{U})P_\alpha + P_\alpha(\nabla\mathbf{U})^T \\ &+ (\mathbf{e}_\alpha^T \epsilon \mathbf{e}_\alpha + \mathbf{e}_\alpha^T \mathbf{W}/a) (I - 3P_\alpha) + \mathbf{e}_\alpha \mathbf{W}^T/a + \mathbf{W} \mathbf{e}_\alpha^T/a, \end{aligned} \quad (2.13)$$

[♣]Here, we use the fact that any general 2×2 Hermitian matrix can be expanded in the $\{\sigma_x, \sigma_y, \sigma_z, \mathbb{1}\}$ basis.

[♡]corresponding to a gauge transformation $u \rightarrow ue^{-i\mathbf{A} \cdot \mathbf{x}/a}$ in the wavefunction

and $(\nabla \mathbf{U})_{ij} = \partial_i U_j$. The potential energy of a single rod can now be expressed as

$$\tilde{U}_\alpha(\mathbf{R}_1, \mathbf{R}_2) = \frac{\kappa}{2} \left(\left| \tilde{\delta}_\alpha + \mathbf{u}_2(\mathbf{R}_2) - \mathbf{u}_1(\mathbf{R}_1) \right| - 1 \right)^2. \quad (2.14)$$

Taking the same steps as before, we find that the lattice deformations modify the dynamical matrix according to

$$\tilde{D}(\mathbf{q}) = \frac{1}{m} \sum_{\alpha=1}^3 \kappa_\alpha \begin{pmatrix} \tilde{P}_\alpha & -\tilde{P}_\alpha e^{i\mathbf{q} \cdot \tilde{\delta}_\alpha} \\ -\tilde{P}_\alpha e^{-i\mathbf{q} \cdot \tilde{\delta}_\alpha} & \tilde{P}_\alpha \end{pmatrix}. \quad (2.15)$$

We then obtain the gauge field

$$\begin{aligned} \mathbf{A}(x, y; \epsilon, W) = & a(\mathbf{q}_K \cdot \nabla) \mathbf{U} + \left[\frac{3}{2}(\epsilon_{xx} - \epsilon_{yy}), -3\epsilon_{xy} \right] \\ & + (W_y, -W_x)/a, \end{aligned} \quad (2.16)$$

and $V = \frac{1}{2} \text{Tr } \epsilon$, where $\epsilon_{ij} \equiv (\partial_i U_j + \partial_j U_i)/2$ is the linear affine strain.

To simplify the design of an acoustic device based on this strained lattice, we now consider those lattice strains that can be obtained by applying forces only on the boundary. Such a configuration requires that the forces in the bulk of the material balance each other. In the material we consider, this force-balance condition is satisfied provided that the nonaffine displacements depend on the affine strain via $W_x = \epsilon_{xy} a$ and $W_y = \frac{1}{2}(\epsilon_{xx} - \epsilon_{yy})a$, which can be obtained by solving the force-balance equation $\delta U_{tot}/\delta \mathbf{W} = 0$ using the total elastic potential energy. Thus, the resulting expression for the gauge field in a boundary-strained material is

$$\mathbf{A}(x, y; \epsilon) = a(\mathbf{q}_K \cdot \nabla) \mathbf{U} + [2(\epsilon_{xx} - \epsilon_{yy}), -4\epsilon_{xy}]. \quad (2.17)$$

For the acoustic systems under study we can also follow a second strategy: patterning the local material stiffness to achieve a spatially dependent gauge field \mathbf{A} . For example, we can smoothly vary the composition or thickness of the rods to change their effective spring constants to $\kappa_i = \kappa + \delta\kappa_i$, where $i = 1 \dots 3$ labels springs in the lattice unit cell. In this case, we find that the gauge field and potential are given by

$$\begin{aligned} \mathbf{A}(x, y; \delta\kappa) = & \left(-\frac{1}{3} \frac{2\delta\kappa_1 + \delta\kappa_2 + \delta\kappa_3}{\kappa}, \frac{\delta\kappa_2 - \delta\kappa_3}{\sqrt{3}\kappa} \right), \\ V = & \frac{\delta\kappa_1 + \delta\kappa_2 + \delta\kappa_3}{3\kappa}. \end{aligned} \quad (2.18)$$

One can then obtain a Landau-level spectrum by selecting \mathbf{A} and V such that (for units in which $a = 1$)

$$\nabla \times \mathbf{A} = B\hat{z} = \text{const}; \quad V = 0. \quad (2.19)$$

For any selection satisfying the conditions of Eqs. (2.19), the dynamical matrix in Eq. (2.10) has the form of the Hamiltonian for a Dirac electron in a plane with a constant magnetic field B applied perpendicular to that plane [163, 165]. Let us now consider two practical solutions to Eqs. (2.19): (i) an externally applied nonuniform pure shear deformation, and (ii) nonuniform patterning of the spring constants along the y -direction.

For case (i), we find the particle displacements throughout the lattice by substituting Eq. (2.17) into Eqs. (2.19) and solving the resulting partial differential equation: $\partial_y U_x + \partial_x U_y = -Bx/2$, with the additional constraint $\partial_x U_x = \partial_y U_y = 0$, which corresponds to nonvolumetric pure shear deformations. The resulting displacements satisfy

$$U_x = 0; \quad U_y = -Bx^2/4. \quad (2.20)$$

Note that for the honeycomb lattice, this condition can be realized using the boundary stresses illustrated in Fig. 2.1d.

For case (ii), we substitute Eqs. (2.18) into Eqs. (2.19) to find the condition

$$\sqrt{3}\partial_x(\delta\kappa_2 - \delta\kappa_3) - \partial_y(\delta\kappa_2 + \delta\kappa_3) = 3\kappa B \quad (2.21)$$

for the spatial dependence of the spring constants. We consider a material uniform along the x -direction. In this case, the condition in Eq. (2.21) is satisfied for spring constants given by

$$\mu \equiv \frac{\delta\kappa_2}{\kappa} = \frac{\delta\kappa_3}{\kappa} = -\frac{\delta\kappa_1}{2\kappa} = \frac{By}{3}, \quad (2.22)$$

which is visualized in Fig. 2.1e.

2.3 Mechanical Landau levels

Now that we have proposed metamaterial architectures that realize the acoustic analog of a constant magnetic field, we go on to explore the physical consequences of this field for sound waves. To proceed, we focus on an architecture that is peculiar to the acoustic context, i.e. we select the realization of a

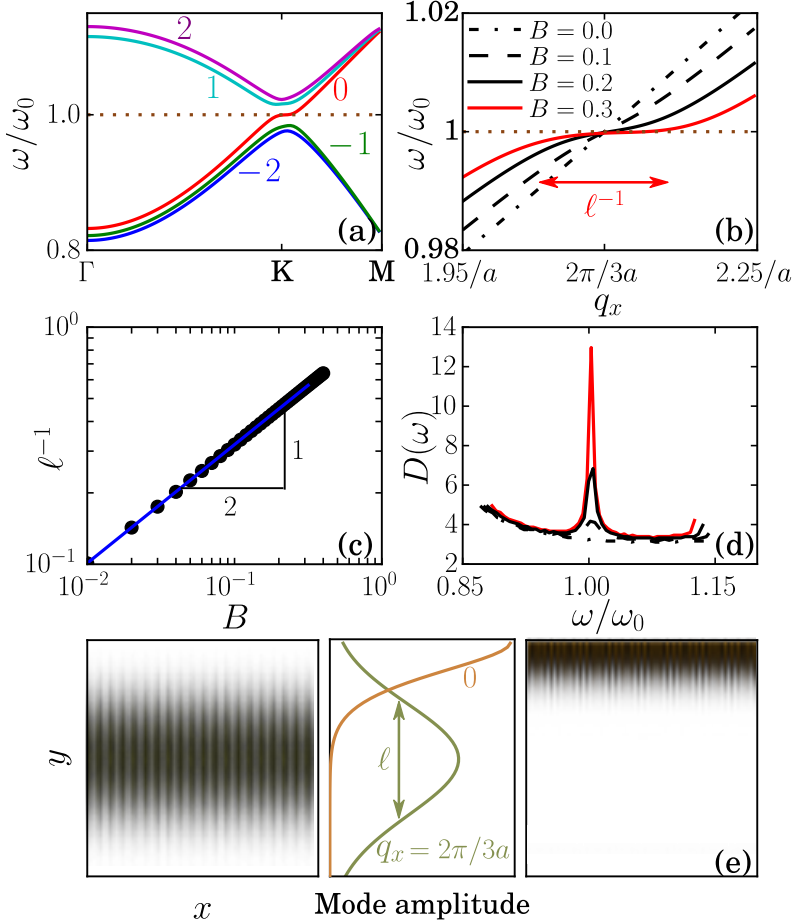


Figure 2.2: Mechanical Landau levels: (a) A pseudo-magnetic field leads to Landau levels around the Dirac point. (b) As the magnetic field increases, the zeroth-Landau-level band flattens. Band flatness can be characterized by the inverse magnetic length ℓ^{-1} . (c) The inverse magnetic length scales as the square root of the magnetic field. (d) Density of states for the zeroth Landau level, for the same values of B as in (b). The peak at the Dirac frequency rises as the bands flatten. (e) Visualizations of the zeroth Landau level at two different wavevectors. For $\mathbf{q} = \mathbf{q}_K$, this mode has a Gaussian profile around the waveguide center, whereas far from this point, at $\mathbf{q} = 0$, the mode decays exponentially away from the edge.

patterned metamaterial waveguide described by Eqs. (2.22). Such a quasi-one-dimensional waveguide is uniform along the x -direction, graded along the y -direction, and is subject to no-stress boundary conditions on its top and bottom (see Fig. 2.1e). The constant pseudo-magnetic field leads to a Landau-level spectrum for frequencies near ω_0 (Fig. 2.2a).

Let us focus on the acoustic band corresponding to the most prominent Landau level: $n = 0$. In Fig. 2.2b, this band is plotted for several values of the pseudo-magnetic field B ; as the pseudo-magnetic field increases, the band flattens over a larger region in wavevector space, which leads to an increasing peak in the density of acoustic states (shown in Fig. 2.2d). The width of this flat region defines an inverse length scale ℓ^{-1} , which scales as $\ell^{-1} \sim \sqrt{B/a}$ (Fig. 2.2c). This length scale is the acoustic analog of the magnetic length of a Landau-level state. Consequently, an acoustic mode in the Landau level has a Gaussian profile with a transverse confinement given by ℓ (Fig. 2.2e). The transverse location of this mode within the waveguide is controlled by the mode wavenumber q_x , in contrast to an index-graded waveguide in which the location is determined by the mode frequency. Consequently, in our case, the location of sound at a targeted frequency can be significantly tuned via the mode wavenumber (Fig. 2.2e and 2.4).

2.4 Sublattice-polarized domain wall modes

The $n = 0$ Landau level at $q_x = q_{K,x} \equiv 2\pi/3a$ has frequency ω_K , is located at the waveguide center, and involves displacements exclusively on one sublattice. Modes with these properties generically appear in regions across which A_x changes sign, i.e. their local dispersions have Dirac cones on opposite sides of point K . As an example, we consider a waveguide with two domain walls that separate a uniform central region with spring constants set by $\mu = -0.08$ from two regions, one above and one below, that each have $\mu = 0.08$ (Fig. 2.3a). At $q_x = q_{K,x}$, the spectrum as a function of q_y near point K is described by a gapped 1D Dirac Hamiltonian centered about ω_K , with effective mass proportional to A_x . The “spin” degree of freedom corresponds to the two sublattices of the honeycomb lattice: eigenstates of σ_z with eigenvalues $+1$ and -1 involve displacements solely on sublattice A and sublattice B, respectively. When the mass $m(y)$ varies spatially, domain walls at which $m(y)$ changes sign harbor exponentially localized midgap modes that are “spin-polarized”, i.e. confined to a single sublattice [172, 175]. The sublattice on which the mode

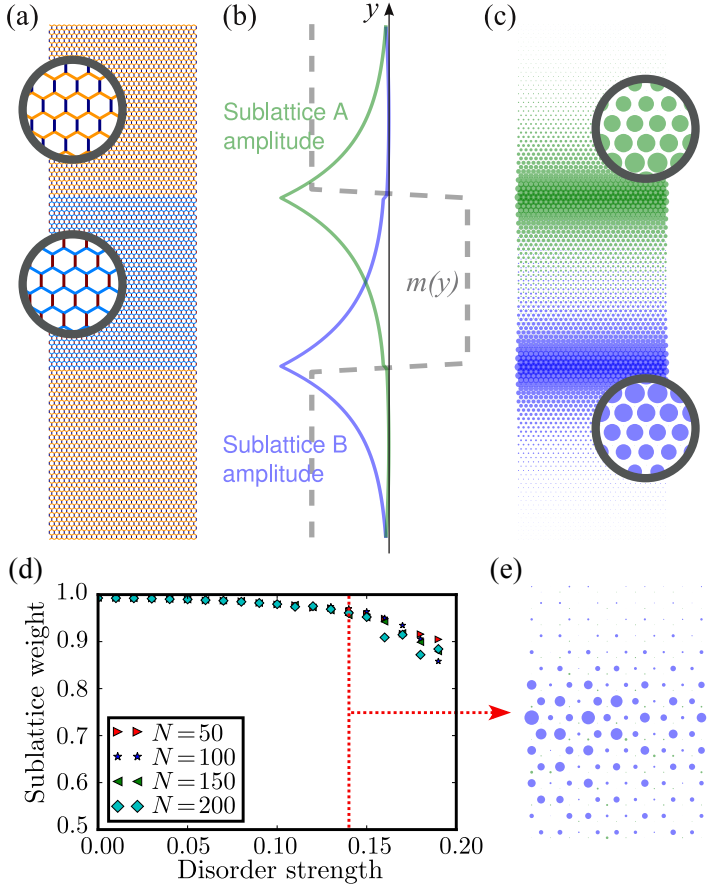


Figure 2.3: (a) Waveguide with two domain walls separating two regions with $\mu = 0.08$ from a central region with $\mu = -0.08$. The bonds are colored according to their spring constants as in Fig. 1(e). Periodic boundary conditions are applied along x . (b) Variation of the effective Dirac mass $m(y)$ (dashed line) and of the amplitude of the midgap mode at $q_x = 2\pi/3a$ on either sublattice (solid lines). (c) Visualization of the midgap mode with the sublattices distinguished. Each point is represented by a disc whose area is proportional to the amplitude of the midgap mode at that point. Points on sublattices A and B are drawn as green and blue discs respectively, showing the strong polarization of each domain wall mode onto a distinct sublattice. (d) The dependence of sublattice polarization of the domain-wall-bound mode on disorder in the spring constants. The polarization remains significant due to the topological origin of the mode (e) Even in the presence of strong (14%) disorder, we clearly observe the sublattice-polarized domain-wall-bound mode.

is localized is determined by the sign of the change in mass upon crossing the domain wall. Fig. 2.3b–c shows the numerically-obtained midgap mode for the domain wall geometry in Fig. 2.3a, whose components on sublattice A (sublattice B) fall off exponentially from the top (bottom) domain wall.

2.4.1 Connection to the Jackiw-Rebbi model

Some of our results for the sublattice-polarized modes can be understood using a connection between mechanical graphene and the Jackiw-Rebbi model [175]. Note that, for the waveguide described above, $\kappa_2 = \kappa_3$ and $V = 0$, which is equivalent to $\delta\kappa_2 = \delta\kappa_3 = -\delta\kappa_1/2 \equiv \kappa\mu$. This case with staggered spring constants along the y -direction is reminiscent of the Su-Schrieffer-Heeger model [172]. Using the formula for the synthetic gauge field in Eq. 2.18, we find the following form for the dynamical matrix:

$$D = D_0 + \frac{1}{3}\omega_0^2\mu(y)\sigma_x. \quad (2.23)$$

Thus, we see that the dimensionless parameter μ plays the role of the effective mass in the Jackiw-Rebbi model. For modes of the honeycomb-lattice waveguide near the Dirac frequency, we can obtain the form of the eigenmodes using the zero mode solution of the Jackiw-Rebbi model: $\mathbf{u}(y) \propto \exp[-\int_0^y \mu(y) dy]$. Thus, for the sharp domain wall of Fig. 3, for which the effective mass is a step-function, we find solutions at the domain wall which decay exponentially away from the domain wall. On the other hand, for a mechanical Landau-level mode obtained using material patterning, the mass varies linearly with y , i.e. $\mu \propto y$, and the mode indeed has a Gaussian profile (see Fig. 2.4). Furthermore, the solutions to the Jackiw-Rebbi model exhibit a parity anomaly, which can be used to ascertain that the domain-wall-bound modes as well as the Landau-level modes are both sublattice-polarized.

2.4.2 Topological robustness of the domain-wall mode

In this part, we explain in detail the robustness of the sublattice-polarized domain wall mode in the presence of disorder.

As explained in the previous section, a domain wall across which the mass $\mu(y)$ in Eq. (2.23) changes sign will always carry a domain-wall-bound mode. Intuitively, this mode corresponds to a Landau-level-like mode but in the presence of a spatially dependent magnetic field given by the derivative $\mu'(y)$. Thus, the existence of the domain-wall bound mode requires μ to change (and, in particular, change in sign) across the domain wall.

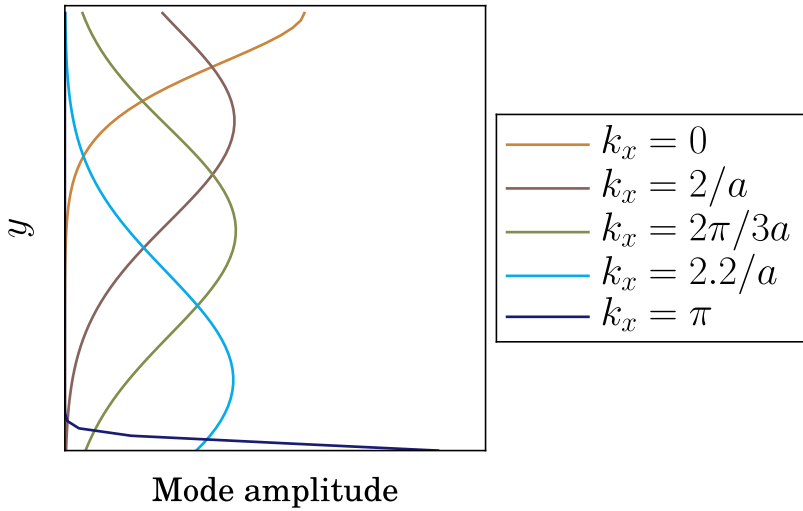


Figure 2.4: Visualizations of the zeroth Landau level for different wavenumbers. For $q_x = 2\pi/3a$, this mode has a Gaussian profile and is located precisely at the waveguide center due to a symmetry of the Dirac cone: the modes with frequency above (below) ω_K live on the lower (upper) half of the waveguide. We observe edge states with Gaussian profiles for wavenumber q_x near $2\pi/3a$. For example, when $q_x = 2/a$ (thus $q_x < 2\pi/3a$) the mode has a Gaussian profile and is located near the top edge of the waveguide (brown curve). In contrast, when $q_x = 2.2/a$ (thus $q_x > 2\pi/3a$) the mode has a similar shape, but is located near the bottom edge of the waveguide (light blue curve). Far from the Landau level, at $q_x = 0$ (π), the mode decays exponentially away from the top (bottom) edge. This figure is an expansion of Fig. 2.2e.

One of the consequences of nonzero μ is to break a chiral symmetry in this system. This chiral symmetry preserves the reflection symmetry of the Dirac cone: the cone looks the same right-side up as upside-down. Furthermore, this is the symmetry necessary to preserve the sublattice polarization (i.e. the fact that the mode lives on only one of the two sublattices) of the domain-wall bound mode. From the fact that μ has to vary across the domain wall and this violation of chiral symmetry, one might suppose that the domain-wall mode's existence also seems to presuppose that it will not be robust against disorder. However, quantitatively, the terms that break this chiral symmetry are small so that the domain-wall modes are nearly perfectly polarized on one sublattice (see Figs. 2.6 and 2.7).

Let us first explain the origins of topological robustness in this system and how it relies on chiral symmetry. If the dynamical matrix has form

$$D = \begin{pmatrix} 0 & H \\ H^\dagger & 0 \end{pmatrix}, \quad (2.24)$$

then we say that the system does have chiral symmetry. For this dynamical matrix, we can calculate the *winding number* of $\det H$, which is the integral of $\nabla_{\mathbf{k}} \ln \det H$, over a periodic contour γ in the Brillouin zone. The determinant $\det H$ is a complex number for each wavevector, and traces out a closed path in the complex plane as the wavevector follows the contour γ (see Fig. 2.5b). The integral counts how many times the path encloses the origin $\det H = 0$, and in particular, $\frac{1}{2\pi i} \int_{\gamma} d\mathbf{k} \cdot \nabla_{\mathbf{k}} \ln \det H$ is unity when the origin is enclosed once and zero otherwise. It thus forms a topological invariant for our system, which is called the *Herring number* in the context of Dirac cones [63, 190]. Only in the case when the vector potential is zero does this integral become not well-defined, because in that case the contour passes through the center of the Dirac cone, at which point $\det H = 0$.

Notably, in our system, D has the form of Eq. (2.24) only near the Dirac cone. Away from points K and K' , chiral symmetry does not hold and other diagonal terms enter the dynamical matrix. However, near the Dirac cone, where all of the phenomena considered in this work take place, these achiral terms are small and the chiral symmetry holds approximately. As a result, the topological robustness associated with this chiral symmetry can also be observed, as we explore in Fig. 2.7 for the sublattice polarization.

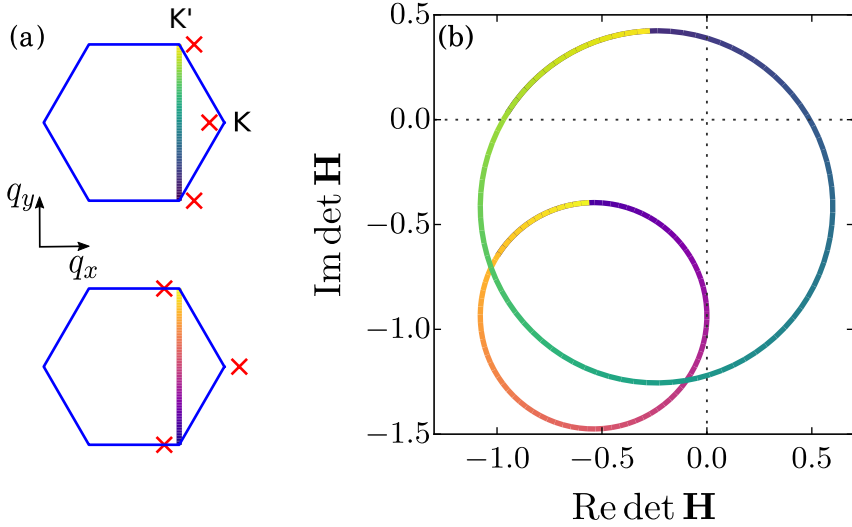


Figure 2.5: Topological invariants in a 2D Brillouin zone with a constant gauge field \mathbf{A} . (a) A schematic of the location of the Dirac points when the gauge field is constant. When $\mathbf{A} = (A_x, 0)$ and the x -component A_x is positive, the Dirac cone at \mathbf{q}_K shifts to the left and the cone at $\mathbf{q}_{K'}$ shifts to the right (top panel). For A_x negative, these cones shift in the opposite direction. When the Dirac cones shift, it is possible to define a winding contour around the Dirac cones that connects $\mathbf{q}_{K'}$ with itself via a vertical path across the Brillouin zone. (b) When the quantity $\nabla_{\mathbf{k}} \ln \det H$ [see Eq. (S7)] is integrated along the contour defined in (a), as long as the chiral symmetry of the honeycomb lattice is respected, the resulting quantity is an integer called the Herring number. This number is zero when $A_x > 0$ (small circle, which doesn't enclose the origin) and unity when $A_x < 0$ (large circle, which does enclose the origin). Thus, this number counts the Dirac cones within the contour and can only change when the sign of A_x changes as, e.g. in the case of the Landau level or the domain wall.

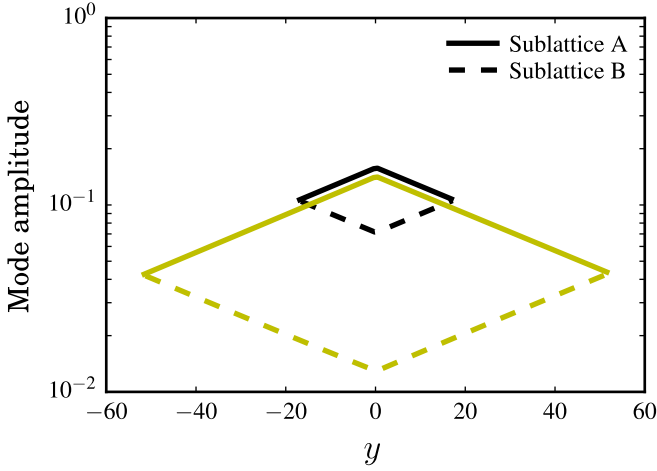


Figure 2.6: Amplitude of the midgap mode for quasi-one dimensional waveguides with different sizes $N = 20$ (black) and $N = 60$ (yellow) along the transverse direction plotted on a log-linear scale. For each system size, the amplitude of the vibrational mode on the two sublattices A and B are shown as solid and dashed lines respectively, as a function of y -position relative to the domain wall at $y = 0$. The component on sublattice A decays exponentially away from the domain wall, similar to the exponentially decaying domain-wall mode shown in Fig. 2.3b. The mode also has a component on sublattice B, which decays exponentially away from the waveguide edges. This component arises because an edge termination is similar to a domain wall with a different mass sign change compared to the actual domain wall in the system. The relative amplitudes of the two components are set by the boundary conditions at the edges: the loose node condition at the system edge requires that $\mathbf{u}_A = \mathbf{u}_B$, as the nodes at the boundary can not balance a nonzero force from the interior springs.

To check that the sublattice polarization remains significant in the presence of system disorder, we have performed numerical simulations of disordered waveguides. In Figure 2.7 we present the results of these simulations in which we note that although increasing disorder does somewhat affect the sublattice polarization, the effect is small in absolute terms. Even when the disorder strength is around 15% of the initial spring stiffness, the mode remains polarized within 5% of its initial, near-perfect, polarization.

2.5 Selective enhancement

The sublattice polarization of the Landau-level states can be used to selectively enhance these modes under external drive by employing site-dependent damping. For example, for positive magnetic fields, the Landau-level states live only on the A-sublattice of the honeycomb unit cell [99, 163]. If we introduce damping of the form $-\gamma\dot{\mathbf{u}}_B$ into the equation of motion, Eq. (2.3), such that only the displacements of the B-sublattice are damped, then the Landau-level acoustic waves would not be attenuated, whereas the rest of the sound waves, which generically are split between the A and B sublattices, would have a nonzero attenuation. To characterize this selective enhancement, we study the attenuation rate $\eta(\mathbf{q})$ as a function of mode wavevector, as well as the self-response function $\chi(\omega)$ which measures the displacements in response to a drive at frequency ω .

We use the drag matrix $\Gamma = \begin{pmatrix} \gamma_{\parallel} & 0 \\ 0 & \gamma'_{\parallel} \end{pmatrix}$ with $\gamma' = 0$ to model sublattice-biased dissipation. With the presence of these drag forces, the equation of motion becomes $m\ddot{\mathbf{u}} + \Gamma\dot{\mathbf{u}} + D\mathbf{u} = 0$. Now consider an external driving force $\mathbf{F}(\mathbf{R}, t) = \mathbf{F}(\mathbf{R})e^{i\omega t}$ which oscillates in time. With this force, the inhomogenous equation of motion is $m\ddot{\mathbf{u}} + \Gamma\dot{\mathbf{u}} + D\mathbf{u} = \mathbf{F}$. To find the solutions, we use Bloch functions, i.e. the normal modes of the periodic structure, to expand the drive as $\mathbf{F}(\mathbf{R}, t) = e^{i\omega t} \sum_{n\mathbf{k}} \mathbf{F}_{n\mathbf{k}} \mathbf{u}_{n\mathbf{k}} e^{i\mathbf{k}\cdot\mathbf{R}}$. A steady-state solution, if it exists, oscillates with the same frequency ω as the drive. The steady-state solution can be expanded as $\mathbf{u}(\mathbf{R}, t) = e^{i\omega t} \sum_{\mathbf{k}} c_{n\mathbf{k}} \mathbf{u}_{n\mathbf{k}} e^{i\mathbf{k}\cdot\mathbf{R}}$. From the equation of motion, we find that the coefficients $c_{n\mathbf{k}}$ obey

$$c_{n\mathbf{k}} = \frac{\mathbf{F}_{n\mathbf{k}}}{-m\omega^2 + i\Gamma_{n\mathbf{k}}\omega + \lambda_{n\mathbf{k}}}, \quad (2.25)$$

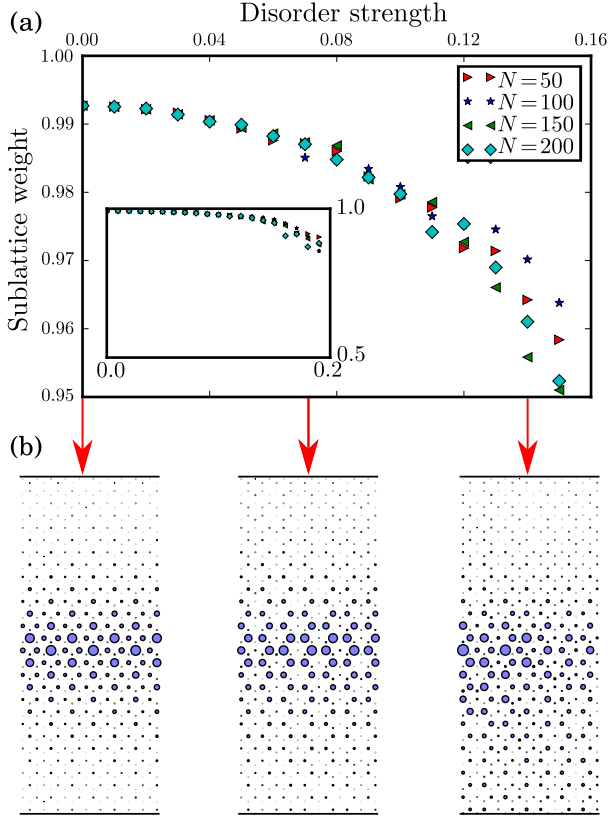


Figure 2.7: Effect of disorder in the spring constants on the sublattice polarization of modes bound to domain walls (see Fig. 2.3). (a) We consider waveguides that are infinite along the x -direction and have N unit cells along the y -direction. The disorder is implemented by rescaling each spring constant with spring constant $\kappa + \delta\kappa$ by a random number X via $(1 + X)\kappa + \delta\kappa$, where X is chosen from a uniform distribution on the interval $[-s, s]$ where we call the number s the disorder strength (x -axis of panel a). We then plot the relative weight of each mode on a sublattice averaged over 100 realizations of the disorder in panel (a). We note that it is always near unity (see inset). Even for disorder strength $\sim 10\%$, we note that the modes are still mostly polarized on one sublattice. Even for the most disordered cases we consider, the relative sublattice weight is 0.95, which indicates that the sublattice polarization of the domain-wall bound mode is robust against disorder in the spring constant. (b) Domain-wall bound mode amplitudes on each lattice site for several realizations of the disorder, with different disorder strengths. We note that even in the case in which the effects of the disorder on the mode are appreciable, the mode is still very strongly polarized on one of the sublattices.

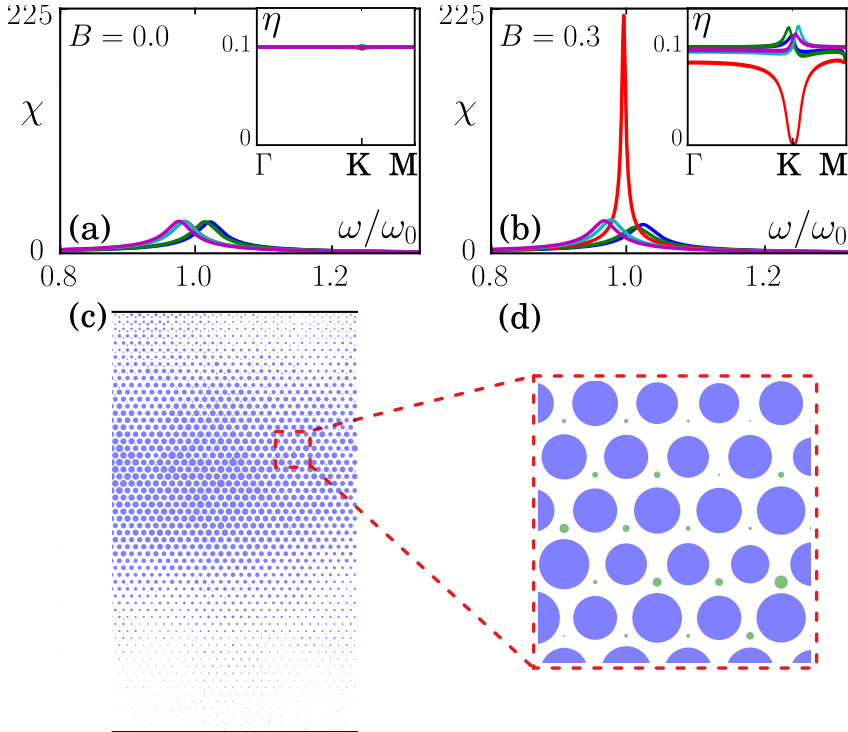


Figure 2.8: Single-mode response χ of Landau-level states in mechanical graphene, including the effect of damping on one sublattice and for pseudo-magnetic field values (a) $B = 0.0$ and (b) $B = 0.3$. Colors correspond to the different Landau-level bands identified in Fig. 2a. Insets: wavenumber-dependent attenuation rate η of the corresponding bands. (c) The steady-state response (for $B = 0.3$) to external periodic forcing with frequency close to the Dirac frequency and at an edge that is situated 50 unit cells to the left of the section shown. Each point is represented by a disc whose area is proportional to the amplitude of the response. (d) Zoom-in of (c) shows that the Landau-level mode is selectively enhanced due to the presence of sublattice-biased damping.

where $\Gamma_{n\mathbf{k}} = \sum_{n'} \mathbf{u}_{n'\mathbf{k}}^\dagger \Gamma \mathbf{u}_{n\mathbf{k}}$ and $\lambda_{n\mathbf{k}}$ are the eigenvalues of the dynamical matrix, Eq. 2.4. We expect the response to depend strongly on the damping. To see this, consider $\Gamma_{n\mathbf{k}}$ to be a real number. If $\Gamma_{n\mathbf{k}}^2 > 2\lambda_{n\mathbf{k}}m$ (corresponding to the overdamped limit), then the amplitude of the response never rises above $\mathbf{F}_{n\mathbf{k}}/\lambda_{n\mathbf{k}}$ – it attains this limiting value at low frequencies and falls off as $\mathbf{F}/m\omega^2$ at higher frequencies. If on the other hand, $\Gamma_{n\mathbf{k}}^2 < 2\lambda_{n\mathbf{k}}m$ (corresponding to the underdamped limit), the response develops a peak at $\omega_p^2 = \lambda_{n\mathbf{k}}/m - \Gamma_{n\mathbf{k}}^2/2m^2$, whose height diverges as $1/\Gamma_{n\mathbf{k}}$. Therefore, at low damping, the response will be dominated by modes whose natural frequency is close to the driving frequency. If for example, the lattice is driven by forcing atoms along one edge in an oscillatory manner, then $\mathbf{F}_{n\mathbf{k}}$ will be appreciable for several modes, but the only modes to have a strong response will be those whose natural frequency is close to the driving frequency.

This observation can be used to selectively enhance the zeroth Landau level mode, as seen in Fig. 2.8. In Fig. 4a-b, we plot $\chi(\omega) \equiv c_{n\mathbf{k}}/F_{n\mathbf{k}}$ for the Landau-level bands with $-2 \leq n \leq 2$, in response to an oscillatory drive that is proportional to the corresponding mode displacement vector, for $\mathbf{k} = \mathbf{q}_K$. In the absence of the pseudo-magnetic field B , the response is underdamped, but no mode stands out as having a largest peak in χ (Fig. 2.8a), whereas for nonzero B , χ exhibits a strong peak at a frequency ω_0 , corresponding to the zeroth Landau-level (Fig. 2.8b). In the insets, we plot the attenuation rates η , corresponding to the imaginary parts of the frequency spectrum, for these modes as a function of \mathbf{k} along the ΓKM cut of the Brillouin zone. We also observe from here that the zeroth Landau level mode is selected for nonzero B : it smaller attenuation than the other modes. We then drive the lattice with force $\mathbf{F}(t) = e^{i\omega t} \hat{x}$ (ω near ω_0), on two of the lattice points (near but slightly above the waveguide center), and observe the amplitude of the steady-state response sufficiently far away from this drive. We note that the pseudo-magnetic field combined with selective damping leads to selective enhancement of acoustic Landau-level modes relative to the rest of the attenuated acoustic spectrum.

2.6 Towards mechanical lasers

This phenomenon is the acoustic analog of selective enhancement of microwave modes realized in Ref. [72]. Just as selective enhancement for light waves may lead to the design of novel parity-time-symmetric [78, 81] and topological [89] lasers, analogously, the selective enhancement of sound waves may be useful in the design of sound amplification by stimulated emission

of radiation (SASERs), i.e. the acoustic analog of lasers, as well as acoustic couplers and rectifiers. The detailed design of such devices [87] would involve acoustic resonators, an acoustic drive, and nonlinearity of the response. A potential architecture for this device may involve resonators at every node in the metamaterial, with an external acoustic source populating the states within each resonator.

2.7 Conclusion

We explored acoustic phenomena associated with the Landau-level spectrum. For example, the acoustic analog of Shubnikov-de Haas oscillations [192] corresponds to a sharp peak in the phonon density of states at the Landau-level frequency. In addition, sound modes are confined within a length scale set by the analog of the magnetic length. Our theoretical findings pave the way towards realizations of these acoustic phenomena associated with the synthetic gauge fields [21]. In §2.4, we showed that even stronger confinement of sound modes can be engineered at a domain wall associated with a change in the effective mass of the phononic excitations, which localizes phonon modes that are analogous to the topological domain-wall states in the Su-Schrieffer-Heeger model of polyacetylene [172]. In §2.5, we showed how this domain-wall-bound mode exhibits robustness against a type of disorder that may come in the manufacturing of acoustic metamaterials – disorder in the stiffness of each component. Like other realizations of topological states [95, 109] in mechanical [44, 49, 53, 54, 55, 68, 70, 71, 73, 77, 82], acoustic [37, 57, 62, 64, 67, 74, 75, 76], and photonic [17, 83, 85, 86, 88], metamaterials, this characterization may help with the design of robust devices. We show that introducing dissipation on just one of the two sublattices enhances the domain-wall-bound sound mode. This feature may be implemented in the acoustic context by considering a material immersed in a viscous fluid (appropriate for low-Reynolds number, e.g. micro-scale metamaterials), or by including dampers (e.g. small dashpot dampers at every components for cm-scale realizations) within the material design. We suggest this feature may be exploited for the design of acoustic couplers, rectifiers, and sound amplification by stimulated emission of radiation (SASERs).

Chapter 3.

Photonic waveguides in liquid crystals



Liquid crystals are soft matter phases characterized by their orientational order [141]. As a result of this order, liquid crystals can control the propagation of light in a reconfigurable way, with applications ranging from liquid crystal displays (LCD) [125] to adaptive lenses [12]. Light waves that propagate through a birefringent material such as a liquid crystal acquire a Pancharatnam-Berry phase. We have seen in the first chapter of this thesis that a spatially varying Pancharatnam-Berry phase has an effect similar to a change of the refractive index in the form of a generalized Snell's law, Eq. 1.11 and interferes with the defraction of light beams [40]. Therefore, light incident to a birefringent medium can change direction, even when the refractive index of the medium is homogeneous [5, 7].

Light beams acquire a geometric Pancharatnam-Berry phase when passing through a thin film of birefringent molecules [118, 131]. Therefore, as we have seen in the first chapter, subwavelength liquid crystal metasurfaces can be designed to scatter a light beam towards a certain direction, making these materials suitable for flat optics elements [84, 93]. Furthermore, recently developed plasmonic photopatterning techniques [22, 51] can be used to achieve control over the patterns of the nematic textures in thin liquid crystal polymers, paving the way to achieve various optical performances using these materials [24, 28]. These techniques are used for designing and manufacturing of geometric phase lenses [120] and achieving a controlled continuous profile of the Pancharatnam-Berry phase [23]. In this chapter, we study the propagation of light in a liquid crystal medium with a particular focus on the waveguiding regimes in these materials.

Optical waveguides, i.e. electromagnetic waveguides at optical frequencies, have been realized in a number of ways, including using spatial gradients in the refractive index [128] and using photonic bandgaps [114, 136]. The examples include graded index fibers [168] and photonic crystal fibers [124, 139]. However, all these methods are based on changing the refractive index of the medium, e.g. through laser writing the dielectric material or by using optical cavities, such as in photonic crystal fibers. Slussarenko *et al.* [56] observed such waveguiding regimes by using consecutive geometric phase lenses of liquid crystals. In this chapter, we generalize this work by presenting a theoretical framework to study the guided modes in a liquid crystal. The analysis in this chapter will provide the basis for a discussion of topological photonics in liquid crystals which we will follow in the next chapter.

We study the paraxial light propagation (i.e. at small angles with the direction of propagation) in a birefringent medium that is described by a Schrödinger-type equation with the distance along the propagation direction as an effective time [104, 108]. A spatial modulation of the director field introduces a time-dependent vector and scalar potential into this effective theory. We will study a specific pattern that is periodic with the same length scale as the periodicity of the ordinary and extraordinary polarized light dynamics [141]. We focus on the regime where the orientational variations of the molecules happen in a scale that is smaller than the defocusing length of the light beam which leads to a separation of the scales in the dynamics of light wavepacket from smaller scale variations. This slow dynamics is then mapped to the dynamics of a quantum wavefunction under a time-periodic Hamiltonian which are studied using Floquet theory [61, 79]. We then use the techniques of the Floquet quantum mechanics to derive a numerical scheme to determine the guided modes of the medium in such regimes. We also show the resemblance of the birefringence effect with a variation of the refractive index by studying curved liquid crystal waveguides what reminds one to an optical fiber [128].

3.1 Paraxial light propagation in uniaxial media

Consider the propagation of a Gaussian light beam in a uniform uniaxial medium where the nematic molecules are oriented along the plane orthogonal to the direction of propagation. We start by Helmholtz equations for the transverse electromagnetic (TEM, $E_z = B_z = 0$) waves,

$$\frac{\partial^2}{\partial z^2} \psi_{xy} = -\nabla_{\perp}^2 \psi_{xy} - k_0^2 \epsilon \psi_{xy}, \quad (3.1)$$

where $\psi_{xy} = (E_x, E_y)$ is the transverse electric field, k_0 is the light wavenumber in the free space, and ϵ is the dielectric of the medium. In liquid crystals, because of the shape of the nematic molecules, beams with different polarizations experience different refractive indices. In such so-called uniaxial media, the dielectric tensor is given by

$$\epsilon(x, y, z) = \epsilon_{\perp} \mathbf{I} + (\epsilon_{\parallel} - \epsilon_{\perp}) \mathbf{n}^T \mathbf{n}, \quad (3.2)$$

where ϵ_{\perp} and ϵ_{\parallel} are the components of the dielectric tensor along the ordinary and extraordinary axes of the molecules, respectively and $\mathbf{n}(x, y, z)$ is the director field of the nematic orientations. The refractive indices for these two axes are combined in the following matrix:

$$\mathbf{N} = \sqrt{\epsilon_D} = \text{diag}(n_o, n_e), \quad (3.3)$$

where $\epsilon_D = \text{diag}(\epsilon_{\perp}, \epsilon_{\parallel})$ is the diagonalized dielectric tensor. Thus, the uniaxial medium is characterized by two particular indices n_o and n_e , that correspond to the so-called ordinary and extraordinary polarizations that propagate unchanged. Therefore, three characteristic length scales naturally appear: the light wavelength λ , the beating length $\Lambda = \lambda/(n_e - n_o)$ between the ordinary and extraordinary polarizations, and the Rayleigh length Z_R that determines the size of the Gaussian beam given in terms of the beam's wavelength and its width, w by

$$Z_R = \pi \bar{n} w^2 / \lambda, \quad (3.4)$$

where $\bar{n} = (n_e + n_o)/2$. Additional length scales characterize the spatial pattern of the liquid crystal. Here, we focus on patterns where only the orientation of the nematic liquid crystal molecules (i.e. the director field) is changed, while the ordinary and extraordinary indices n_o and n_e are the same in the whole system. For a liquid crystal composed of uniaxial elements

with orientations in the xy -plane, which is the case that is considered in this thesis, the director field is determined in terms of a single parameter, θ , as $\mathbf{n} = (-\sin \theta, \cos \theta, 0)$, where θ is the angle between the extraordinary and the y axes, see Fig. 3.1. The ordinary-extraordinary frame is rotated with respect to the Cartesian coordinates with the angle θ that corresponds to the orientation of the molecules. Therefore, one can rewrite Eq. 3.1 for the ordinary-extraordinary waves using the substitution $\psi_{\text{oe}} = \mathbf{R}^{-1}(\theta)\psi_{xy}$, where $\mathbf{R}(\theta)$ is the rotation operator with angle θ , and obtain

$$\begin{aligned} \partial_z^2 \psi_{\text{oe}} - 2i(\partial_z \theta) \sigma_y \partial_z \psi_{\text{oe}} &= -\nabla_{\perp}^2 \psi_{\text{oe}} \\ &+ 2i(\nabla_{\perp} \theta) \sigma_y \cdot \nabla_{\perp} \psi_{\text{oe}} + i(\nabla^2 \theta) \sigma_y \psi_{\text{oe}} \\ &+ (\nabla \theta)^2 \psi_{\text{oe}} - k_0^2 \epsilon_D \psi_{\text{oe}}. \end{aligned} \quad (3.5)$$

We now present the regimes in which the dynamic of a wavepacket can be separated from the variations in small scales using slowly varying envelope approximation (SVEA). These regimes are determined by the relative ratios of the length scales that are discussed above. More precisely, we assume that between these scales, λ is usually the smallest (or fastest), but for the other two length scales various situations could take place, depending on the ratio

$$\frac{\Lambda}{Z_R} = \frac{(\lambda/Z_R)^2}{\pi \bar{n} \Delta n}. \quad (3.6)$$

In the following, we study the large birefringence regime, where the light focusing can be affected from the dynamics inside each beating length. The small birefringence regimes are discussed in the appendix 3.5.1.

3.1.1 Large birefringent medium: interaction picture

When the birefringence of the medium, $\Delta n = n_e - n_o$ is sufficiently large, we are in a regime where Λ is a fast variable compared to the Rayleigh length, Z_R as given by Eq. 3.4. Thus, there are two small quantities

$$\varepsilon_1 = \lambda/Z_R \quad \text{and} \quad \varepsilon_2 = \Lambda/Z_R \quad (3.7)$$

concerning the paraxial light propagation in this regime. In such case, the effect of changes happening over length Z_R can be considered as perturbations on top of the faster dynamics which takes place over the birefringence wavelength Λ . This z -dependent interaction can be treated by separating the dynamics over the fast and slow length scales, similar to exploiting the interaction picture in

quantum mechanics [45]. This is done by writing down the wavefunction as $\psi_{\text{oe}}(x, y, z, \varepsilon_1 z, \varepsilon_2 z) = \mathbf{U}_{\text{oe}}(z, \varepsilon_2 z)\psi(x, y, z, \varepsilon_1 z)$, where

$$\mathbf{U}_{\text{oe}}(z) = e^{ik_0 \mathbf{N} z} \quad (3.8)$$

is the evolution of the polarization in a homogeneous uniaxial medium. The dynamical equation for the wavepacket in the interaction picture can be cast as

$$\begin{aligned} \partial_z^2 \psi + [2ik_0 \mathbf{N} - 2i(\partial_z \theta) \mathbf{S}(z)] \partial_z \psi &= -\nabla_{\perp}^2 \psi \\ &- 2k_0(\partial_z \theta) \mathbf{S}(z) \mathbf{N} \psi + 2i(\nabla_{\perp} \theta) \mathbf{S}(z) \cdot \nabla_{\perp} \psi \\ &+ i(\nabla^2 \theta) \mathbf{S}(z) \psi + (\nabla \theta)^2 \psi, \end{aligned} \quad (3.9)$$

where

$$\mathbf{S}(z) = \mathbf{U}_{\text{oe}}^{-1}(z) \sigma_y \mathbf{U}_{\text{oe}}(z) = e^{i\frac{2\pi z}{\Lambda} \sigma_z} \sigma_y \quad (3.10a)$$

$$= \sigma_y \cos(k_0 \Delta n z) + \sigma_x \sin(k_0 \Delta n z) \quad (3.10b)$$

is the spin-dependent part of the the dynamics in terms of the Pauli matrices. To see how the terms involved in this equation are compared to each other, we write them in terms of dimensionless variables $X = x/w$, $Y = y/w$, and $Z = z/Z_R$ and then multiply the entire equation by $\frac{Z_R}{2\bar{n}k_0} = \frac{w^2}{4}$ to get

$$\begin{aligned} \frac{\varepsilon_1}{4\pi\bar{n}} \partial_Z^2 \psi + \left[i\frac{\mathbf{N}}{\bar{n}} - \frac{i}{2\pi\bar{n}} \varepsilon_{\theta} (\partial_{Z_{\theta}} \theta) \mathbf{S}(z/\Lambda) \right] \partial_Z \psi \\ = -\frac{1}{4} \nabla_{\perp}^2 \psi - (Z_R/Z_{\theta}) (\partial_{Z_{\theta}} \theta) \mathbf{S}(z/\Lambda) \frac{\mathbf{N}}{\bar{n}} \psi \\ + \frac{i}{2} (\nabla_{\perp} \theta) \mathbf{S}(z/\Lambda) \cdot \nabla_{\perp} \psi \\ + \frac{i}{4} \left[\nabla_{\perp}^2 \theta + (w/Z_{\theta})^2 \partial_{Z_{\theta}}^2 \theta \right] \mathbf{S}(z/\Lambda) \psi \\ + \frac{i}{4} \left[(\nabla_{\perp} \theta)^2 + (w/Z_{\theta})^2 (\partial_{Z_{\theta}} \theta)^2 \right] \mathbf{S}(z/\Lambda) \psi, \end{aligned} \quad (3.11)$$

where ∇_{\perp} is the gradient with respect to dimensionless variables and Z_{θ} is a characteristic length scale over which the orientation of the molecules vary along the z axis, and $\varepsilon_{\theta} = \lambda/Z_{\theta}$. Assuming $\lambda \ll Z_R$ which implies $w \ll Z_R$ leads to the following dynamical equation after reviving the original variables:

$$\begin{aligned} i\partial_z\psi = & -\frac{1}{2\bar{n}k_0}\nabla_{\perp}^2\psi - (\partial_z\theta)\mathbf{S}(z)\psi \\ & + \frac{i}{\bar{n}k_0}(\nabla_{\perp}\theta)\mathbf{S}(z) \cdot \nabla_{\perp}\psi + \frac{i}{2\bar{n}k_0}(\nabla^2\theta)\mathbf{S}(z)\psi \\ & + \frac{1}{2\bar{n}k_0}(\nabla\theta)^2\psi, \end{aligned} \quad (3.12)$$

which can be rearranged into the following form:

$$\begin{aligned} i\partial_z\psi = & -\frac{1}{2\bar{n}k_0}[\nabla_{\perp} - i(\nabla_{\perp}\theta)\mathbf{S}(z)]^2\psi - (\partial_z\theta)\mathbf{S}(z)\psi \\ & + \frac{1}{2\bar{n}k_0}[i(\partial_z^2\theta)\mathbf{S}(z) + (\partial_z\theta)^2]\psi. \end{aligned} \quad (3.13)$$

The last two terms are of order $\frac{1}{Z_R}\left(\frac{w}{Z_{\theta}}\right)^2$, and therefore can be neglected in the limit where $w \ll Z_{\theta}$. This leads to the wavepacket evolution

$$i\frac{\partial\psi}{\partial z} = -\frac{1}{2\bar{n}k_0}[\nabla_{\perp} + i\mathbf{A}]^2\psi + \mathbf{V}\psi, \quad (3.14)$$

with $\mathbf{A}(z) = -(\nabla_{\perp}\theta)\mathbf{S}(z)$ and $\mathbf{V}(z) = -(\partial_z\theta)\mathbf{S}(z)$, where $\mathbf{S}(z)$ is a z -dependent matrix that only depends on Λ and is responsible for the polarization dynamics. Formally, this equation resembles the Schrödinger equation of quantum mechanics, provided that the paraxial direction z is replaced by time. From now on, in this chapter and the next one we refer to z as time.

3.2 Guiding regimes for light in a uniaxial medium

We now use the results in the previous section to study the photonic guiding regimes in liquid crystals as a result of the interplay between light and the director of the nematic molecules.

In the quantum mechanical language, a guided mode to the paraxial equation of motion, Eq. 3.14 is an eigenmode of the Hamiltonian, if it does not depend on time. However, note that since in this effective Schrodinger equation the Hamiltonian is time-dependent, and therefore, it is not generally

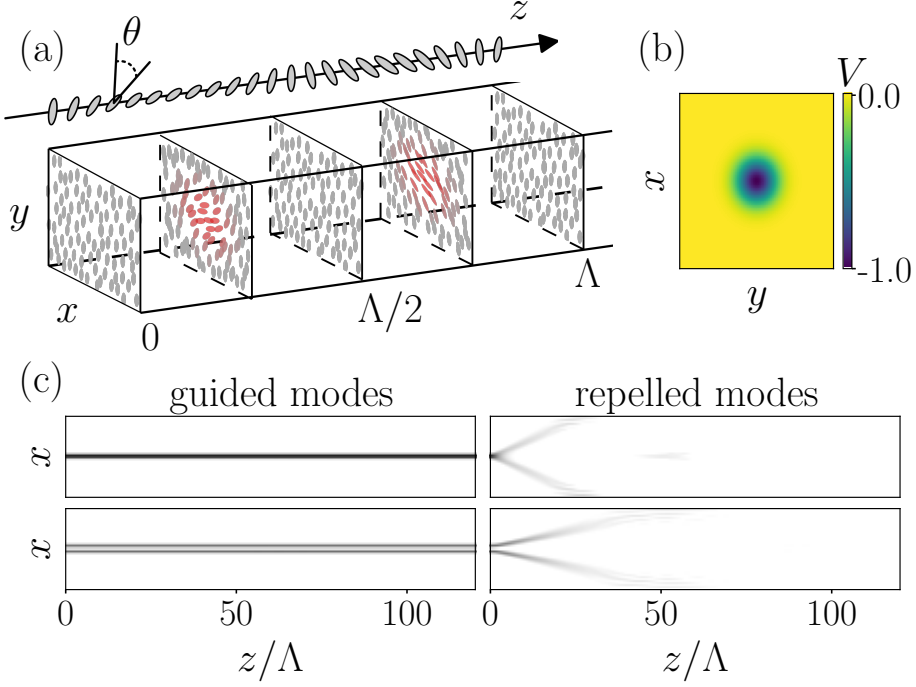


Figure 3.1: (a) The liquid crystal configuration corresponding to one waveguide, Eq. 3.16 with $\Gamma_0 = \pi/12$ and $w_p = 1$ and (b) the effective potential associated with it. Left panels in (c) show the evolution of the guided modes while right panels correspond to the repelled modes of this system. Top and bottom panels in (c) correspond to the zeroth and first order modes of the system.

possible to find an eigenmode of the evolution for the entire period of time. This time dependence comes from two sources of drive: the phase evolution U_{oe} and the periodicity of the configuration along the z -direction. When the orientation $\theta(x, y, z)$ of the director field is periodic in the paraxial direction z with a the same period Λ of the phase evolution, the Hamiltonian is Λ -periodic in z , and can be analyzed using Floquet theory [61, 79]. The main idea is that the propagation of light over large distances $z \gg \Lambda$ is essentially captured by repeating its evolution over one period Λ , which is described by the evolution operator $U(\Lambda)$ associated with equation (3.14). The eigenvalues of the operator $U(\Lambda)$ are phases of the form $e^{-i\kappa\Lambda}$ where κ is the quasi-momentum in the paraxial direction of the corresponding eigenmode. Here, the eigenmodes describe guided modes of the soft waveguide, and up to variations at the (small) scale Λ their intensity remains constant.

The use of Floquet eigenmodes generalizes the previously used methods in finding the eigenmodes of the time-averaged Hamiltonian [56]. A perturbative approach can be used to find the dynamics inside a Floquet period using quasi-modes as an approximation for the Floquet-Bloch modes [40, 182]. Here, we use a more general approach that is based on finding the eigenmodes of the system's evolution in the stroboscopic picture. Using this new method, one can also find the higher-order guided modes of such systems, i.e. modes that repeat themselves (up to a global phase), but with a different quasi-momentum and intensity pattern. Also, the eigenmodes of the Floquet evolution operator will remain guided over larger distances in z , given the other sources of losses are not there ♠.

We construct this evolution operator numerically by slicing period Λ into small steps δz and by using the following feature of the evolution operator:

$$U(z_3, z_2)U(z_2, z_1) = U(z_3, z_1). \quad (3.15)$$

Since $U(\Lambda)$ is a unitary operator, its eigenvalues reside on the unit circle. Hence, unlike a usual quantum problem, a highly oscillating mode in this spectrum can lie very close to another mode that is well localized in its spatial pattern. This makes the numerical diagonalization of this operator unstable and subject to accidental degeneracies. We solve this issue by exploiting the Sambe space representation of the Floquet Hamiltonian and their modes, which we explain in the appendix 3.5.3.

We applied this method to a few systems. Here, we show the calculations that reproduce the results by Ref. [56]. We consider a Gaussian nematic director patterning that is described by the following orientational field:

$$\theta(x, y, z) = \Gamma_0 e^{-(x^2+y^2)/w_p^2} \sin(2\pi z/\Lambda), \quad (3.16)$$

where $\Gamma_0 = \pi/12$ is the amplitude of the director field's rotation, w_p is the width of the Gaussian pattern, and Λ the periodicity of the pattern along the effective time and is equal to the beating length between the ordinary and extraordinary light beams. The refractive indices for this birefringent medium are $n_o = 1.5$ and $n_e = 1.7$ and thus we have $\Lambda = \lambda/\Delta n = 5\lambda$. We also consider $w_p = \lambda$. The liquid crystal pattern associated with this pattern is shown in Fig. 3.1(a).

♠ In this study we do not consider the internal sources of loss that can give rise due to the interaction of the electromagnetic waves with a liquid crystal. We will discuss this in more detail in a discussion about non-Hermiticity of this system in the next chapter.

We use our numerical methods to generalize the results of the Ref. [56] by finding the various guided modes with different spatial intensity pattern. We order these modes by the first moment of their spatial distribution around the waveguide center, $\frac{1}{\mathcal{N}} \int r I(r) dr$, where $I(r) = \psi^\dagger(r)\psi(r)$ is the light intensity and is non-negative everywhere, and $\mathcal{N} = \int I(r) dr$ is the normalization factor. The evolution of the first two guided modes obtained with this method is shown in the left panels of the Fig. 3.1(c). With each guided mode is associated a repelled mode obtained by its complex conjugation. To understand why this is the case, we note that in our numerical method we build a $2N \times 2N$ matrix for $U(\Lambda)$, where N is the size of the mesh in the simulation box in each of the x - and y directions, and the doubling factor comes from the polarization degree of freedom. However, the guided modes of a waveguide can not span the entire vector space of the initial modes, as not all the modes are guided by this waveguide. We note that the eigenvectors of the evolution operator come in pairs of modes with similar intensity patterns, of which one is a physical mode that corresponds to a guided mode of the evolution. The other mode in each pair is unphysical, i.e. their polarization components oscillate with the grid. Thus, the doubling of the degrees of freedom in this numerical scheme leads to spurious modes to construct half of the spectrum. Instead of these unphysical modes, the system supports the presence of repelled modes, which in the Ref. [56] are the modes with opposite circular polarizations of the guided modes. In our numerical scheme here, the complex conjugation does this transformation in the polarization. The complex conjugated modes correspond to the eigenmodes of a new Hamiltonian which has a scalar potential with opposite sign. This change in the sign leads to the transformation from a potential well to a potential barrier for the guided modes of the initial system in the effective picture. In Fig. 3.1 (c) we show two guided modes and the repelled modes associated to them.

3.3 Curved waveguides

We saw in the first chapter that the Snell's law, Eq. 1.11, in the presence of the birefringent medium acquires a modifying term that is proportional to the gradient of the Pancharatnam-Berry phase of the light beam. Therefore, the liquid crystal optical waveguides that we described in the previous section might also be seen as a consequence of the similar effect of the spatial variation in the Pancharatnam-Berry phase with the refractive index grading of the medium. Here, we present a test of this comparison by studying the liquid

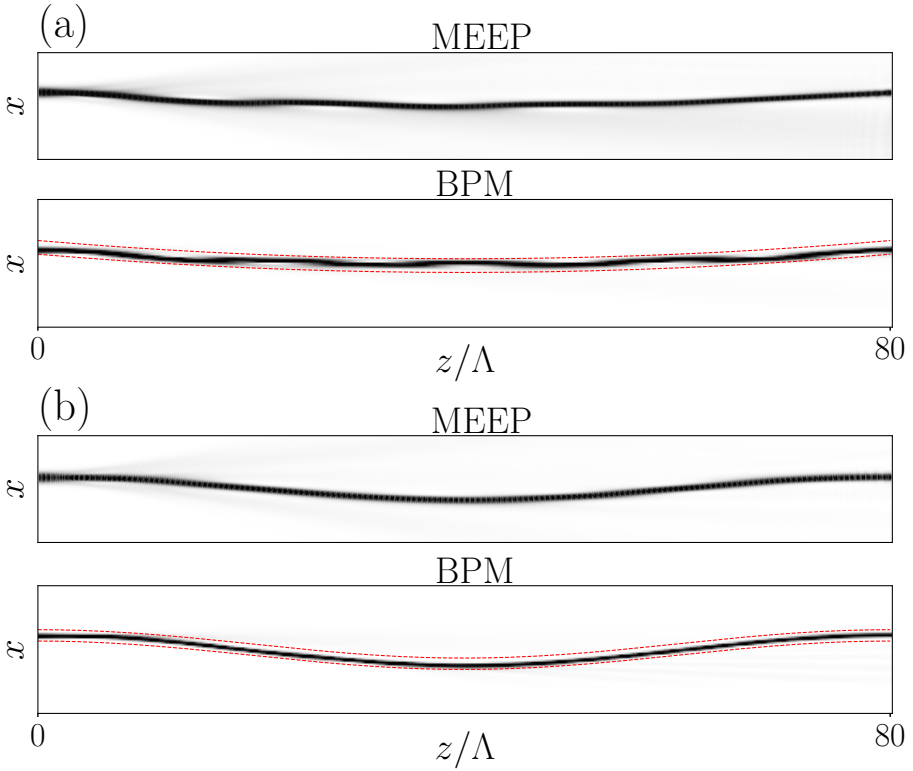


Figure 3.2: Curved (a) parabolic and (b) sinusoidal waveguides. The results from solving Maxwell’s equations using the software MEEP and solving the effective Schrödinger equations using BPM methods show agreement. Dashed lines correspond to the waveguide borders, i.e. the width of the transverse Gaussian patterns that create them.

crystal waveguides with curvature. These curved waveguides can be useful when for example a time-varying coupling strength of the waveguides is needed. This will allow us to investigate the phenomena associated with tight-binding quantum systems with time-varying hopping amplitudes, once we develop this framework in the next chapter.

More importantly, the curvature can lead to a new coupling between the polarization of light and its path via a spin-orbit coupling [60, 110, 111]. Light beam inside these waveguides acquire both Pancharatnam-Berry phase and Rytov-Vladimirskii-Berry phase simultaneously, see § 1.2. The interplay of these two different geometric phases and the phenomena associated to this interplay are subjects to future investigations.

For the numerical study of these systems we use both MEEP software [102] as well as a beam propagation method (BPM) in Python. MEEP solves the full Maxwell's equations using finite-difference time-domain (FDTD) method which makes it numerically expensive for large-scale systems. The BPM method uses the slowly varying envelope approximation and the resulting first order differential equation along the z -axis to solve this system as an initial value problem. Using the paraxial equation of motion, Eq. 3.14, we develop a code based on the Crank-Nicolson method to solve this equation with a given initial condition. The latter is a considerably computationally faster code for larger-scale systems, such as those we consider for a lattice of waveguides in the next chapter. The Schrödinger solver code can also be adapted to solve the Floquet propagators and their diagonalization to find the guided modes, as we discuss in appendix 3.5.3.

We observe that similar to before, for a small curvatures in the waveguide shapes, the lights are guided for a specific circular polarized light, whereas the light beam with opposite polarization is completely repelled. The numerical results for the propagation of a guided mode (that is obtained in the previous section for a straight waveguide) inside a curved waveguide is shown in Fig. 3.2. These results also show a good agreement of our python code with the MEEP simulations.

We further notice an effect similar to reflection of light from waveguide walls in optical fibers [132], for example in Fig. 3.2. This is remarkable, since there is not a solid wall like in a index-graded optical fiber and shows a strong evidence to the generalized Snell's law, 1.11. This bouncing effect makes it important to have a bound on how much these waveguides can be curved so that the incident light is not transmitted outside. We further confirm this in Fig. 3.3 for a waveguide that has the sinusoidal shape with a curvature that is two times larger from the waveguide in Fig. 3.2(b).

3.4 Fully rotating nematic waveguides

So far we considered modulations of the nematic fields that are non-monotonic along the z direction, for example by the orientation that is spatially varied as

$$\theta(x, y, z) = \theta_0(x, y) \sin 2\pi z / \Lambda. \quad (3.17)$$

This consideration was done to achieve a smooth director field that is periodic along the z -axis. However, since θ is an orientation, it can also be periodic when it fully rotates on a cycle. Here, we consider a pattern that is periodic while we require the center of the waveguides to fully rotate. A full rotation

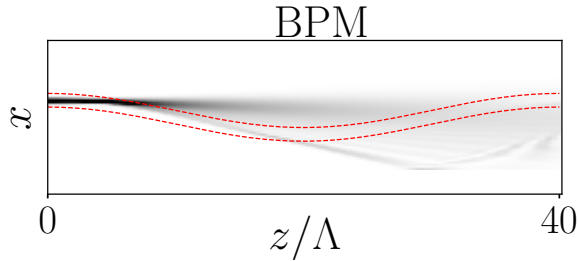


Figure 3.3: The effect of curvature in the ability of the waveguides we study for light confinement. We observe the coinciding light is transmitted outside when the waveguide curvature is twice as the one depicted in Fig. 3.2(b).

of the nematic pattern introduces a handedness which can be mapped to an effective time-reversal symmetry breaking in the paraxial limit, similar to the effect of a helical path [88]. However, as we discussed in our description of geometric phases of light, the nature of the rotation in the two problems above are different: in a fully rotating nematic waveguide this is a Pancharatnam-Berry phase, whereas in a helical waveguide it is a Rytov-Vladimirskii-Berry phase, resulting from a change in the orientation along the orbital path of the light beam.

Since the orientation of the molecules have a spatial dependent amplitude, e.g. in our first example in 3.16 that is given by

$$\theta_0(x, y) = \Gamma_0 \exp [-(x^2 + y^2)/w_p^2], \quad (3.18)$$

it is not possible to apply the full rotation in the entire xy -plane. In the example above, this can be seen by noticing the asymptotic behavior of the director field's orientation that vanishes at large distances from waveguide's center. Therefore, one needs to consider a fully rotating director field only in a finite region in the xy -plane. This full rotation at the center can be achieved by simply requiring that the director field continues in the same rotating manner after reaching its maximum (this can be achieved with $\Gamma_0 = \pi/2$ as well), as shown in Fig. 3.4(a). When $\Gamma_0 = \pi$, the center of the pattern reaches to its initial direction at $z = \Lambda/4$, but the nearby molecules are at their maximum rotation with an angle smaller than smaller than π . For the latter, the periodicity would still be achieved by the non-monotonic pattern suggested by Eq. 3.17.

As a result we can expect defects arising in the nematic texture due to this difference between the topology in the center and points far away. Consequently, a large gradient of the orientation is expected in the perpendicular plane. These defects can introduce large peaks in the gauge field around the discontinuity of the orientational order. To avoid large perturbations due to the discontinuity of the orientation along the xy -plane, we put these defects on a relatively far distance from the center of the waveguide. We consider the following pattern in a circle $C_R(0)$ around the center:

$$\theta_2 = \begin{cases} \theta_0(x, y) \sin\left(\frac{2\pi z}{\Lambda}\right) & \text{if } (x, y) \notin C_R(0) \text{ or } \frac{z}{\Lambda} \in [0, \frac{1}{4}] \\ 2\pi - \theta_0(x, y) \sin\left(\frac{2\pi z}{\Lambda}\right) & \text{if } (x, y) \in C_R(0) \text{ and } \frac{z}{\Lambda} \in [\frac{1}{4}, \frac{3}{4}] \\ 4\pi + \theta_0(x, y) \sin\left(\frac{2\pi z}{\Lambda}\right) & \text{if } (x, y) \in C_R(0) \text{ and } \frac{z}{\Lambda} \in [\frac{3}{4}, \frac{1}{4}] \\ \dots & \dots \end{cases} \quad (3.19)$$

This pattern is illustrated in Fig. 3.4(a). Note that R can essentially be large enough to make the discontinuity in the nematic orientation in the xy -plane negligible. However, now there are large gradients of the director field when passing through $z = \Lambda/4$ and $3\Lambda/4$ planes, see Fig. 3.4(b). To make this perturbation smaller, the Gaussian pattern $\theta(x, y)$ can be kept less sharp, i.e. wider. The width associated to the variations in the perpendicular plane can affect the validity of the paraxial approximation through changing the Rayleigh defocusing length.

With these considerations we now look at the guided modes of a fully rotating LC system in z . We use large R values for now, hence the entire nematic texture follows the modified variation Eq. 3.19. We observe that at $w_p \lesssim 5$ the guided modes deviate largely from a Gaussian, but for more stretched patterns with larger width, we observe the guided modes that are close to a Gaussian pattern.

In conclusion, we have shown in this chapter that paraxial light propagation in a liquid crystal medium can be mapped to Floquet quantum mechanical systems. We then developed a numerical scheme to extract the guided modes in liquid crystals with beating length between ordinary and extraordinary lights much smaller than the defocusing length of the light beam. We used this numerical method to find guided photonic modes of a liquid crystal medium with certain nematic patterns. Our results include higher-order guided modes, guided modes in curved waveguides, and guided modes in fully rotating nematic patterns. Looking forward, we would like to investigate the interplay

between various geometric phases that a monochromatic light beam acquires in such waveguides. We will also discuss in the next chapter symmetries of these waveguides, which we will use towards implementation of topological photonics in designer liquid crystal media.

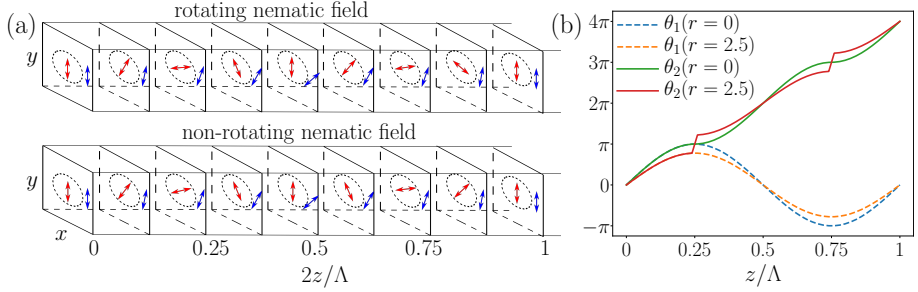


Figure 3.4: (a) Half a Floquet period of the liquid crystal configuration corresponding to rotating (top) and non-rotating (bottom) director fields. For clarity at each time step, one nematic for both inside and outside of the region C_R , depicted by the dashed circle, are shown. (b) The orientation field for rotating (solid lines) and non-rotating (dashed lines) at the center ($r = 0$) and one off-center, $r = 2.5$, point inside C_R . The full rotating director field at the center imposes discontinuity in the director field at off-center points inside C_R . We set $w_p = 5$ and $R = 15$ for this plot; larger pattern widths would lead to smaller discontinuity at $z/\Lambda = 0.25, 0.75$, but larger discontinuity in nematic orientation at the xy -plane when crossing from C_R .

3.5 Appendix

3.5.1 Dynamics of circularly polarized waves through a uniform uniaxial medium

In a uniform medium, where $\theta(x, y, z) = \theta_0$, the dielectric tensor is diagonalized as

$$\epsilon_D = \mathbf{R}(\theta_0) \begin{pmatrix} \epsilon_{\perp} & 0 \\ 0 & \epsilon_{\parallel} \end{pmatrix} \mathbf{R}^{-1}(\theta_0), \quad (3.20)$$

where

$$\mathbf{R}(\theta) = \begin{pmatrix} \cos \theta & -\sin \theta \\ \sin \theta & \cos \theta \end{pmatrix}. \quad (3.21)$$

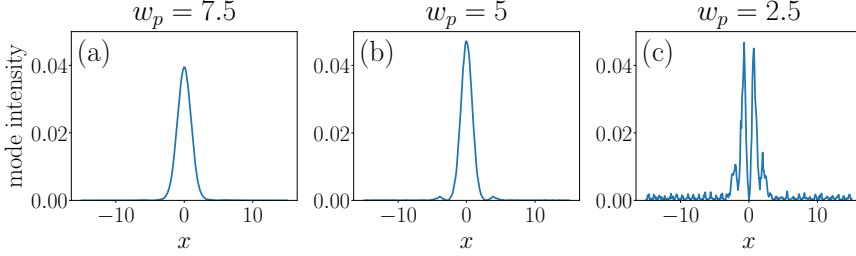


Figure 3.5: Floquet eigenmode of a fully rotating nematic waveguide for three values of the transverse pattern Gaussian widths. The narrower patterns correspond to larger discontinuities along the z direction, as depicted in Fig. 3.4(b). This discontinuity leads then to a deviation of the eigenmodes from Gaussian shapes. For these simulations we use $R = 15$.

Thus, the change of basis $\psi_{oe} = \mathbf{R}^{-1}(\theta_0)\psi_{xy}$ from Cartesian to ordinary/extraordinary (oe) basis diagonalizes the equation of motion 3.1. In the oe basis, the solution to the equation of motion is given by

$$\psi_{oe}(z) = \mathbf{U}_{oe}(z)\psi_{oe}(0) \quad (3.22)$$

where

$$\mathbf{U}_{oe} = \begin{pmatrix} e^{ik_0 n_o z} & 0 \\ 0 & e^{ik_0 n_e z} \end{pmatrix}, \quad (3.23)$$

where $n_o = \sqrt{\epsilon_{\perp}}$ and $n_e = \sqrt{\epsilon_{\parallel}}$ are refractive indices for ordinary and extraordinary lights, respectively.

Let us now consider propagation of a circularly polarized light in such a medium. We thus change our basis to left/right circularly polarized basis. The dynamics is then given by

$$\psi_L(z) = e^{i\bar{n}k_0 z} \left[\cos(\delta/2)\psi_L(0) - i \sin(\delta/2)e^{2i\theta_0}\psi_R(0) \right], \quad (3.24)$$

$$\psi_R(z) = e^{i\bar{n}k_0 z} \left[\cos(\delta/2)\psi_R(0) - i \sin(\delta/2)e^{-2i\theta_0}\psi_L(0) \right], \quad (3.25)$$

where $\bar{n} = (n_o + n_e)/2$ is the average refractive index and $\delta = k_0(n_e - n_o)z$ is the phase retardation via propagation. The length-scale corresponding to the polarization dynamics is then given by

$$\Lambda = 2\pi/(k_0\Delta n) = \lambda/\Delta n, \quad (3.26)$$

where $\Delta n = n_e - n_o$.

3.5.2 Dynamics of paraxial light propagation in liquid crystals with medium to low birefringence

In the chapter, we derived the dynamics of light wavepackets for a regime where $\Lambda \ll Z_R$. We now focus on the intermediate values of the birefringence where the two length scales Λ and Z_R become of the same order, the light propagation dynamics enters a different regime where both of these length scales are slow compared to λ . Thus, the small quantities of the problem are

$$\varepsilon_1 = \lambda/Z_R, \quad (3.27)$$

$$\varepsilon_2 = \lambda/\Lambda. \quad (3.28)$$

In this regime, we can not apply the interaction picture that is introduced above. Instead, the SVEA can directly be applied on the equation of motion Eq. (3.5). To do that, we start by expanding the wavefunction in the L/RCP basis as

$$\psi_{\text{oe}}(z) = F_R(z)\psi_R + F_L(z)\psi_L, \quad (3.29)$$

where $\psi_R = \frac{1}{\sqrt{2}}(1; i)$ and $\psi_L = \frac{1}{\sqrt{2}}(1; -i)$ are the eigenvectors of the Pauli matrix σ_y . Plugging this expansion into Eq. (3.5), we find the following set of coupled differential equations:

$$\begin{aligned} \partial_z^2 F_R(z) - 2i(\partial_z \theta)\partial_z F_R(z) &= -\nabla_{\perp}^2 F_R(z) + 2i(\nabla_{\perp} \theta) \cdot \nabla_{\perp} F_R(z) \\ &+ i(\nabla^2 \theta)F_R(z) + (\nabla \theta)^2 F_R(z) \\ &- k_0^2 \frac{n_o^2 + n_e^2}{2} F_R(z) - k_0^2 \frac{n_o^2 - n_e^2}{2} F_L(z), \end{aligned} \quad (3.30)$$

$$\begin{aligned} \partial_z^2 F_L(z) + 2i(\partial_z \theta)\partial_z F_L(z) &= -\nabla_{\perp}^2 F_L(z) - 2i(\nabla_{\perp} \theta) \cdot \nabla_{\perp} F_L(z) \\ &- i(\nabla^2 \theta)F_L(z) + (\nabla \theta)^2 F_L(z) \\ &- k_0^2 \frac{n_o^2 + n_e^2}{2} F_L(z) - k_0^2 \frac{n_o^2 - n_e^2}{2} F_R(z). \end{aligned} \quad (3.31)$$

To perform SVEA, we extract and separate the fast dynamics from $F_R(z)$ and $F_L(z)$, i.e. the dynamics over the small length scale λ . The electromagnetic wavefunction $\psi_{\text{oe}}(z)$ can also be expressed as

$$\psi_{\text{oe}}(z) = F_R\psi_R(z) + F_L\psi_L(z), \quad (3.32)$$

where $\psi_{R,L}(z) = \frac{\psi_o(z) \pm \psi_e(z)}{\sqrt{2}}$. The dynamics of this wavefunction in the limit when $\lambda \ll \Lambda$ is given by (see Eq. (3.22) in the appendix)

$$\psi_o(z) = e^{ik_0 n_o z} \psi_o + \mathcal{O}(\lambda/\Lambda), \quad (3.33)$$

$$\psi_e(z) = e^{ik_0 n_e z} \psi_e + \mathcal{O}(\lambda/\Lambda). \quad (3.34)$$

Inserting this into Eq. (3.32) and comparing with Eq. (3.29) we find that

$$\begin{pmatrix} F_R(z) \\ F_L(z) \end{pmatrix} = \left[e^{ik_0 \bar{n} z} \begin{pmatrix} \cos \frac{\pi z}{\Lambda} & -i \sin \frac{\pi z}{\Lambda} \\ -i \sin \frac{\pi z}{\Lambda} & \cos \frac{\pi z}{\Lambda} \end{pmatrix} (1 + \mathcal{O}(Z)) \right] \begin{pmatrix} F_R \\ F_L \end{pmatrix}, \quad (3.35)$$

where $Z = \varepsilon_2 z$ is the slow variable along the propagation direction in this regime. Thus, the amplitudes' dynamics include two different length scales λ and Λ . If we assume Λ to be comparable with the Rayleigh length, we can consider that the fast dynamics is only given by the exponential in the first term, which leads to the following separation:

$$\begin{pmatrix} F_R(z) \\ F_L(z) \end{pmatrix} = e^{ik_0 \bar{n} z} \begin{pmatrix} F_R(Z) \\ F_L(Z) \end{pmatrix}. \quad (3.36)$$

By Inserting this into Eqs. (3.30) and (3.31) we get to the following coupled equations of motion:

$$\begin{aligned} & -k_0^2 \bar{n}^2 F_{R,L}(Z) + 2ik_0 \bar{n} \partial_Z F_{R,L}(Z) + \partial_Z^2 F_{R,L}(Z) \\ & \mp 2i \partial_Z \theta [\partial_Z F_{R,L}(Z) + ik_0 \bar{n} F_{R,L}(Z)] = -(\nabla_{\perp} \mp i \nabla_{\perp} \theta)^2 F_{R,L}(Z) \\ & -k_0^2 \left[\bar{n}^2 + (\Delta n/2)^2 \right] F_{R,L}(Z) - k_0^2 \bar{n} \Delta n F_{L,R}(Z) \end{aligned} \quad (3.37)$$

Now, after introducing the fast and slow variables the SVEA can be performed by considering $\lambda \ll \Lambda, Z_R$. It follows that

$$i \partial_Z F_R(Z) = -\frac{1}{2\bar{n}k_0} (\nabla_{\perp} - i \nabla_{\perp} \theta)^2 F_R(Z) - \partial_Z \theta F_R(Z) - \frac{\pi}{\Lambda} F_L(Z), \quad (3.38)$$

$$i \partial_Z F_L(Z) = -\frac{1}{2\bar{n}k_0} (\nabla_{\perp} + i \nabla_{\perp} \theta)^2 F_L(Z) + \partial_Z \theta F_L(Z) - \frac{\pi}{\Lambda} F_R(Z). \quad (3.39)$$

So in this case, we find the following expressions for the scalar potential and the gauge field:

$$\mathbf{A} = -i \nabla_{\perp} \theta \sigma_z, \quad (3.40)$$

$$\mathbf{V} = -\nabla_Z \theta \sigma_z - \frac{\pi}{\Lambda} \sigma_x. \quad (3.41)$$

Table 3.1: Summary of SVEA

	Fast scales	Slow scales	\mathbf{V}	\mathbf{A}
case I	λ, Λ	Z_R	$-(\partial_z \theta) \mathbf{S}(z) + \frac{1}{2\bar{n}k_0} [i(\partial_z^2 \theta) \mathbf{S}(z) + (\partial_z \theta)^2]$ $\frac{w}{Z_\theta} \ll 1$ $-(\partial_z \theta) \mathbf{S}(z)$	$-(\nabla_\perp \theta) \mathbf{S}(z)$
case II	λ	Λ, Z_R	$\nabla_Z \theta \sigma_z - \frac{\pi}{\Lambda} \sigma_x$	$-i \nabla_\perp \theta \sigma_z$
case III	λ, Z_R	Λ	---	---

Low birefringence limit

The third physically relevant regime occurs when the birefringence vanishes. According to Eq.(3.6), this implies that the beat length, Λ is slow even with respect to the Rayleigh length. Thus, we would expect that the polarization dynamics does not affect the defocusing of light and hence its confinement within a waveguiding region. In this sense, this limit is not of interest in the waveguiding regime we are looking for. In other words, the variations of the nematic texture in this regime are so slow that they do not have an effect on the light ray's propagation and its expansion.

We conclude this section by summing up the discussion on the fast and slow scales in the Table. 3.1.

3.5.3 Floquet theory for a periodically driven system

The physical systems we study here are examples of periodically driven systems which are vastly studied in the context of Floquet theory. A periodically driven quantum mechanical system is described by a time-periodic Hamiltonian $H(t+T) = H(t)$ [61, 79]. However, the examples of such systems are not restricted to quantum mechanics. Namely, the z -periodic photonic liquid crystal system that we study is described by an effective paraxial equation, Eq. 3.14, that can be mapped to a time-periodic Schrödinger equation. Here we review some of the most basic ideas behind the Floquet theory and study its application in our system.

The time-dependent Schrodinger equation $i\partial_t |\phi(t)\rangle = H(t) |\phi(t)\rangle$ is solved as follows;

$$|\phi(t)\rangle = U(t, t_0) |\phi(t_0)\rangle, \quad (3.42)$$

where the evolution operator is given by the following time-ordered integral

$$U(t, t_0) = \mathcal{T} \exp \left(i \int_{t_0}^t H(t') dt' \right). \quad (3.43)$$

For a time periodic Hamiltonian the evolution operator is also periodic, namely

$$U(t_2, t_1) = U(t_2 + T, t_1 + T), \quad (3.44)$$

and thus, for $\tau \in [0, T]$ and for any integer n

$$U(\tau + nT) = U(\tau) [U(T)]^n, \quad (3.45)$$

where we set the initial time t_0 to zero. Therefore, the full evolution of the wavefunction can be characterized by the evolution operator in one time period. Particularly for large time scales the wavefunction time evolution is in the stroboscopic picture given by the set of wavefunction at the time periods $\{|\phi(nT)\rangle = [U(T)]^n |\phi(0)\rangle\}_n$. The advantage of using the stroboscopic picture is that it contains the relevant information about the wavefunction dynamics for time scales much larger than the Floquet period T . For example, although the time dependence of the Hamiltonian does not allow for an eigenmode of the full evolution operator, in the stroboscopic picture the eigenmodes of the evolution operator over one time period are the eigenstates of the full evolution.

Furthermore, for a system described by a Hermitian Hamiltonian, $U(T)$ is a unitary operator and thus its eigenvalues are given by $e^{i\beta T}$, where β is called quasi-energy and is defined modulo $2\pi/T$. Therefore, the stroboscopic evolution of the eigenstate u is given by

$$|\phi(nT)\rangle = e^{in\beta T} |\phi\rangle. \quad (3.46)$$

In the photonic system under study, these eigenstates are associated with the guided modes of the system. Also, the eigenvalues are quasi-momenta in this case, as the effective time is actually of a spatial origin in this problem and the periodicity of the system is set by the length Λ . Note that the validity of this result for the photonic system depends on the condition that the dynamics of the wavefunction inside a Floquet period is small enough that the effective paraxial equation is always a valid description. This condition is satisfied in the adiabatic regime where the Floquet period is much smaller than the Rayleigh length, that is given by Eq. 3.4. This result implies that there are higher order guided modes with non-Gaussian distributions which are guided in a non-uniform uniaxial media, as shown by Fig. 3.1.

Representation in the Sambe space

We saw above that to obtain the guided modes of a periodic liquid crystal structure we need to solve the diagonalization problem

$$U(t_0 + T, t_0) |\phi(t_0)\rangle = e^{i\beta T} |\phi(t_0)\rangle. \quad (3.47)$$

Since $U(t_0 + T, t_0)$ is a unitary operator, its eigenvalues are all located on the circumference of the unit circle. It thus become likely that for high resolution simulation boxes, the different modes of the system have very close quasi-energies and become practically degenerate. A numerical scheme then can become unstable due to these artificial degenerate spaces. To solve this issue, we use the Floquet Hamiltonian's Sambe-space representation, which is a time-independent equivalent problem to solving the time-periodic quantum-mechanical system [176].

This method requires writing the Hamiltonian in the Sambe space, which is an enlarged space composed of the sidebands of the Floquet Hamiltonian [50]. The eigenvalue problem above then can be expressed in this space as

$$\mathcal{H}^S |\mathcal{U}\rangle = \beta |\mathcal{U}\rangle, \quad (3.48)$$

where \mathcal{H}^S is the Sambe Hamiltonian whose blocks are given by the Fourier components of the Floquet Hamiltonian $H(t) - i\partial_t$ as

$$\mathcal{H}_{IJ}^S = H^{(I-J)} - I\delta_{I,J}\omega, \quad (3.49)$$

where $I, J \in \mathbb{Z}$, $H^{(p)}$ is the p th Fourier harmonic of the Hamiltonian, $\delta_{I,J}$ is the Kronecker delta, and ω is the drive frequency. The eigenstate $|\mathcal{U}\rangle$ is also obtained by the column stacking of the Fourier components of the periodized wavefunction $|u\rangle^\clubsuit$:

$$|\mathcal{U}\rangle = \begin{pmatrix} \cdot \\ \cdot \\ \cdot \\ |u\rangle^{(I-1)} \\ |u\rangle^{(I)} \\ |u\rangle^{(I+1)} \\ \cdot \\ \cdot \\ \cdot \end{pmatrix}. \quad (3.50)$$

[♣]This can be obtained from a Floquet eigenstate as $|u_\alpha(t)\rangle = V(t) |\phi_\alpha\rangle$, where $V(t)$ is the short-term (within a Floquet period) propagator.

Note that the eigenvalues of this method can have arbitrary norms that solves the issue that we described above: the two eigenvalues β_0 and $\beta_0 + \epsilon + 2n\pi$ where ϵ is small with respect to the resolution of the diagonalization code are in this method well separated from each other, while in the previous method they were pointing to very close points on the unit circle which could lead to accidental degeneracies.

We skip the details of the calculations of \mathcal{H}^S for the various cases that we consider in this thesis. We solve the time-independent problem above numerically using usual diagonalization methods. To find the lowest order guided modes, we look for the maximally spatially localized modes that are obtained from the eigenmodes of the Sambe Hamiltonian.

Chapter 4.

Liquid-crystal-based photonic topological insulators



Topological photonics harnesses the physics of topological insulators to control the behavior of light. Photonic modes robust against material imperfections are an example of such control. In this chapter, we propose a soft-matter platform for assembling topological photonic materials that hold promise for protected unidirectional waveguides, sensors and lasers [17]. The orientation of liquid crystal molecules introduces an extra geometric degree of freedom which in conjunction with suitably designed structural properties leads to the creation of topologically protected states of light. The use of soft building blocks potentially allows for reconfigurable systems that exploit the interplay between light and the soft responsive medium.

Topological materials are a class of structured materials that exhibit remarkable features such as the existence of chiral edge states robust against backscattering at their boundaries. These materials inspired from topological insulators [100] have proven ubiquitous in physics, including examples in photonics [17, 18, 26, 83, 85, 86, 88], mechanics [15, 33, 52, 67, 68, 73], hydrodynamics [19, 20, 38, 46], stochastic systems [42] and electrical circuits [29, 59, 69]. The unique properties of topological photonic materials suggest several potential applications [17, 18, 83] ranging from high-power single-mode lasers [25, 27] to slow light [14].

In this chapter, we show how liquid crystals can be used as a soft-matter platform to realize the building blocks of topological photonics [17, 18, 83]. In the previous chapter, we developed a strategy purely based on liquid crystals where the orientation of the nematic molecules, described by their director field, is used to realize waveguiding [40, 47, 56]. Here, we use the same degrees of freedom in these materials to build Floquet topological materials [36, 41, 88] by coupling these waveguides.

We first develop a tight-binding model (coupled-modes description) for the coupled liquid-crystal waveguides [177]. We establish its domain of validity through a careful comparison with direct simulations of Maxwell equations. Along with a precise analysis of the symmetries in the system, these results allow us to engineer a liquid-crystal realization of two archetypal topological systems: a system with non-trivial winding numbers analogous to the one-dimensional Su-Schrieffer-Heeger (SSH) model [36, 172] and a system with non-trivial Chern numbers inspired by the two-dimensional Haldane model [151].

In Ref. [88] it was demonstrated that periodic modulations induced by helix-shaped waveguides allow one to implement photonic Floquet topological insulators. In a curved waveguide, the change in the local direction of propagation leads to geometric phases [13, 161] called Rytov-Vladimirskii-Berry phases [188, 189], which are eventually responsible for the existence of the photonic topological insulator in Ref. [88]. In contrast, the geometric phases present in our liquid-crystal system are Pancharatnam-Berry phases [155, 186] and stem from the change in the local optical axes. As a consequence, the symmetries of the photonic topological material are entirely controlled by the spatial symmetries of the nematic texture.

4.1 Coupled liquid crystal waveguides

In the previous chapter, we studied soft photonic waveguides in a liquid crystal medium. We now consider a system that consists of two such waveguides by transversely repeating the director modulation which corresponds to one waveguide, see Fig. 4.1(a). When two of these waveguides are located close to each other, they become coupled as light can tunnel from a waveguide to another through evanescent waves: the electromagnetic field inside one waveguide induces a field inside the other one. Fig. 4.1(c) shows that if a

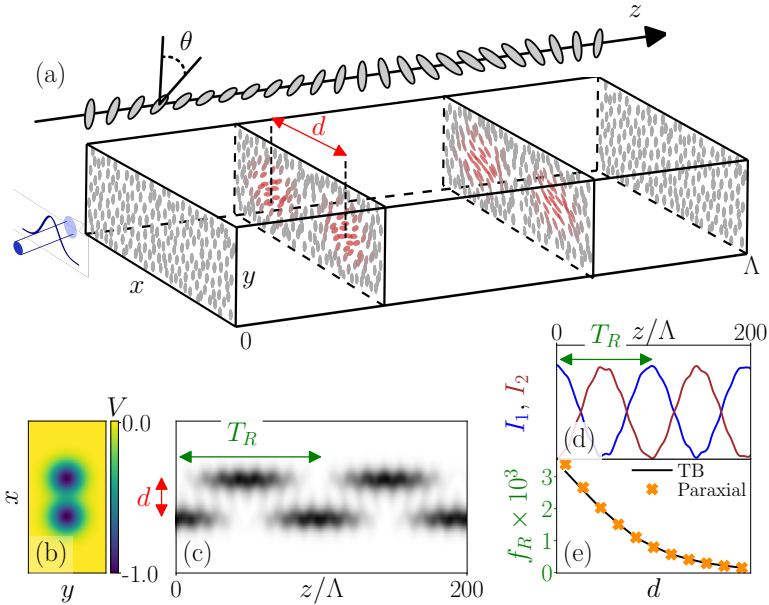


Figure 4.1: Coupling of two waveguides, corresponding to the liquid-crystal pattern in (a) and with an effective optic potential shown in (b). The z -axis in (a) shows the orientation of the molecules in the centre of a waveguide for one Floquet period, given by Λ . (c)-(d) The intensity profile obtained with the guided mode of one of the waveguides as an initial condition shows an oscillatory pattern, which is reminiscent of Rabi oscillations in two-level quantum systems. (e) Dependence of the dimensionless Rabi frequency $f_R = \lambda/T_R$ with the distance between waveguides for both the continuum paraxial simulations and the tight-binding method. The effective interaction between two such waveguides, proportional to f_R , decays exponentially with their distance.

guided mode is initially inside one of the two identical waveguides, it will eventually leak into the other one. The light intensity pattern obtained from such interaction oscillates sinusoidally with a period T_R (see Fig. 4.1(d)) exactly like Rabi oscillations in two-level quantum systems.

We wish to consider a system made of a large number of coupled waveguides. To do so, we need a simplified description of the waveguides and of their couplings, that allows to capture the essential features of the system (such as the Rabi oscillations described above) without having to describe the full liquid crystal configuration. Hence, we use a time-dependent Hückel method [34, 191] to develop a tight-binding model for the photonic waveguides (see appendix 4.6.2). The tight-binding (TB) Hamiltonian H^{TB} obtained using this method for the evolution of a system of N waveguides reads

$$i\partial_z |\psi_n\rangle = \sum_{m=1}^N H_{nm}^{\text{TB}}(z) |\psi_m\rangle, \quad (4.1)$$

where ψ_n is the mode inside waveguide n . This tight-binding model brings the essential simplicity that is needed to analyze a system with many coupled waveguides such as a lattice configuration. The Rabi oscillations obtained from this tight-binding model for a two-waveguide system are in agreement with the solutions of the Schrödinger equation (3.14) in the continuum using appropriate initial conditions, validating our approach, see Fig. 4.1(e). Using this tight-binding model, we further quantify the interaction between two such waveguides and observe that its strength decays exponentially with respect to the distance between them, see Fig. 4.1(e).

4.2 Photonic crystals in 1+1d: SSH chain

A lattice of coupled waveguides is obtained by a periodic patterning of the nematic director in the transverse plane. Here, we consider a 1+1d lattice, where the second dimension stands for the paraxial direction z that plays the role of time in this system. We consider a system inspired by the Su-Schrieffer-Heeger (SSH) model [36, 172]. Using the interaction-distance dependence from the previous section, we design a lattice of these waveguides on a chain so that the interaction between two neighboring waveguides changes in an alternating way, as shown in Fig. 4.2(a-b). The distance between waveguides is chosen such that the ratio between the two different hopping amplitudes is $J_-/J_+ = 0.25(1)$.

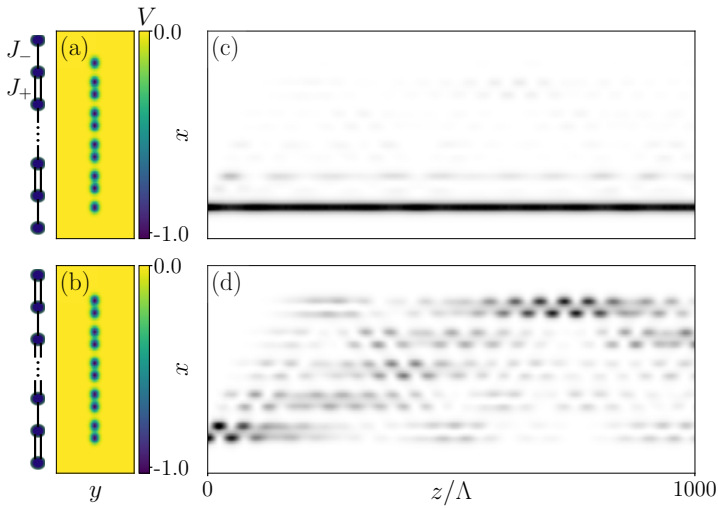


Figure 4.2: An SSH chain of photonic waveguides in a liquid crystal medium. (a)-(b) The effective photonic potential for two topologically distinct dimerizations of the waveguides in such a system which correspond to an SSH chain with and without an edge mode, respectively, as shown in (c)-(d). The effective tunneling between these waveguides is controlled by their distance as illustrated in Fig. 4.1(e). Insets in panels (a)-(b) sketch an SSH chain corresponding to each system. Strong (J_+) and weak (J_-) couplings are shown by double and single bonds, respectively. (c) The propagation of an edge mode whose existence is topologically protected. (d) Shows the scattering into the bulk of the same initial mode in a trivial chain.

Figure 4.2(a-b) also shows that depending on the ordering of the strong and weak bonds at the boundary, there are two different dimerizations of the neighboring waveguides. The tight-binding description of the system in Fig 4.2(a-b) is a time-dependent version of the SSH chain [172]. We find a photonic state that remains at the edge of one of the two configurations of this system, as shown in Fig. 4.2 (c), whereas in the other configuration, in panel (d), the initial mode at the edge leaks into the bulk while it propagates forward. The intensity profile of the localized edge mode shows an exponential decay away from the waveguide at the boundary.

The presence of this edge mode is due to the topology of the Hamiltonian describing the system, which is characterized by an integer winding number across the Brillouin zone (BZ). To see this, note that the dimerized chain's tight-binding Hamiltonian in the momentum space is in general a 2×2 matrix (due to two sublattices) and can be cast as

$$H(\mathbf{k}) = \mathbf{d}(\mathbf{k}) \cdot \boldsymbol{\sigma} + \epsilon \mathbf{I}, \quad (4.2)$$

where $\boldsymbol{\sigma} = (\sigma_x, \sigma_y, \sigma_z)$ is a vector of Pauli matrices, \mathbf{d} is a vector in the momentum space, and ϵ is the onsite energy term. When sublattice symmetry is preserved, $d_z = 0$ and

$$w = \frac{1}{2\pi i} \int_{\text{BZ}} d^2\mathbf{k} \ln \mathbf{d}(\mathbf{k}) \quad (4.3)$$

counts the number of windings of \mathbf{d} over the BZ. Since $\mathbf{d}(\mathbf{k})$ is a periodic function, the integration is performed over a closed loop, and thus the parameter w is integer valued and characterizes the topology of the Hamiltonian. For the SSH chain, we find that $w = 1$ for the topological and $w = 0$ for the trivial system. In this particular case, this topological invariant depends on whether J_- is smaller or greater than J_+ , which explains why this edge mode is present in only one of the two configurations in Fig. 4.2.

4.3 Symmetries and topological modes in 2+1d

So far, we only considered systems in which there is a symmetry between the photonic modes that propagate forwards and backwards along the z direction. This z -reversal symmetry corresponds to time-reversal (TR) symmetry in the effective quantum picture. We would now like to explore the phenomena that can arise with introducing an asymmetry in this direction. The TR symmetry acts on Eq. (3.14) through the operator $T = \sigma_z \Theta$, where Θ

is complex conjugation and where the Pauli matrix σ_z exchanges right and left circular polarizations. It follows that a configuration is TR invariant if there is a reference point z_0 such that the orientation of the directors satisfies $\theta(z_0 - z) = -\theta(z_0 + z)$ (see appendix 4.6.3).

In the tight-binding model of this system, we focus on the subspace of guided modes, since the unguided ones do not follow a coupled-mode picture. In this reduced description, the TR operator is simply the complex conjugation operator Θ . We prove analytically in the appendix 4.6.3 that the TR invariance in the paraxial Hamiltonian leads to the TR invariance of the tight-binding model.

We break TR symmetry by considering the director field configuration

$$\theta(x, y, z) = \theta_0(x, y) [\sin \Omega z + \eta \cos(2\Omega z - \varphi)], \quad (4.4)$$

where $\theta_0(x, y)$ describes the nematic pattern in the transverse plane (it is a sum of Gaussians centred at desired positions), $\Omega = 2\pi/\Lambda$ is the frequency of the drive (an inverse length scale here), η is a dimensionless coefficient that controls the strength of the TR symmetry breaking, and φ is the dephasing between the harmonics of the pattern. We focus on configurations of these waveguides in 2+1 dimensions where the absence of TR invariance can lead to topological modes [17, 88, 151]. A 2+1d lattice of these waveguides can be designed by considering transverse modulations of the nematic directors that are periodic in two directions. We consider a modulation that creates a honeycomb lattice of such waveguides in the transverse plane, as shown in Fig. 4.3(a).

We find that in our Floquet model, the TR symmetry breaking is not sufficient to get a topological band structure. This can be understood through a high-frequency Magnus expansion [61] of a general Floquet tight-binding Hamiltonian on a honeycomb lattice, by mapping the obtained effective Hamiltonian with that for the Haldane model [151] (see appendix 4.6.4). We find that breaking the three-fold symmetry between the three neighboring bonds is required to get a non-zero Haldane mass at the first order of the expansion. Many Floquet driven models involve a rotating gauge field, arising for example from the coupling with a circularly polarized light radiation [80] or an effective gauge field originating from spin-orbit coupling of light on a helical waveguide [88]. In this case, the rotating gauge field effectively breaks the C_3 symmetry via a Peierls substitution in the hoppings.

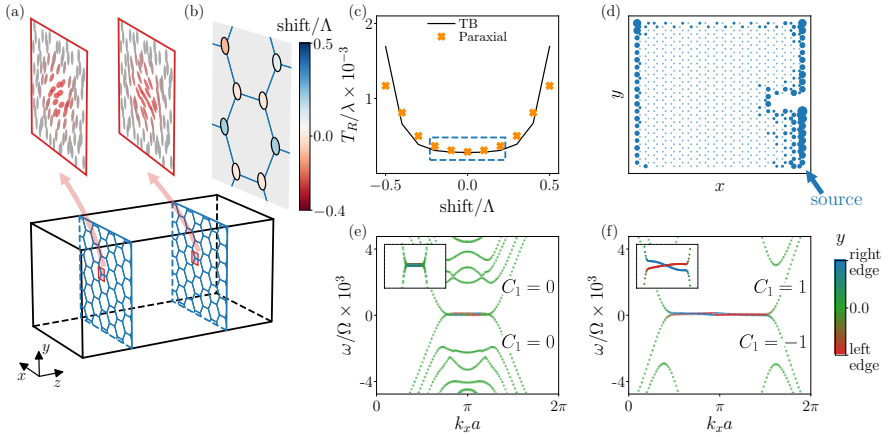


Figure 4.3: (a) A photonic lattice on a honeycomb structure that is obtained by patterning of the nematic directors in the transverse plane. Each node of the lattice corresponds to a photonic waveguide, as shown in the zoomed-in panels. (b) A unit cell of this photonic lattice, where the waveguides are colored according to their relative phase shift in the z -direction. The unit cell is enlarged with respect to the honeycomb one because of the different phase shifts. (c) The Rabi period between two photonic waveguides as a function of the relative shift between them. We focus on the parameter space enclosed by the blue dotted rectangle, where there is a close agreement between the tight-binding model and the continuum paraxial simulations. (d) Evolution of a topological edge mode on the projected $x - y$ plane. The size of each circle corresponds to the light intensity on that site. This mode propagates along the edge without backscattering on obstacles. (e)-(f) One sideband in the Floquet band structure of a honeycomb lattice of photonic waveguides (e) without and (f) with relative phase shift. In both cases the TR symmetry is violated using the structural parameter $\eta = 0.67$. The band structure in (f) shows the presence of one mode at the right (blue) and left (red) edge of this system for a range of transverse momenta in the BZ. The presence of these edge modes and their unidirectional propagation are predicted by the difference between first Chern numbers C_1 of the bands which are separated by the gap.

Here, we do not have access to such a rotating gauge field. Instead, we break this symmetry by shifting the waveguides along the z -axis, with a shift that is different for each of the neighboring waveguides, see Fig. 4.3(b). The relative shift of waveguides affects both the strength of their interactions, as shown in Fig. 4.3(c), and induces a dephasing between the hoppings. We choose a spatially periodic configuration of phase shifts. However, the unit cell is enlarged with respect to the hexagonal lattice, as shown in Fig. 4.3(b) where the colors represent the shifts.

We note that the tight-binding description is only reliable when the shifts are small enough, see Fig. 4.3(c). We use the guided mode of each waveguide as a basis for the tight-binding description. This works well when the waveguides are not shifted. When they are, our procedure does not span the whole space where the modes evolve when the waveguides are shifted, because the guided modes of waveguides with relative shifts are different: the guided mode of one waveguide can be repelled from a similar waveguide with a relative shift of origin. In the following, we focus on the range of shifts where the tight-binding description still provides a reliable approximation (blue dashed rectangle in Fig. 4.3(c)).

The band structures associated with the tight-binding model of the lattices of waveguides in Fig. 4.3(a-b) on a cylinder are shown in panels (e)-(f). Panel (e) corresponds to a honeycomb lattice of waveguides without relative phase shifts. Panel (f) corresponds to the unit cell shown in panel (b), where the waveguides are shifted with respect to each other. In this case, we observe chiral modes localized at the edges of the cylinder. A direct calculation of the first Chern number [100, 121, 169] (given by Eq. 1.8) of the top and bottom bands shows that these edge modes have a topological origin. They circulate unidirectionally along the edge in the transverse plane as they propagate along the z -direction despite the presence of a defect at the boundary, see Fig. 4.3(d). The decay length of the edge modes in the bulk is related to the inverse size of the bulk band gap in which these modes reside, compared to the frequency of the Rabi oscillation. Thus, we find that the decay length is only a few lattice sites, even though the gap is very small with respect to the Floquet frequency.

4.4 Non-Hermitian description of shifted waveguides

A full description of the photonic crystal should encompass both guided and repelled modes. The analysis above shows that waveguides shifted with respect to each other can be coupled. In this situation, both the guided and repelled modes should be taken into account. In principle, this would entail the use of a non-Hermitian Hamiltonian [133] to describe the system, to account for the loss of light intensity due to the repelled light (eventually converted to heat in the bulk of the material). In this section, we provide details about the coupling between waveguides with relative shifts.

In particular, we show that an effective Hermitian description of the coupled waveguides is still possible in the regimes considered above. There is effectively no coupling between the guided and repelled modes, despite the difference between guided modes of the relatively shifted waveguides. Fig. 4.4 shows simulation results for the two coupled shifted waveguides with $\eta = 0.67$ and $\delta = 1$, where the distance between the two waveguides is given by $2w_p + \delta$. As can be seen in the figure, there is a drastic change in qualitative behavior of the intensity patterns depending on the relative shift between the waveguides.

To understand this qualitative difference, we now determine the effective coupling between these relatively shifted waveguides. As we saw in Fig. 4.3, the Hückel method fails to fully account for the couplings when the relative shift between the waveguides is close to $\Lambda/2$. Therefore, we extract the effective Hamiltonians directly from the intensity patterns. We restrict ourselves to extracting these parameters from the intensities and not from phases, since the latter would require projection of the temporal modes inside each waveguides into a basis of a linear combination of both waveguides' guided modes. We start with the following ansatz for the effective Hamiltonian:

$$H = -i\epsilon\mathbb{I} + (J_x\sigma_x + J_y\sigma_y) + (m + i\eta)\sigma_z \quad (4.5)$$

in which the basis vectors $[1, 0]^T$ and $[0, 1]^T$ correspond to the two waveguides. We consider real values for J_x and J_y for now. A more complicated model with non-reciprocal couplings would require loosening this condition, but we will see that it is not necessary in our system. When the initial condition is corresponds to the guided mode of the first waveguide, the evolution is given by

$$|\psi_1(t)\rangle = U(t) \begin{bmatrix} 1 \\ 0 \end{bmatrix} = e^{-\epsilon t} \begin{bmatrix} \cos tJ + i\frac{m}{J} \sin tJ \\ -i\frac{J_x\sigma_x + J_y\sigma_y}{J} \sin tJ \end{bmatrix}. \quad (4.6)$$

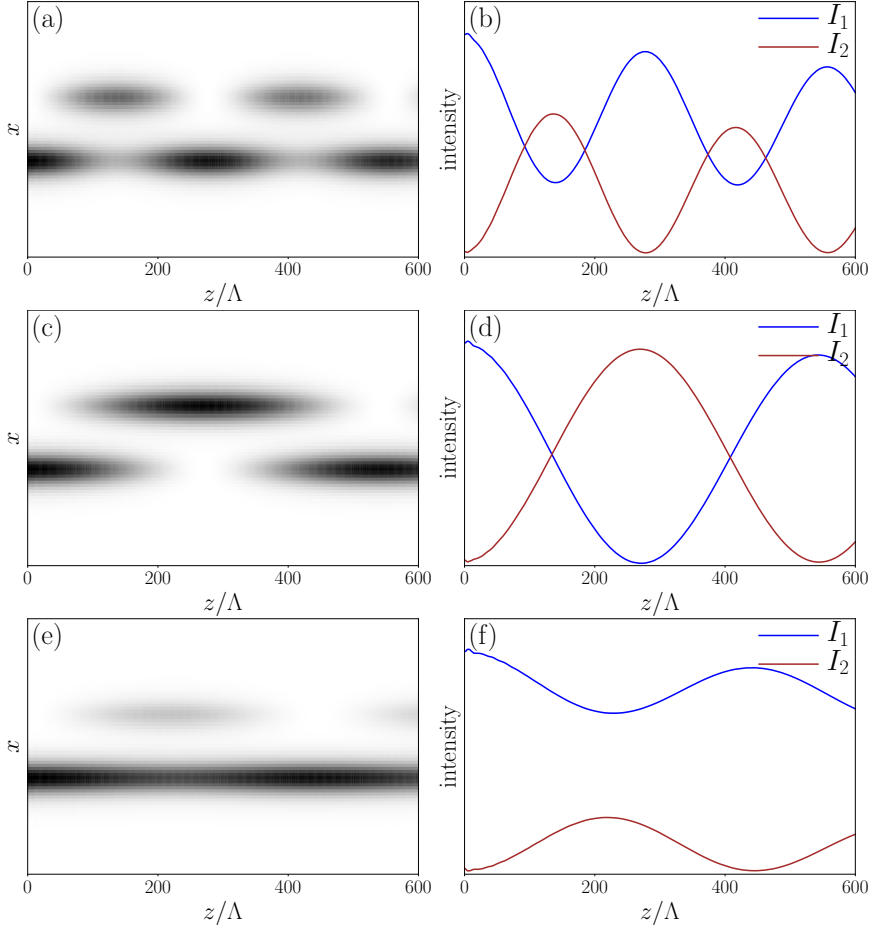


Figure 4.4: Coupling between waveguides with relative shifts. Left panels show the intensity profile of the couplings and right panels compare the total intensity in the two waveguides. The relative shift between waveguides is 0.3Λ for (a)-(b), 0.4Λ for (c)-(d), and 0.5Λ for (e)-(f).

The mode intensity inside the second waveguide is

$$|\langle [0, 1]^T | \psi_1 \rangle|^2 = e^{-2ct} \frac{J_x^2 + J_y^2}{J_r^2 + J_c^2} (\sin^2 J_r t + \sinh^2 J_c t), \quad (4.7)$$

where J_r and J_c are the real and imaginary parts of the effective hopping determined by

$$J_r + iJ_c = \sqrt{(m + i\eta)^2 + J_x^2 + J_y^2}. \quad (4.8)$$

By fitting Eq. (4.7) to the intensity pattern obtained from the system's evolution in the paraxial regime, we can obtain η , m , J_r , J_c , and $j = |J_x + iJ_y|$. m and η are determined by solving

$$(m + i\eta)^2 = (J_r + iJ_c)^2 - j^2, \quad (4.9)$$

$$(m - i\eta)^2 = (J_r - iJ_c)^2 - j^2. \quad (4.10)$$

We obtain these parameters for three different waveguide distances and for $\eta = 0.67$ and shift/ $\Lambda = 0.5$ for a simulation on a period of 6000Λ . The results are summarized in Table 4.1.

Table 4.1: Quantities characterizing the coupling between waveguides with relative shifts.

δ	ϵ	m	η	j	$ \det U $
0.0	$3.2e-5$	0.0021	0.	0.0049	1.0
1.0	$3.5e-5$	0.0013	$3.0e-5$	0.0019	0.99997
2.0	$3.9e-5$	0.0013	$2.9e-5$	0.0007	0.9998

In the last column we calculate the absolute value of the determinant of the matrix of eigenvectors: $U = (|\psi_1\rangle, |\psi_2\rangle)$. If H is Hermitian, $|\det U| = 1$. In our system, the deviation from unity is very small. Based on this result, we conclude that the non-Hermitian effects in our system should be negligible. The peculiar behavior in the intensity patterns of Fig. 4.4 is due to the Hermitian mass term (with a real mass m), which becomes comparable to the hopping amplitude j .

We have then verified that non-Hermitian effects involving non-orthogonal eigenmodes are negligible in the topological system described in the previous section, validating our approach based on Hermitian topological invariants. Looking forward, the natural occurrence of non-Hermiticity in the description suggests liquid crystal-based soft waveguides as a promising platform for non-Hermitian optics [16, 39, 91, 103].

4.5 Conclusion

In this chapter, we have shown how to realize photonic Floquet topological systems using liquid crystals. As an example, we have shown how Floquet versions of the SSH and Haldane models can be realized. As photonic crystals, these photonic Floquet topological insulators are semimetal phases with a

strong anisotropy; for instance, a $(2 + 1)$ -dimensional Chern insulator can be seen as a photonic Weyl material [43, 65]. Our analysis based on a reduction of the paraxial wave equation to a tight-binding description provides a blueprint to design photonic structures with targeted topological properties in liquid crystal systems through Pancharatnam-Berry phases.

Our proposal is inspired by recent advances in liquid crystal technology that make it possible to effectively print out any target director field either by stacking two-dimensional photoaligned slices [22, 28, 48, 51, 56, 94, 112] or through three-dimensional photopatterning techniques [116]. Electrically controlled and light-driven liquid crystals [48, 107] could be further exploited to engineer reconfigurable topological photonic devices.

Also, the TR symmetry can be broken using the fully rotating nematic fields given by Eq. 3.19. Using this approach introduces a handedness that breaks the symmetry between forward- and backward-moving modes. Furthermore, the handedness introduces a second effective vector potential by moving into a rotating frame [88]. The consequences of such symmetry breaking terms are a subject for further investigations.

4.6 Appendix

We now provide details for the information for the realization of the model in an actual liquid crystal environment, a derivation of the tight-binding model, symmetries of the photonic crystal system, and non-Hermitian effects in the interaction of waveguides with relative shifts in their origin.

4.6.1 Liquid crystal configuration

The waveguiding in the system under study is achieved when the following modulation for the director field is used [56]:

$$\theta(x, y, z) = \exp\left[-\frac{x^2 + y^2}{w_p^2}\right] \sin\left(\frac{2\pi z}{\Lambda}\right), \quad (4.11)$$

where w is the width of the Gaussian pattern. The effective gauge and scalar fields are then determined as

$$\mathbf{A} = \frac{2(x\hat{x} + y\hat{y})}{w_p^2} \exp\left[-\frac{x^2 + y^2}{w_p^2}\right] \sin\left(\frac{2\pi z}{\Lambda}\right) \mathbf{S}(z), \quad (4.12)$$

$$\mathbf{V} = -\frac{2\pi}{\Lambda} \exp\left[-\frac{x^2 + y^2}{w_p^2}\right] \cos\left(\frac{2\pi z}{\Lambda}\right) \mathbf{S}(z). \quad (4.13)$$

Note that the configuration is chosen to be periodic after each beating length. Considering Eq. 3.10, it follows that this feature of the liquid crystal structure leads to a z -periodic Hamiltonian in the right-hand side of Eq. 3.14. Therefore, this system can be studied using the machinery of the Floquet Hamiltonians [56].

Note also that the mode evolution equations of this system are linear in θ . Therefore, one can build a lattice of the waveguides above by repeating the modulation of one waveguide, Eq. 4.11, in the transverse plane. For example, a 1-d SSH chain is described by

$$\theta(x, y, z) = \sum_{i=1}^N \theta_i(x, z), \quad (4.14)$$

with

$$\theta_i(x, z) = \sin\left(\frac{2\pi z}{\Lambda}\right) \times \left(\exp\left[-\frac{[x - (x_i - d_1/2)]^2}{w_p^2}\right] + \exp\left[-\frac{[x - (x_i + d_1/2)]^2}{w_p^2}\right] \right), \quad (4.15)$$

where $x_i = x_0 + (i - 1)(d_1 + d_2)$ are the positions of the centre of pairs of potentials in terms of the alternating distances between the neighboring waveguides, d_1 and d_2 .

4.6.2 Floquet tight-binding model

To build-up a lattice model for a photonic crystal in this system, we exploit the Floquet tight-binding approach. We start by writing down the many-waveguide wavefunction $|\Phi\rangle$ as a linear combination of single-waveguide modes $|\phi_I\rangle$ as follows:

$$|\Phi(z)\rangle = \sum_I a_I(z) |\phi_I(z)\rangle, \quad (4.16)$$

where $\phi_I(z)$ is obtained by the evolution of the guided mode inside the waveguide I . The validity of this approximation can be determined by the closeness of the dynamics of this wavefunction to the actual system's evolution. Plugging the wavefunction above into the Schrödinger equation of the system

leads to

$$\begin{aligned} H |\Phi(z)\rangle &= i\partial_z |\Phi\rangle \\ &= \sum_J [i\partial_z(a_J(z)) |\phi_J(z)\rangle + ia_J(z)\partial_z |\phi_J(z)\rangle]. \end{aligned} \quad (4.17)$$

We can now multiply both sides of this equation with $\langle\phi_J|$ to obtain

$$\begin{aligned} &\sum_I i \langle\phi_J|\phi_I\rangle \partial_z a_I \\ &= \sum_I \langle\phi_J| H |\phi_I\rangle a_I - \sum_I \langle\phi_J| i\partial_z |\phi_I\rangle a_I. \end{aligned} \quad (4.18)$$

This result can be written as

$$i\partial_z a = S^{-1}(H - R)a, \quad (4.19)$$

where $a = (a_1, a_2, \dots)$ is a vector in the basis of waveguides, and the matrix elements in this basis are

$$S_{JI} = \langle\phi_J|\phi_I\rangle, \quad (4.20)$$

$$H_{JI} = \langle\phi_J| H |\phi_I\rangle, \quad (4.21)$$

$$R_{JI} = \langle\phi_J| i\partial_z |\phi_I\rangle. \quad (4.22)$$

Note that these matrices act on the space of guided modes, not on the space of light polarizations. When starting the coupled-mode theory in Eq. 4.16, we project the initial model into the space of the guided modes, which is a one-dimensional subspace of the polarization space. The effective tight-binding Hamiltonian associated with the continuous problem is then

$$H_{\text{TB}} = S^{-1}(H - R). \quad (4.23)$$

4.6.3 Time-reversal symmetry

In this section we consider the time-reversal symmetry (TRS) of the effective Schrodinger equation that describes the light propagation in this system. Here we are interested in the behaviour of systems under the inversion of the effective time by the operation $T : z \rightarrow -z$. A system is invariant under TRS if there is a z_0 such that

$$TH(z_0 + z)T^{-1} = H(z_0 - z). \quad (4.24)$$

We first look at the physical set-up that gives a time-reversal invariant system and then derive the tight-binding version of the Eq. (4.24).

TRS in real space

The question we would like to answer first is that what features of the liquid crystal system will lead to its invariance under time-reversal. A difficulty in defining a proper time-reversal (TR) operator arises when we notice that the light beam dynamics in this system is extremely affected by its initial polarization. Especial cases of guided and repelled modes for the right/left circularly polarized (RCP/LCP) initial conditions are studied in [56]. To avoid potential problems related to this issue, we pick up a TR operator that preserves LCP and RCP lights so that we can study the effect of this operator in the projected space of initial conditions with certain polarization [♣]. This projection can be done by using

$$T = \sigma_z \Theta, \quad (4.25)$$

where $\sigma_z = \text{diag}(1, -1)$ is the third Pauli matrix and Θ is the complex conjugation operator. It then follows that $T\psi_{\text{R,L}} = \psi_{\text{R,L}}$. Thus, if the initial polarization of the light beam is a linear combination of the LCP/RCP polarizations (with real coefficients), we have

$$T |\psi(0)\rangle = |\psi(0)\rangle. \quad (4.26)$$

Now note that the system's wavefunction evolution is given by $|\psi(z)\rangle = U(z) |\psi(0)\rangle$, where

$$U(z) = \lim_{\delta z/z \rightarrow 0} \prod_{n=0}^{\lfloor z/\delta z \rfloor} \exp(-i\delta z H(z - n\delta z)) \quad (4.27)$$

The time reversal of the wavefunction is

$$\begin{aligned} T |\psi(z)\rangle &= T \lim_{\delta z/z \rightarrow 0} \prod_{n=0}^{\lfloor z/\delta z \rfloor} \exp(-i\delta z H(z - n\delta z)) T^{-1} T |\psi(0)\rangle \\ &= \lim_{\delta z/z \rightarrow 0} \prod_{n=0}^{\lfloor z/\delta z \rfloor} [T \exp(-i\delta z H(z - n\delta z)) T^{-1}] T |\psi(0)\rangle \\ &= \lim_{\delta z/z \rightarrow 0} \prod_{n=0}^{\lfloor z/\delta z \rfloor} [\exp(i\delta z H(-z + n\delta z))] |\psi(0)\rangle, \end{aligned} \quad (4.28)$$

[♣]Note that the operator we define does not necessarily work for initial conditions with arbitrary polarization

where in the last line we assumed the time reversal invariance of the system around $z = 0$ as well as the invariance of the initial wavefunction at the same point given by Eq. (4.26). The last line is the wavefunction's evolution backward in time till $-z$. Thus, the above calculation actually gives

$$T |\psi(z)\rangle = |\psi(-z)\rangle, \quad (4.29)$$

where $|\psi(-z)\rangle = U^{-1}(0, -z) |\psi(0)\rangle$. Apart from its convenience, this relation gives a tool to numerically check whether a given system is TR invariant or not.

We now find the physical systems which are invariant under this TR operator. In other words, we want to find configurations of the system such that the Hamiltonian

$$H(z) = -\frac{1}{2} [\nabla_{\perp} + i\mathbf{A}(z)]^2 + \mathbf{V}(z), \quad (4.30)$$

with $\mathbf{A}(z) = -(\nabla_{\perp}\theta)\mathbf{S}(z)$ and $\mathbf{V}(z) = -(\partial_z\theta)\mathbf{S}(z)$ satisfies (4.24). Now if we use

$$\begin{aligned} T\mathbf{S}(z)T^{-1} &= T [\cos(2\pi z/\Lambda)\sigma_y + \sin(2\pi z/\Lambda)\sigma_x] T^{-1} \\ &= \cos(2\pi z/\Lambda)\sigma_y - \sin(2\pi z/\Lambda)\sigma_x \\ &= \mathbf{S}(-z), \end{aligned} \quad (4.31)$$

we will have

$$\begin{aligned} TH(z)T^{-1} &= -\frac{1}{2} [\nabla_{\perp} - i(-\nabla_{\perp}\theta)(-z)\mathbf{S}(-z)]^2 \\ &\quad + (-\partial_z\theta)(-z)\mathbf{S}(-z). \end{aligned} \quad (4.32)$$

Now one can see that an odd θ around any point in z_0 is a sufficient condition for the system to be TR invariant. Thus the system is TRI when there is a z_0 such that

$$\theta(z_0 + z) = -\theta(z_0 - z) \quad (4.33)$$

We thus can break the effective TRS in this system using the orientation field that is given in Eq. 4.4. Fig. 4.5 shows examples of θ fields which preserve or break the TR symmetry.

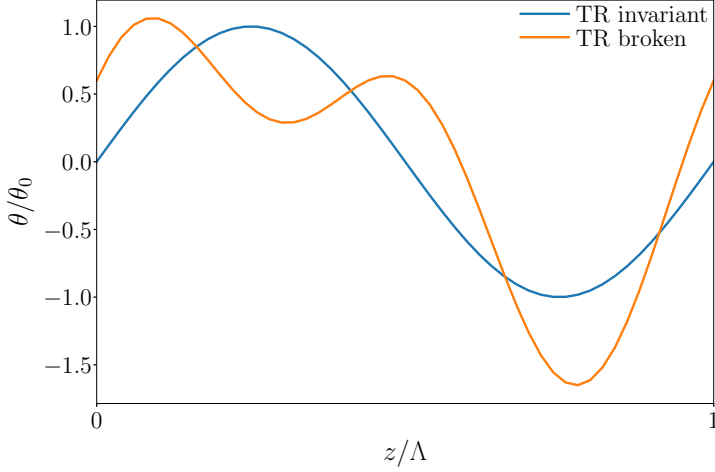


Figure 4.5: Examples of nematic director fields corresponding to TR invariant and broken systems. The TR broken case is obtained from the Eq. 4.24 using $\eta = 0.67$ and $\varphi = \arctan 0.5$.

TRS in tight-binding Hamiltonian

Here, we consider the effect of the time reversal operation in the tight-binding model of the system under study. It is also insightful to understand the implications of a continuous TRS Hamiltonian on the tight-binding version. Here we consider the terms of H_{TB} in Eqs. (4.20) - (4.22) separately. Switching to inner product notation we have for a TR invariant system

$$\begin{aligned}
 S_{JI}(-z) &= (\psi_J(-z), \psi_I(-z)) \\
 &= (T\psi_J(z), T\psi_I(z)) \\
 &= (\Theta\psi_J(z), \Theta\psi_I(z)) \\
 &= (\overline{\psi_J(z)}, \overline{\psi_I(z)}) \\
 &= \overline{(\psi_J(z), \psi_I(z))} = \overline{S_{JI}(z)},
 \end{aligned} \tag{4.34}$$

where the bar means the complex conjugation.

$$\begin{aligned}
 h_{JI}(-z) &= (\psi_J(-z), H(-z)\psi_I(-z)) \\
 &= (T\psi_J(z), TH(z)T^{-1}T\psi_I(z)) \\
 &= (\Theta\psi_J(z), \Theta H(z)\psi_I(z)) \\
 &= (\overline{\psi_J(z)}, \overline{H(z)\psi_I(z)}) = \overline{h_{JI}(z)},
 \end{aligned} \tag{4.35}$$

and

$$\begin{aligned}
R_{JI}(-z) &= (\psi_J(-z), i\partial_z\psi_I(-z)) \\
&= (T\psi_J(z), i\partial_z T\psi_I(z)) \\
&= (\Theta\psi_J(z), i\partial_z\Theta\psi_I(z)) \\
&= (\overline{\psi_J(z)}, -i\partial_z\overline{\psi_I(z)}) \\
&= \overline{(\psi_J(z), i\partial_z\psi_I(z))} = \overline{R_{JI}(z)}.
\end{aligned} \tag{4.36}$$

Thus we conclude that

$$TH(z)T^{-1} = H(-z) \tag{4.37}$$

implies

$$\Theta H_{\text{TB}}(z)\Theta^{-1} = H_{\text{TB}}(-z). \tag{4.38}$$

4.6.4 Why is C_3 -symmetry breaking needed?

Here we would like to consider the effect of the TRS breaking in a Floquet system. The example of such systems is the Floquet photonic topological insulators first proposed and observed by Rechtsman *et al.* [88]. Let us start with a Floquet tight-binding Hamiltonian on a honeycomb lattice. For now, we only consider a nearest neighbour interaction, for which the tight-binding Hamiltonian in the momentum space is given by

$$H(k) = \begin{pmatrix} M & J(\mathbf{k}) \\ J^*(\mathbf{k}) & -M \end{pmatrix}, \tag{4.39}$$

where k is the momentum and M is the mass. Let us consider the massless case $M = 0$. For a Floquet system, the hopping amplitudes in terms of their Fourier components are given by

$$J(\mathbf{k}) = \sum_{\ell \in \mathbb{Z}} J_\ell(\mathbf{k}) e^{i\ell\Omega t} = \sum_{\ell \in \mathbb{Z}} \sum_{j=1}^3 J_{\ell,j} e^{i\mathbf{k} \cdot \delta_j} e^{i\ell\Omega t}, \tag{4.40}$$

where $\delta_{1,2,3}$ are the three neighbouring vectors, and Ω is the drive frequency. We drop the explicit \mathbf{k} dependence notation for now. The Hamiltonian in terms of its harmonics is determined by

$$H = \sum_{\ell \in \mathbb{Z}} H_\ell e^{i\ell\Omega t}, \tag{4.41}$$

$$H_\ell = \begin{pmatrix} 0 & J_\ell \\ J_{-\ell}^* & 0 \end{pmatrix}. \tag{4.42}$$

We are interested in the large frequency limit of the system that is described by this Hamiltonian. In this limit, the stroboscopic picture gives most of the relevant physics of the problem. We consider the Floquet-gauge invariant high frequency expansion of the Hamiltonian [61]

$$H_{\text{eff}} = H_0 + \frac{1}{\Omega} \begin{pmatrix} M_{\text{eff}} & 0 \\ 0 & -M_{\text{eff}} \end{pmatrix} + \mathcal{O}(1/\Omega^2), \quad (4.43)$$

where H_0 is the time-averaged Hamiltonian and the first-order effective mass is given by

$$M_{\text{eff}} = \sum_{\ell=1}^{\infty} \frac{1}{\ell} [|J_{\ell}|^2 - |J_{-\ell}|^2]. \quad (4.44)$$

We see from here that in the first order of the expansion, the drive behaves as if a mass term is introduced to the Hamiltonian. This effective mass can become non-zero when $J_{\ell} \neq J_{-\ell}$ for which the TRS needs to be broken.

However, we observe in Fig. (3)e-f that to have a gapped band structure of this system, the point-group C_3 symmetry also needs to be broken. To see why this should be the case, we look back at the Eq. (4.40), where for a C_3 -symmetric system one can write

$$J_{\ell}(\mathbf{k}) = J_{\ell}(\mathbf{k} = 0) \sum_{j=1}^3 e^{i\mathbf{k} \cdot \delta_j}. \quad (4.45)$$

This leaves us with an effective mass proportional to the $\left(\sum_{j=1}^3 e^{i\mathbf{k} \cdot \delta_j} \right)^2$ which is zero and has also a zero first derivative at the Dirac point. Note that this asymmetry between harmonics of the hopping parameter along different directions is present in the system where a time-periodic rotating gauge field renormalizes the hoppings via Peierls substitution [88].

Now that we found a way to open up a gap in the Floquet band structure, we still need to investigate if this gap is topological or trivial. To do so, we now take a look at the band structure of a finite system and look for signatures of topological edge modes in their band structure. One important requirement for this gap to be topological is that the mass has different signs on the two inequivalent Dirac points. Let us consider the previous case where we break the C_3 symmetry by introducing an asymmetric set of hoppings which satisfy $\frac{J_{\ell,1}}{r_{\ell,1}} = \frac{J_{\ell,2}}{r_{\ell,2}} = \frac{J_{\ell,3}}{r_{\ell,3}} = \kappa_{\ell}$. Now If we take a look back at the effective mass

term in our model, we have

$$M_{\text{eff}}(K) = \sum_{\ell=1}^{\infty} \frac{1}{\ell} [|\kappa_{\ell}|^2 A_{\ell}(K) - |\kappa_{-\ell}|^2 A_{-\ell}(K)],$$

$$M_{\text{eff}}(-K) = \sum_{\ell=1}^{\infty} \frac{1}{\ell} [|\kappa_{\ell}|^2 B_{\ell}(K) - |\kappa_{-\ell}|^2 B_{-\ell}(K)],$$

where

$$A_{\ell}(\mathbf{k}) = B_{\ell}(-\mathbf{k}) = \left| \sum_j r_{\ell,j} e^{i\mathbf{k} \cdot \delta_j} \right|^2. \quad (4.46)$$

Now as we see from here, if we only break the C_3 symmetry by a set of real directional hopping scales $r_{\ell,j}$, this will lead to $M_{\text{eff}}(K) = M_{\text{eff}}(-K)$, for which the gap in the band structure will be trivial. For a simplified case where the r factors are independent from the harmonic ℓ , it follows that

$$M_{\text{eff}}(K) = \sum_{\ell=1}^{\infty} \frac{1}{\ell} [|\kappa_{\ell}|^2 - |\kappa_{-\ell}|^2] A(K) \quad (4.47)$$

$$M_{\text{eff}}(-K) = \sum_{\ell=1}^{\infty} \frac{1}{\ell} [|\kappa_{\ell}|^2 - |\kappa_{-\ell}|^2] B(K). \quad (4.48)$$

For general complex r -factors the effective masses can become different.

Chapter 5.

Edge modes in rotating Rayleigh-Bénard systems



Pattern forming systems are a hallmark of studying non-equilibrium physics. A system that is driven out of equilibrium and is starting from a thermally fluctuating state finally reaches a state with clearly distinguishable patterns on a mesoscopic or macroscopic scale. The patterns can be stationary or time-dependent. This time dependence can range from coherent periodic behaviors or traveling waves to chaotic motions.

Here, we consider a well-studied example of these out-of-equilibrium systems that is called the Rayleigh-Bénard convection [119]. An experimental setup for this phenomenon is a cylindrical cell filled with a fluid that is exposed to two heat baths with different temperatures, the below plate being the hottest one, see Fig. 5.1(a). The buoyancy force resulting from this temperature difference leads to a heavier fluid near the top plate, which then together with the gravity force induce flows in the fluid. If temperature and gravity overcome the viscous forces of the fluid, convective flows start to emerge. This competition between drive and viscous forces is expressed quantitatively by the Rayleigh number

$$\text{Ra} = \frac{\alpha g d^3 \Delta T}{\nu \kappa}, \quad (5.1)$$

where α is the thermal expansion coefficient, g is the gravitational acceleration, d is the vertical length scale, ν is the kinetic viscosity, and κ is the thermal diffusivity of the fluid. The critical value for this parameter indicates the point beyond which convection takes place. The qualitative description above can be modeled by a set of modes for such systems which are linearly unstable above

the convection threshold. These unstable modes grow out of the thermally fluctuating states. However, this growth will have to stop eventually, as the nonlinearities get involved and saturate the growth, steering the system towards its steady state.

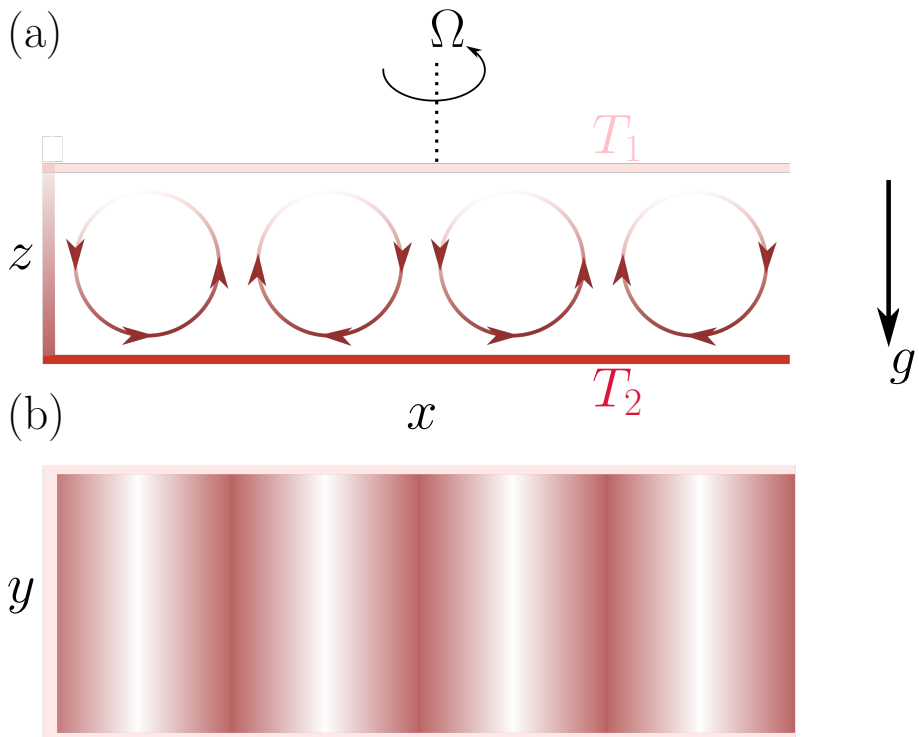


Figure 5.1: (a) A schematic picture of the Rayleigh-Bénard convection cell from the side view. The temperature field of the flow as well as that for the top and bottom plates is depicted by the intensity of the red color ($T_2 > T_1$). Above a critical point, the rolls start to develop and lead to the heat convection. A rotating Rayleigh-Bénard can be achieved by an angular velocity Ω . Panel (b) is a snapshot of this system from the top and shows a stripe pattern.

An important aspect of the description above is a competition between the modes themselves: the modes with maximum growth rates grow faster and thus eventually dominate the final steady state. At the onset of the instability transition, there is a finite number of most unstable modes of the system. These modes induce a slower length- and time scale into the system through their wavelength and frequency.

These slow characteristic length- (and time- for the case of oscillatory steady states) scales make the steady states periodic in space (and time). This explains the important observation of the system's self-organization towards patterns of hydrodynamic instabilities in the Rayleigh-Bénard experiments. There is a variety of shapes and types patterns that can appear in the Rayleigh-Bénard system [106]. The simplest of such patterns are in the shape of stripes (or rolls), as depicted in Fig. 5.1. Each roll is created as a result of the balance between the buoyancy forces and the dissipation due to viscosity and temperature diffusion between cold and hot flows. The separation of the rolls is determined by the characteristic length scale of the most unstable mode of the system. Also, depending on the frequency, this steady state pattern can be stationary or oscillatory in time.

Rotating Rayleigh-Bénard experiments are considered as simplified models for internally rotating convection systems, with examples in geophysical and astrophysical systems [105]. In a rotating Rayleigh-Bénard cell, the so-called wall modes, which are localized modes close to the vertical boundaries, precess in forms of unidirectionally moving traveling waves [142, 146, 179]. The observation of this unidirectional traveling edge states, along with similar observations in other pattern forming systems [58], suggests a possible relation between these modes and the topologically protected chiral edge modes in topological insulators. Inspired by the observation of topological modes in other hydrodynamics systems with Coriolis force [20, 38] or with chiral active constituents [19, 35], we became interested in studying such a possible explanation for the traveling wall modes in the rotating Rayleigh-Bénard experiments. For example, in a rotating Rayleigh-Bénard cell with a rotation rate Ω , the Coriolis force $\rho\Omega \times \mathbf{v}$ also breaks the chiral symmetry between right and left moving flows along the azimuthal direction [140, 142]. This chapter is a summary of this ongoing study that has been done in last two years.

Recently, Favier and Knobloch obtained a strong evidence of the robustness of the traveling wall modes by showing their immunity from extreme boundary deformations through full numerical simulations [4]. These flow patterns of wall modes seem to exist for a wide range of Rayleigh numbers beyond the onset of the convection transition, i.e. ranging from a stable to chaotic bulk [9, 11]. However, a theoretical explanation is yet lacking for these observations. In this chapter, we report our progress in formulating a theoretical framework for such a theoretical investigation.

We use a generalized Swift-Hohenberg equation to effectively describe the behavior of the rotating Rayleigh-Bénard cell [106, 174]. Using these equations we reproduce a variety of phenomena, such as pattern shapes. Furthermore, we linearize a one-dimensional Swift-Hohenberg model around its steady state and use periodic boundary conditions to extract its band structure. Furthermore, by calculating the Zak phase of these bands we find signs of non-trivial topology in this band structure and relate this to an up-down symmetry breaking of the model. To describe the topology of the wall modes in a rotating Rayleigh-Bénard experiment, one needs to consider a two-dimensional model, such as the generalized Swift-Hohenberg model. We numerically verify that this model leads to wall modes and traveling states, as well as their robustness to rough boundary deformations.

An important distinction of the Rayleigh-Bénard system with the other topological hydrodynamic examples above is the dissipative and the nonlinear aspects that are needed for pattern formation. With recent formulation of nonlinear Zak phases and their relation to topological states in nonlinear systems [10], the future focus of this project will be in generalizing our results to describe the topology of the full nonlinear models of the rotating Rayleigh-Bénard experiments. Also, the dissipative aspect introduces non-Hermiticity in the dynamics of this model [8], for which one needs to consider the topology of the non-Hermitian systems [1, 2, 31, 32].

5.1 Model equations

We consider a generalized Swift-Hohenberg equation [106],

$$\begin{aligned} \partial_t u = & ru - (1 + \nabla^2)^2 u + hu^2 - g_1 u^3 \\ & + g_2 \text{rot} \left([\nabla u]^2 \nabla u \right) + g_3 \text{div} \left([\nabla u]^2 \nabla u \right), \end{aligned} \quad (5.2)$$

where u represents the physical field such as velocity or temperature, and r is proportional to the reduced Rayleigh number

$$\epsilon = \text{Ra}/\text{Ra}_c - 1, \quad (5.3)$$

where Ra is the Rayleigh number and Ra_c is its critical value corresponding to the transition to convection transition. When $h = g_2 = g_3 = 0$, this equation is called the Swift-Hohenberg equation [174], which despite its simplicity (compared to full Navier-Stokes description of these systems) recreates some of the complex phenomena associated with the Rayleigh-Bénard experiment [140, 143, 162]. We now discuss the additional terms in the generalized model above.

5.1.1 Symmetries of the Rayleigh-Bénard system

The Swift-Hohenberg model has inversion symmetry that is between up and down flows, i.e. under $u \rightarrow -u$. This symmetry is violated once, for example, the fluid properties are temperature dependent, and thus the coefficients of the model change in the vertical direction as the higher flows are colder [184]. This is called the non-Boussinesq regimes [180] and can be mimicked in the model equation by adding a quadratic term which now breaks the up-down symmetry.

Apart from hexagonal patterns [145, 154, 181], symmetry breaking can bring new effects in the types of modes that can exist in a system. Let us focus for now on a quasi-1d model by considering stripe patterns in a Rayleigh-Bénard cell. A cross-sectional view of this flow pattern is shown in Fig. 5.2. We explained above that near the threshold one can consider a separation of scales by looking at the amplitude of slowly varying modes. Therefore, this picture can be qualitatively thought as amplitudes of a wavefunction that are located on the center of each roll and thus map this system into a lattice model. In a very qualitative way, let us consider that each roll interacts with a neighboring roll by passing alongside it [♣]. A non-Boussinesq regime can then be translated into a different coupling between the neighboring rolls that go upward and the one between downward flows. Thus, in this naive picture one can see that this system might be mapped to a SSH chain [172].

Mapping to a SSH chain might help with the existence of wall modes in Rayleigh-Bénard systems. However, we also tend to explain the traveling wall modes when such systems start to rotate. Therefore, we consider the rotational symmetry breaking of the Rayleigh-Bénard system with the introduction of rotation to the convection cell. This is also called a chiral or azimuthal symmetry in the literature [140, 142] and is the system's symmetry under flipping the horizontal velocities of the fluid. The term chiral symmetry breaking here is used differently from the chiral symmetry that corresponds to the sublattice symmetry in a SSH chain, e.g. in the chapter 2. Here, this symmetry can be understood from the observation of unidirectionally moving wall modes in the rotating Rayleigh-Bénard system. That is a reminder of the presence of chiral edge modes in the quantum Hall effect, and was our key motivation to try to understand the possible connections between the two systems. In a rotating cell the Coriolis force breaks this symmetry between right moving and left moving modes. In Eq. 5.2, the rotation term is the consequence of

[♣]We will try to quantify this approach later in this chapter.

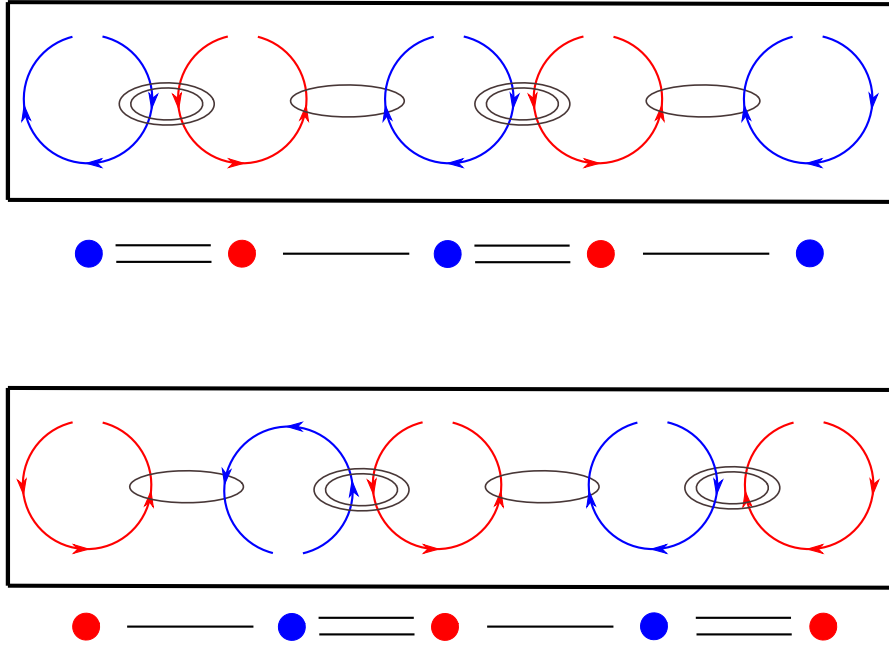


Figure 5.2: A qualitative map between a 1d Rayleigh-Bénard pattern forming system in the non-Boussinesq regime and the SSH chain. Putting a boundary to the system can break the translation symmetry of the effective lattice picture. This lack of the translation symmetry is a crucial factor in finding a topological edge mode in a SSH chain.

such force in the system and g_2 is proportional to the rotation rate Ω . The symmetry breaking of the Coriolis force is also present in the emergence of topological modes in ocean waves [38]. Topological modes are also found in fluids which break this symmetry through chiral constituents [19, 35, 58].

The last term in Eq. 5.2 is a potential term that is of the same order as the rotation term and becomes relevant in some regimes [158]. In our attempt to understand a minimal model to describe a rotating Rayleigh-Bénard cell, we drop this last term in our simulations by setting $g_3 = 0$.

5.1.2 Simulations of the generalized Swift-Hohenberg equations

We simulate generalized Swift-Hohenberg model, Eq. 5.2 using Dedalus, a package for solving partial differential equations based on spectral methods [3]. The convective domain is separated from a non-convective one via a change in the value of r . We perform these simulations for both quasi-1d and circular geometries of the convective domain. In our simulations, we observe the regimes of the system where the pattern is moving unidirectionally along the edge, while the bulk patterns are stationary up to local vibrations and not moving in a specific direction, see Fig. 5.3, where the bottom insets in panels (b)-(d) depicts a tracking of the hexagons. We observe this behavior for both stripe and hexagonal patterns. Here, we only focus on the regime of hexagonal patterns in order to avoid complicated behavior of the partially moving stripes in terms of defect creation and annihilation.

Furthermore, in our simulations we observe that the patterns are robust against boundary deformations. The hexagons at the domain wall act as unidirectionally moving particles without being backscattered from the obstacle at the boundary. These results reproduce the results of Ref. [4] using the generalized Swift-Hohenberg model.

5.2 Linear dispersion relation

Let us consider a general pattern forming system that is described by a nonlinear deterministic dynamics

$$\partial_t \psi = \mathcal{N}[\psi], \quad (5.4)$$

where \mathcal{N} is in general a nonlinear operator. Let us now constraint the systems to have a steady state that is obtained by $\mathcal{N}(\psi_{ss}) = 0$ for spatial patterns[♣]. For any perturbation around this steady state we have

$$\partial_t \psi = \mathcal{L}(\psi - \psi_{ss}) + \text{nonlinear terms}, \quad (5.5)$$

where

$$\mathcal{L} = \left. \frac{\partial \mathcal{N}}{\partial \psi} \right|_{\psi_{ss}} \quad (5.6)$$

[♣]For an instability pattern, one can generalize this definition to non-stationary steady states by requiring a frequency term in the right-hand side.

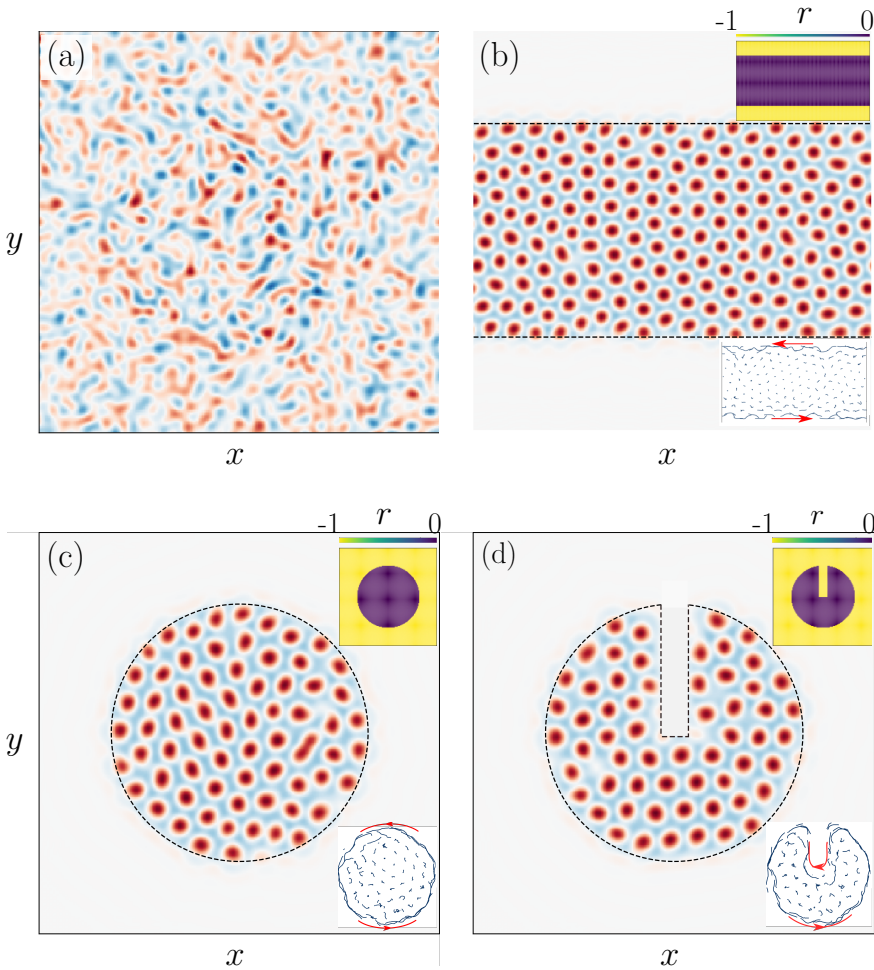


Figure 5.3: Simulation of the Rayleigh-Bénard system using Swift-Hohenberg model, Eq. 5.2. (a) The initial state is a thermal fluid. Hexagonal patterns appear in a quasi-1D (b) or a circular (cylindrical) setup. The top inset shows the r field that is used in the simulations to build a domain wall between ordered and non-convective ($r < 0$) states. The bottom inset shows a track of the hexagons in these simulations. The red arrows in these insets show the pattern movement direction at the walls. As can be seen in (b)-(c) the hexagons close to the domain wall move along the wall, while the ones in bulk vibrate. (d) Robustness of the wall modes in a rotating Rayleigh-Bénard systems with respect to boundary deformations. For these simulations we used $h = 1$, $g_1 = 1$, $g_2 = 0.1$, $g_3 = 0$, $r_{\text{inside}} = 0.3$, and $r_{\text{inside}} = -1$.

is the linearized operator that describes the dynamics of the system around its steady pattern. Here, we extract this dispersion relation by directly applying a Fourier transformation to the linear operator \mathcal{L} .

5.2.1 Fourier response and edge modes in 1d Swift-Hohenberg model

With a qualitative approach we reasoned that the breaking of the up-down symmetry in the 1d Swift-Hohenberg model in the non-Boussinesq regime, described by

$$\partial_t u = (r - 1)u - 2\partial_x^2 u - \partial_x^4 u - g_1 u^3 + hu^2 \quad (5.7)$$

can be similar to the chiral symmetry breaking in an SSH chain.

Here we quantitatively test this idea using the linear stability analysis method that is described before in Eq. 5.5. We look at the spectrum of the excitations around the steady state of the model, given it exists. To do so, we first linearize the Swift-Hohenberg equation around its steady state

$$\partial_t \delta u = (r - 1)\delta u - 2\partial_x^2 \delta u - \partial_x^4 \delta u - 3g_1 u_{ss}^2(x)\delta u + 2hu_{ss}(x), \quad (5.8)$$

where $\delta u(t, x) = u(t, x) - u_{ss}(x)$ is the perturbation around the steady state. Now we move to the Bloch space by writing $\delta u(x) = e^{-ikx}v(x)$, where $v(x + 2\pi) = v(x)$. The equation of motion for v reads $\partial_t v(t) = \mathcal{L}(k)v$, where $\mathcal{L}(k)$ is a differential operator acting on periodic functions. The real and imaginary values of the spectrum of this operator give the growth rate and the frequency of the excitations around the steady state. In Fig. 5.4 we show the growth rates for some values of r , g , and h . The excitations are non-oscillatory in this model, i.e. all frequencies are zero and the patterns are stationary.

We further examine the topological nature of these excitations by computing the Zak phase which is the integral of the Berry connection over the first BZ, and is determined for a single band i as [149]

$$\gamma_i = \int_{1^{st} \text{ BZ}} A_i. \quad (5.9)$$

Interestingly, we observe that when $h \neq 0$ gaps start to open in the band structure of $\mathcal{L}(k)$, as shown in Fig. 5.4. Alos, the Zak phases for the gapped bands are quantized and in some cases are $\pm\pi$, which is an indication of the topological non-equivalence of these bands with the ones with $\gamma = 0$.

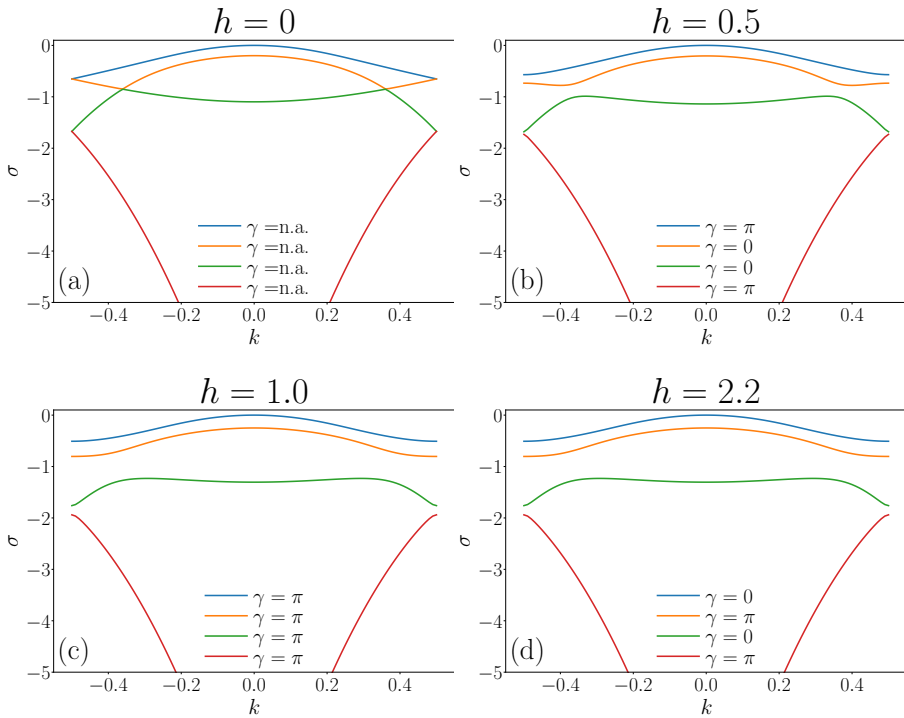


Figure 5.4: Growth rates, σ , of the modes in the linear stability analysis of the Swift-Hohenberg model around its steady state for various values of the up-down symmetry breaking parameter h . The horizontal axis shows the modes wavenumbers throughout the first Brillouin Zone. Legend shows the calculated Zak phase for each of the bands. We observe that the Zak phase is quantized for $h \neq 0$. For $h = 0$, the Zak phase is undefined as the band structure is not gapped.

We further build a domain wall in this system to examine the effect of this topological non-equivalence and check whether it leads to any domain-bound mode, as in the Jackiw-Rebbi model [163, 175]. In figure 5.5 we show the results of this numerical investigation for a choice of parameters $r = 0.1$, $g_1 = 2$, and the effective wall is between regions with $h = 1.2$ and $h = 2.0$. In panel (a), we show the projected growth rate bands for the two systems at different sides of the domain wall as well as the calculated Zak phases of each of the bands. In each shared gap (some of them can be very small) we indicate the observation of a domain-bound mode by \boxtimes , and use \times otherwise. Fig. 5.5(b) shows an the edge mode that corresponds to the non-trivial gap between the two sides of the domain wall.

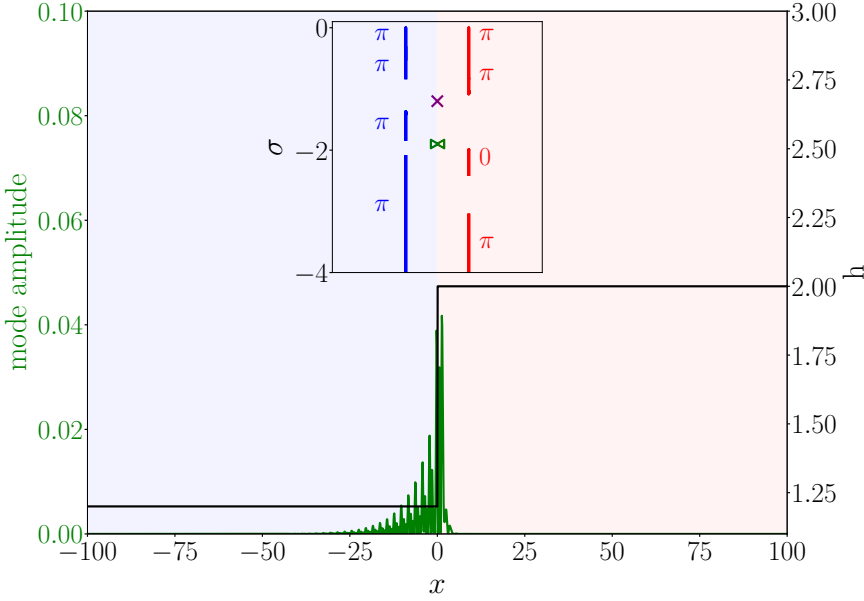


Figure 5.5: Search for domain-bound modes in the Swift-Hohenberg model with domain wall in the reflection-symmetry breaking parameter h . Inset shows a projection of the band structure for the linearized Swift-Hohenberg model for two regions. We search for the presence of the domain-bound modes induced by the domain wall between the two systems, and mark the presence of such modes in a shared gap with ∞ and the absence with x . The corresponding mode to the ∞ is localized at the boundary between the two domains and is exponentially decaying in intensity away from the domain wall.

These observations, although promising, are not a complete proof of a map between this system and a Jackiw-Rebbi model [175]. First of all, we examine a bulk-boundary correspondence between the presence of non-trivial gaps and the existence of domain-wall modes via direct numerical calculations. A systematic proof of the bulk-boundary correspondence above will be subject of further investigations.

Furthermore, it is not clear if the observation above proves a connection to other domain-wall systems, e.g. Jackiw-Rebbi model. In the Jackiw-Rebbi model, as we also saw in the second chapter of this thesis, the modes that localize at the domain wall of the system are polarized. This polarization

depends on the specific system and can for example be a mode's spin or sublattice degree of freedom. The existence of such polarization for the domain-bound modes in the Swift-Hohenberg equations that we derived above is yet to be understood.

Another concern is how to observe these edge modes, since all these edge modes are unstable with negative growth rates. One solution might be in the use of strong nonlinear terms at the boundary and larger perturbations around the steady state, similar to a pumping drive, such as in topological lasers [25, 27]. Having a negative growth rate from the stability analysis of the system around its steady state is inevitable by definition. Therefore, although getting to a topological band structure is plausible, we might still lose some of the physics of the problem by restricting ourselves to the linear regimes. In the rest of this chapter, we try to examine the topology of the system in nonlinear models. We then first start by a nonlinear regime of the problem very close to the threshold, where the separation of scales happens due to strong selection of most unstable modes in long-term dynamics. The formal description of this theory is through the amplitude expansion.

5.3 Nonlinear amplitude equations and system's discretization

At the threshold of the instability, the system starts to have a steady-state pattern. The state of the system around its steady state can be expressed as

$$\text{physical fields} = u^{\text{ss}}(t) + \sum_j A_j^{\text{ss}} e^{s_j t} \phi_j + \text{c.c.}, \quad (5.10)$$

where the perturbations around the steady state are expressed in the basis of the eigenmodes of the linearized operator, \mathcal{L} with the corresponding eigenvalues $s_j = \sigma_j + i\omega_j$, where σ is the growth rate and ω is the frequency of each mode. Of all the modes in this expansion, the ones with the maximum growth rate contribute to the long-term dynamics of the system: these modes grow in amplitude to trigger the nonlinearities in the system.

Very close to the threshold, the modes with positive growth rates have a wavenumber very close to the one from the most unstable mode(s) at the onset. The state of the system is thus effectively described by this subset of modes. One can describe this system using the following perturbatively expansion [140]:

$$u_{\text{p}} = \epsilon^{1/2} u_0 + \epsilon^{3/4} u_1 + \epsilon u_2 + \dots, \quad (5.11)$$

where ϵ is the distance from the threshold, and each order of the expansion can be written as

$$u_i(x, y, z, t) = e^{i\mathbf{k}\cdot\mathbf{r}} A_i(X, Y, T)v(x, y, z, t) + c.c., \quad |\mathbf{k}| = q_c, \quad (5.12)$$

where we separated the dynamics along the z direction from the amplitude A_i . Moreover, the spatial dynamics in the direction perpendicular to the top-bottom surfaces of the cylinder is also separated for patterns with characteristic wavenumber q_c . The amplitudes A_i are slowly varying envelopes that can mimic a periodic structure of stripes. That is close to a Bloch tight-binding description of a continuum wavefunction of a lattice in quantum mechanics. This approximation can lead to a discretized model of this complex system close to the threshold of pattern formation. In the situations where two or more modes constitute to a system's steady state, this effective discretized model might be helpful in describing the interaction of these modes. Examples of such systems are observed in Rayleigh-Bénard cells where square or hexagonal patterns become linearly more stable than the stripe instabilities [156, 164, 181].

The slow parameters X, Y, T are scaled spatial and temporal variables which should be deduced from the dynamics of the physical fields. They are such that $|\nabla_{\mathbf{r}}A| \ll |q_c A|$ and $|\partial_t A| \ll |\omega_c A|$, where $\omega_c = \omega(q_c)$ is the frequency of the most unstable mode. One can then reduce the dynamical model into finding the dynamics of the slowly varying envelopes A_i . By using this steps, we derive the following amplitude equations for the generalized Swift-Hohenberg model given by Eq. 5.2 (details in the appendix):

$$\begin{aligned} \partial_T A_0 &= \left[1 + 4 \left(\partial_X - \frac{i}{2} \partial_Y^2 \right)^2 \right] A_0 - \left(3g_1 - \frac{10}{3} h^2 + 3g_3 \right) A_0 |A_0|^2 \quad (5.13) \\ \partial_T A_1 &= \left[1 + 4 \left(\partial_X - \frac{i}{2} \partial_Y^2 \right)^2 \right] A_1 - 3g_1 [A_0^2 A_1^* + 2|A_0|^2 A_1] \\ &\quad - 4ig_2 [A_0 \partial_Y |A_0|^2] + \frac{4}{3} h^2 [A_0^2 A_1^* + 5|A_0|^2 A_1] \\ &\quad - 3g_3 [A_0^2 A_1^* + 2|A_0|^2 A_1]. \quad (5.14) \end{aligned}$$

with slow variables

$$X = \epsilon^{1/2} x, \quad (5.15a)$$

$$Y = \epsilon^{1/4} y, \quad (5.15b)$$

$$T = \epsilon t. \quad (5.15c)$$

The Eqs. 5.13-5.14 are in agreement with the the results obtained from the full Boussinesq equations [117]. There are some differences, including a second slower time scale $T' = \epsilon^{5/4}T$ which we did not fully explore, but that might have to do with the fact that the dynamics of the modes along the edge are happening at a different time scale compared to the other directions.

Amplitude equations above give a simplified nonlinear description of the Rayleigh-Bénard system's dynamics using the assumption that close to the threshold the fast and slow scale dynamics become separated. In the following, we will try to use this simplified model towards a description of the topology of the Rayleigh-Bénard system.

5.4 Band structure and topology of nonlinear systems

So far, we observed that the in 1d, the linearization of the Swift-Hohenberg model around its steady state solution leads to a band structure with Zak phases equal to $\pm\pi$. One issue with this approach is that, by definition the perturbations of the system around its steady state are decaying. Therefore, even if there are topological edge modes in such spectrum, it will not lead to the presence of this mode in the pattern forming system, except for a temporal rapidly deteriorating mode.

Following along this lines, we then could conclude that it might be more relevant to look for the topological properties of the modes in the full nonlinear regime. We then would like to see if the patterns, as the steady states of the system, are themselves topological modes of the fully nonlinear models.

To search for these modes in the context of band topology, we need to consider a generalized version of at least two concepts from the standard Hamiltonian problems. First, we need to generalize the band structure for a fully nonlinear Schrodinger equation, i.e. by solving the eigenvalue problem $H[u]u = \epsilon u$ for a state-dependent Hamiltonian $H[u]$. We then would like to be able to repeat this for the Fourier components of this nonlinear Hamiltonian to obtain the energy spectrum in the Bloch space. Since H is state dependent, solving this equation in general can be very complicated. For example, a single plane-wave ansatz might be insufficient to diagonalize the Hamiltonian. Instead, we might want to generalize this to a more general space of functions using spectral methods.

There is however at least a family of such nonlinear Hamiltonians for which one can still use the Bloch Fourier transformation to find eigenstates of the system. That is, when the state-dependent terms are mere radial maps of the state u , such as $|u|^2u$, etc. Models of this sort describe various physical system including examples from interacting Bose-Einstein systems described by Gross-Pitaevskii equations [130], KdV equations, nonlinear electronics and optics systems [6]. These systems are known to harbor solitary waves [144].

The second generalizations we will need to consider is how to characterize the topology in such nonlinear band structures. In a recent preprint [10], it was shown that adding nonlinearity to the Schrodinger equation can have an effect on the topological properties of the band structure. Particularly, this paper shows that adding nonlinearity to a SSH chain [172] can push the bands that are continuously evolved from the linear model, to revive an effective chiral symmetry (or a sublattice symmetry), even in the presence of the terms which break this symmetry. This result is then supported by generalization of Zak phase for nonlinear models, and showing that the quantization of the sum of these new phases revives as the nonlinearity becomes stronger in this system. Nonetheless, the nonlinear Zak phase continuously convert to the regular one in the linear models. Another interesting result in this paper was the presence of *in-gap solitons*, or the localized bulk states. The authors relate the presence of such modes to the emergent effective edges in the bulk due to the nonlinear terms and larger mode amplitudes. Considering these results, one would wonder whether the non-trivial Zak phases in the linearized Swift-Hohenberg model that we measured in the previous section is a hint to more general topological phases in the full nonlinear regime.

The non-linear band topology in the Ref. [10] above is examined for effective 1d models, whereas a rotating Rayleigh-Bénard systems is described by a two-dimensional model. An amplitude expansion for a two-dimensional model one can introduce a coupling term $G(\theta)$ between the modes with different orientation of their wavevectors [178]. This coupling can also break a rotational symmetry in the system, for example when it rotates ($G(\theta) \neq G(-\theta)$) [106]. These symmetry breaking terms are present in other time-reversal broken topological insulators [100]. A more complete treatment of the rotating Rayleigh-Bénard systems in terms of topological properties of nonlinear systems will be subject of our future investigations.

5.5 Discussion and outlook

In this chapter, we discussed the results of an ongoing study on the topological phases in the rotating Rayleigh-Bénard system. Using numerical computations, we have observed topological Zak phases in the linearized band structure of the 1d Swift-Hohenberg model. An unknown fact about the model above is about the notion of polarization for these modes. As we have seen in the second chapter about the mechanical graphene, edge modes on Jackiw-Rebbi-type models are spin polarized (in that case sublattice polarized). The translation of this concept to a 1d Swift-Hohenberg model is still to be understood. Also, the bands of this linearized model are constructed by modes with negative growth rates. Hence, it is still not clear how these modes can have an effect on the non-transient dynamics of the system or can give rise to the topological edge modes, as suggested by recent numerical simulations [4]. Nonlinear drives at the boundary can have an effect on bringing the topological modes with negative linear growth rates into long-term dynamics of the Rayleigh-Bénard system.

Therefore, an explanation of the topological origin of the traveling states at the wall of the rotating Rayleigh-Bénard cell requires the generalization this result for the full non-linear equations. To do this, we first used a generalized Swift-Hohenberg model to reproduce the results of the Ref. [4] about the robustness of the wall modes in a rotating Rayleigh-Bénard system. A description of these wall modes will then probably require a generalization of the topological indices for a non-linear model. A first step will be to calculate the recently developed generalized Zak phase [10] for a 1d Swift-Hohenberg model, for which we already have a strong indication from the band topology of the linearized equations. We note that the topological indices for non-linear models are new concepts which we need to consider for the study of an out-of-equilibrium system.

Furthermore, A discretized model, as we described in §5.3, is useful in mapping the Rayleigh-Bénard system to a lattice model. This approach can be particularly useful for the 2d pattern forming systems. For example, It will be interesting to see how a three-coupled mode for hexagonal patterns are described with this theory, as for such patterns the amplitude description contains a chiral symmetry breaking term.

Also, a full description of such models will likely require non-Hermitian operators due to dissipation from the viscous forces. Looking forward, we will study a discretized model with the relevant symmetry-breaking terms. This model then will be both nonlinear and non-Hermitian. In future investigations, we will focus on the topological phases of the modes in such systems.

5.6 Appendix

5.6.1 Band structure of nonlinear Schrödinger/Gross-Pitaevskii equations

We discussed above that the generalization of the concept of band structure for the nonlinear Schrödinger can be far from straightforward. Especially, when the nonlinear terms are not radial, solving the eigenvalue problem will require a more general spectral method instead of Bloch waves. The nonlinear terms in the Swift-Hohenberg equation, even in the 1d version, are of this form. Thus, we will have to see how we should deal with the full diagonalization problem, when we decide to generalize this approach to this equation. Interestingly, when we linearize the model around the onset of the pattern formation system, i.e. for small values for the reduced Rayleigh number ϵ , it leads to a separation of scales in the form of amplitude equations, see Eqs. 5.13 and 5.14. When this separation happens, we no longer need to consider a mixture of Bloch modes in a spectral method in order to diagonalize the Hamiltonian. The amplitude equations are in form closer to Gross-Pitaevskii equations, or nonlinear Ginsburg-Landau equations. For example, it is shown that a complex Ginsburg-Landau equation can describe the one-way propagating mode in a rotating Rayleigh-Bénard cell [135].

Here, we derive the energy spectrum of the nonlinear Schrödinger equations that was considered in the nonlinear Landau-Zener tunnelling effect [126, 129]. Consider the following Hamiltonian of a two-level system:

$$H_{NLZ} \left[\begin{pmatrix} a \\ b \end{pmatrix} \right] = \frac{\gamma}{2} \sigma_z + \frac{v}{2} \sigma_x + \frac{c}{2} (|b|^2 - |a|^2) \sigma_z, \quad (5.16)$$

which modifies the Hamiltonian of a standard Landau-Zener model by adding a nonlinear term which is proportional to the population difference of the system. The time-dependent version of this problem is achieved by considering $\gamma(t) = \alpha t$. When α is small compared to the energy gap, the evolution of the

system is expected to follow an adiabatic path. However, it is shown in the Ref. [129] that when $c > v$ this model predicts a tunneling even in the adiabatic limit. This nonadiabatic behavior appears as a result of loop structures in the band structure of the model.

We now give the steps to calculate the band structure of this model. We start by writing down the Schrödinger equation

$$i\partial_t a = \frac{v}{2}b + \left[\frac{\gamma}{2} + \frac{c}{2} (|b|^2 - |a|^2) \right] a, \quad (5.17a)$$

$$i\partial_t b = \frac{v}{2}a - \left[\frac{\gamma}{2} + \frac{c}{2} (|b|^2 - |a|^2) \right] b. \quad (5.17b)$$

The total population of the two bands $|b|^2 + |a|^2$ is constant (it is easy to check with the equations above). It is then possible to write

$$\begin{pmatrix} a \\ b \end{pmatrix} = e^{i\varphi_1} \begin{pmatrix} \sin \frac{\varphi}{2} \\ e^{i\theta} \cos \frac{\varphi}{2} \end{pmatrix}. \quad (5.18)$$

We define the population difference variable $s = |b|^2 - |a|^2 = \cos \varphi$. In terms of these new parameters, the Schrodinger equations converts to

$$\begin{aligned} \frac{i}{2}\dot{\varphi} \cos \frac{\varphi}{2} - \dot{\varphi}_1 \sin \frac{\varphi}{2} &= \frac{v}{2}e^{i\theta} \cos \frac{\varphi}{2} + \left[\frac{\gamma}{2} + \frac{c}{2} \cos \varphi \right] \sin \frac{\varphi}{2}, \quad (5.19) \\ \frac{-i}{2}\dot{\varphi} \sin \frac{\varphi}{2} - (\dot{\theta} + \dot{\varphi}_1) \cos \frac{\varphi}{2} &= \frac{v}{2}e^{-i\theta} \sin \frac{\varphi}{2} - \left[\frac{\gamma}{2} + \frac{c}{2} \cos \varphi \right] \cos \frac{\varphi}{2}. \end{aligned} \quad (5.20)$$

The real and imaginary parts of these equations lead to

$$\dot{s} = -\frac{dH_{\text{cl,NLZ}}}{d\theta} = -v\sqrt{1-s^2} \sin \theta \quad (5.21a)$$

$$\dot{\theta} = \frac{dH_{\text{cl,NLZ}}}{ds} = \frac{\gamma + cs}{1+s} \quad (5.21b)$$

$$\dot{\varphi}_1 = -\left[\frac{\gamma}{2} + \frac{c}{2}s \right] - \frac{v\sqrt{1+s}}{2\sqrt{1-s}} e^{i\theta} \quad (5.21c)$$

The eigensystem of the nonlinear Hamiltonian H_{NLZ} translates into $\dot{s} = \dot{\theta} = 0$ and $\dot{\varphi}_1 = \varepsilon$. Thus, the eigenmodes of the nonlinear Hamiltonian will correspond to the fixed points of the classical Hamiltonian [126, 137]

$$H_{\text{cl,NLZ}} = \frac{c}{2}s^2 + \gamma s - v\sqrt{1-s^2} \cos \theta. \quad (5.22)$$

Therefore, the eigenmodes of the nonlinear Hamiltonian correspond to

$$\theta^* = 0, \pi; \quad cs^* + \gamma = \frac{\pm v}{\sqrt{1 - s^{*2}}}, \quad (5.23)$$

which leads to

$$f(s^*) = (1 - s^{*2})(s^* + \gamma/c)^2 = (vs^*/c)^2. \quad (5.24)$$

The function f is positive in the interval $[-1, 1]$ and takes one maximum (two local maxima) when $|\gamma/c| > 1$ ($|\gamma/c| > 1$). Following a standard process, we find that Eq. 5.24 has two solutions for $v/c > 1$ and four solutions when $v/c < 1$ and $|\gamma| < \gamma_c$ for a critical γ_c value. These extra solutions to the nonlinear equations lead to loop shapes in system's energy spectrum. As a result, an adiabatic change in the Hamiltonian can lead to a nonadiabatic change in the ground state of the system which is what the authors call nonlinear Landau-Zener (NLZ) tunnelling.

5.6.2 A nonlinear SSH chain

We now try to study these generalizations in the context of a nonlinear SSH chain, following the results in the Ref. [10]. By starting from discrete system and considering the Bloch wavefunctions $\Psi_{A/B,j} = \Phi_{A/B,j} e^{ikj}$, the authors arrive to the following model:

$$H(\Sigma) = (J_1 + J_2 \cos k)\sigma_x + J_2 \sin k\sigma_y + h(\Sigma)\sigma_z + \frac{g}{2}I_2, \quad (5.25)$$

where J_1 and J_2 are the hoppings in the chain, $h(\Sigma) = v + \frac{g}{2}[|\Phi_B|^2 - |\Phi_A|^2]$ contains the nonlinear term that is state dependent with g as nonlinearity strength, and v a chiral symmetry breaking term. Due to lack of the latter symmetry, in the usual case of the linear SSH the topological edge mode does not exist and the winding number of the Hamiltonian becomes ill defined. Interestingly, it is shown in Ref. [10] that in the presence of strong nonlinearity, the chiral symmetry effectively revives in the system's band structure and therefore it is possible to calculate a nonlinear Zak phase which is quantized.

Without going to further details, here we try to study the band structure for this system corresponding to the eigenvalue problem $H(\Sigma)\Phi = \varepsilon\Phi$, where $\Phi = \begin{pmatrix} \Phi_A \\ \Phi_B \end{pmatrix}$. First, it is easy to check that Eq. 5.25 leads to $|\Phi_A|^2 + |\Phi_B|^2 = 1$ (up to constants). We have

$$i\partial_t\Phi_A = v\Phi_A + \frac{g}{2}|\Phi_A|^2\Phi_A + (J_1 + J_2e^{-ik})\Phi_B, \quad (5.26a)$$

$$i\partial_t\Phi_B = -v\Phi_B + \frac{g}{2}|\Phi_B|^2\Phi_B + (J_1 + J_2e^{ik})\Phi_A. \quad (5.26b)$$

These equations are similar in structure to the NLZ problem, Eqs. 5.17. Using the same method as above we find

$$\dot{s} = -\frac{dH_{\text{cl,NSSH}}}{d\theta} = -2\sqrt{1-s^2} [J_1 \sin \theta + J_2 \sin(\theta - k)], \quad (5.27a)$$

$$\dot{\theta} = \frac{dH_{\text{cl,NSSH}}}{ds} = 2v - \frac{g}{2}s + \frac{2s}{\sqrt{1-s^2}} [J_1 \cos \theta + J_2 \cos(\theta - k)], \quad (5.27b)$$

$$\varepsilon_k = -\dot{\varphi}_1 = v + g\frac{1-s}{4} + \sqrt{\frac{1+s}{1-s}} [J_1 \cos \theta + J_2 \cos(\theta - k)], \quad (5.27c)$$

where $H_{\text{cl,NSSH}} = 2vs - \frac{g}{4}s^2 - 2\sqrt{1-s^2} [J_1 \cos \theta + J_2 \cos(\theta - k)]$. Here one needs to diagonalize the system for each wavenumber k in order to obtain a band structure. This calculation leads to the loop shapes in the band structure of the model in some regions of the BZ in the strong nonlinear regimes [10].

References

- [1] Yuto Ashida, Zongping Gong, and Masahito Ueda. *Non-Hermitian Physics*. 2020. arXiv: 2006.01837 (80).
- [2] Emil J. Bergholtz, Jan Carl Budich, and Flore K. Kunst. *Exceptional Topology of Non-Hermitian Systems*. 2020. arXiv: 1912.10048 (80).
- [3] Keaton J. Burns, Geoffrey M. Vasil, Jeffrey S. Oishi, Daniel Lecoanet, and Benjamin P. Brown. *Dedalus: A flexible framework for numerical simulations with spectral methods*. **Physical Review Research** 2 2, 023068, **2020** (83)
URL: <https://doi.org/10.1103/PhysRevResearch.2.023068>.
- [4] Benjamin Favier and Edgar Knobloch. *Robust wall states in rapidly rotating Rayleigh–Bénard convection*. **Journal of Fluid Mechanics** 895, R1, **2020** (79, 83, 92)
URL: <https://doi.org/10.1017/jfm.2020.310>.
- [5] Andrew J. Hess, Guilhem Poy, Jung-Shen B. Tai, Slobodan Žumer, and Ivan I. Smalyukh. *Control of Light by Topological Solitons in Soft Chiral Birefringent Media*. **Phys. Rev. X** 10, 031042, **2020** (33)
URL: <https://link.aps.org/doi/10.1103/PhysRevX.10.031042>.
- [6] F. Palmero, L.Q. English, J. Cuevas-Maraver, and P.G. Kevrekidis. *Nonlinear edge modes in a honeycomb electrical lattice near the Dirac points*. **Physics Letters A** 384 26, 126664, **2020** (91)
URL: <http://www.sciencedirect.com/science/article/pii/S0375960120305314>.
- [7] Guilhem Poy, Andrew J. Hess, Ivan I. Smalyukh, and Slobodan Žumer. *Chirality-Enhanced Periodic Self-Focusing of Light in Soft Birefringent Media*. **Phys. Rev. Lett.** 125, 077801, **2020** (33)
URL: <https://link.aps.org/doi/10.1103/PhysRevLett.125.077801>.
- [8] Suraj Shankar, Anton Souslov, Mark J. Bowick, M. Cristina Marchetti, and Vincenzo Vitelli. *Topological active matter*. 2020. arXiv: 2010.00364 (80).

- [9] Olga Shishkina. *Tenacious wall states in thermal convection in rapidly rotating containers*. **Journal of Fluid Mechanics** 898, F1, **2020** (79)
URL: <https://doi.org/10.1017/jfm.2020.420>.
- [10] Thomas Tuloup, Raditya Weda Bomantara, Ching Hua Lee, and Jiangbin Gong. *Nonlinearity induced topological physics in momentum space and real space*. 2020. arXiv: 2006.09753 (11, 80, 91, 92, 95, 96).
- [11] Xuan Zhang, Dennis P. M. van Gils, Susanne Horn, Marcel Wedi, Lukas Zwirner, Guenter Ahlers, Robert E. Ecke, Stephan Weiss, Eberhard Bodenschatz, and Olga Shishkina. *Boundary Zonal Flow in Rotating Turbulent Rayleigh-Bénard Convection*. **Phys. Rev. Lett.** 124, 084505, **2020** (79)
URL: <https://link.aps.org/doi/10.1103/PhysRevLett.124.084505>.
- [12] José Francisco Algorri, Dimitrios C. Zografopoulos, Virginia Urruchi, and José Manuel Sánchez-Pena. *Recent Advances in Adaptive Liquid Crystal Lenses*. **Crystals** 9 5, 460–500, **2019** (33)
URL: <https://doi.org/10.3390/cryst9050272>.
- [13] Eliahu Cohen, Hugo Larocque, Frédéric Bouchard, Farshad Nejad-sattari, Yuval Gefen, and Ebrahim Karimi. *Geometric phase from Aharonov-Bohm to Pancharatnam-Berry and beyond*. **Nature Reviews Physics**, 437–449, **2019** (56)
URL: <https://doi.org/10.1038/s42254-019-0071-1>.
- [14] Jonathan Guglielmon and Mikael C. Rechtsman. *Broadband Topological Slow Light through Higher Momentum-Space Winding*. **Phys. Rev. Lett.** 122, 153904, **2019** (55)
URL: <https://link.aps.org/doi/10.1103/PhysRevLett.122.153904>.
- [15] Guancong Ma, Meng Xiao, and C. T. Chan. *Topological phases in acoustic and mechanical systems*. **Nature Reviews Physics** 1 4, 281–294, **2019** (55)
URL: <https://doi.org/10.1038/s42254-019-0030-x>.
- [16] Mohammad-Ali Miri and Andrea Alù. *Exceptional points in optics and photonics*. **Science** 363 6422, **2019** (66)
URL: <https://science.sciencemag.org/content/363/6422/eaar7709>.
- [17] Tomoki Ozawa, Hannah M. Price, Alberto Amo, Nathan Goldman, Mohammad Hafezi, Ling Lu, Mikael C. Rechtsman, David Schuster, Jonathan Simon, Oded Zilberberg, and Iacopo Carusotto. *Topological photonics*. **Rev. Mod. Phys.** 91, 015006, **2019** (32, 55, 56, 61)
URL: <https://link.aps.org/doi/10.1103/RevModPhys.91.015006>.

- [18] Marie S. Rider, Samuel J. Palmer, Simon R. Pocock, Xiaofei Xiao, Paloma Arroyo Huidobro, and Vincenzo Giannini. *A perspective on topological nanophotonics: Current status and future challenges*. **Journal of Applied Physics** 125 12, 120901, **2019** (55, 56)
URL: <https://doi.org/10.1063/1.5086433>.
- [19] Anton Souslov, Kinjal Dasbiswas, Michel Fruchart, Suriyanarayanan Vaikuntanathan, and Vincenzo Vitelli. *Topological Waves in Fluids with Odd Viscosity*. **Phys. Rev. Lett.** 122, 128001, **2019** (55, 79, 82)
URL: <https://link.aps.org/doi/10.1103/PhysRevLett.122.128001>.
- [20] C. Tauber, P. Delplace, and A. Venaille. *A bulk-interface correspondence for equatorial waves*. **Journal of Fluid Mechanics** 868, R2, **2019** (55, 79)
URL: <https://doi.org/10.1017/jfm.2019.233>.
- [21] Xinhua Wen, Chunyin Qiu, Yajuan Qi, Liping Ye, Manzhu Ke, Fan Zhang, and Zhengyou Liu. *Acoustic Landau quantization and quantum-Hall-like edge states*. **Nature Physics** 15 4, 352–356, **2019** (32)
URL: <https://doi.org/10.1038/s41567-019-0446-3>.
- [22] Hao Yu, Miao Jiang, Yubing Guo, Taras Turiv, Wu Lu, Vishva Ray, Oleg D. Lavrentovich, and Qi-Huo Wei. *Plasmonic Metasurfaces with High UV-Vis Transmittance for Photopatterning of Designer Molecular Orientations*. **Advanced Optical Materials** 7 11, 1900117, **2019** (33, 67)
URL: <https://onlinelibrary.wiley.com/doi/abs/10.1002/adom.201900117>.
- [23] Hao Yu, Ziyuan Zhou, Yongle Qi, Xinfang Zhang, and Qi-Huo Wei. *Pancharatnam-Berry optical lenses*. **J. Opt. Soc. Am. B** 36 5, D107–D111, **2019** (33)
URL: <http://josab.osa.org/abstract.cfm?URI=josab-36-5-D107>.
- [24] Ziyuan Zhou, Yubing Guo, Hao Yu, Miao Jiang, Taras Turiv, Irakli Chaganava, Oleg D. Lavrentovich, and Qi-Huo Wei. “Liquid crystal Pancharatnam-Berry optical elements.” In: *Liquid Crystals XXIII*. Ed. by Iam Choon Khoo. Vol. 11092. International Society for Optics and Photonics. SPIE, 2019, 31–38. URL: <https://doi.org/10.1117/12.2528086> (33).
- [25] Miguel A. Bandres, Steffen Wittek, Gal Harari, Midya Parto, Jinhan Ren, Mordechai Segev, Demetrios N. Christodoulides, and Mercedeh Khajavikhan. *Topological insulator laser: Experiments*. **Science** 359 6381, **2018** (55, 88)
URL: <https://science.sciencemag.org/content/359/6381/eaar4005>.

- [26] Michel Fruchart, Seung-Yeol Jeon, Kahyun Hur, Vadim Cheianov, Ulrich Wiesner, and Vincenzo Vitelli. *Soft self-assembly of Weyl materials for light and sound*. **Proceedings of the National Academy of Sciences** 115 16, E3655–E3664, **2018** (55)
URL: <https://doi.org/10.1073/pnas.1720828115>.
- [27] Gal Harari, Miguel A. Bandres, Yaakov Lumer, Mikael C. Rechtsman, Y. D. Chong, Mercedeh Khajavikhan, Demetrios N. Christodoulides, and Mordechai Segev. *Topological insulator laser: Theory*. **Science** 359 6381, **2018** (55, 88)
URL: <https://science.sciencemag.org/content/359/6381/eaar4003>.
- [28] Miao Jiang, Hao Yu, Xiayu Feng, Yubing Guo, Irakli Chaganava, Taras Turiv, Oleg D. Lavrentovich, and Qi-Huo Wei. *Liquid Crystal Pancharatnam-Berry Micro-Optical Elements for Laser Beam Shaping*. **Advanced Optical Materials** 6 23, 1800961, **2018** (33, 67)
URL: <https://onlinelibrary.wiley.com/doi/abs/10.1002/adom.201800961>.
- [29] Ching Hua Lee, Stefan Imhof, Christian Berger, Florian Bayer, Johannes Brehm, Laurens W. Molenkamp, Tobias Kiessling, and Ronny Thomale. *Topoelectrical Circuits*. **Communications Physics** 1 1, 39, **2018** (55)
URL: <https://doi.org/10.1038/s42005-018-0035-2>.
- [30] Kathryn H. Matlack, Marc Serra-Garcia, Antonio Palermo, Sebastian D. Huber, and Chiara Daraio. *Designing perturbative metamaterials from discrete models*. **Nature Materials** 17 4, 323–328, **2018** (13)
URL: <https://doi.org/10.1038/s41563-017-0003-3>.
- [31] Huitao Shen, Bo Zhen, and Liang Fu. *Topological Band Theory for Non-Hermitian Hamiltonians*. **Phys. Rev. Lett.** 120, 146402, **2018** (80)
URL: <https://link.aps.org/doi/10.1103/PhysRevLett.120.146402>.
- [32] Shunyu Yao and Zhong Wang. *Edge States and Topological Invariants of Non-Hermitian Systems*. **Phys. Rev. Lett.** 121, 086803, **2018** (80)
URL: <https://link.aps.org/doi/10.1103/PhysRevLett.121.086803>.
- [33] Xiujian Zhang, Meng Xiao, Ying Cheng, Ming-Hui Lu, and Johan Christensen. *Topological sound*. **Communications Physics** 1 1, **2018** (55)
URL: <https://doi.org/10.1038/s42005-018-0094-4>.
- [34] Mark J. Ablowitz and Justin T. Cole. *Tight-binding methods for general longitudinally driven photonic lattices: Edge states and solitons*. **Phys. Rev. A** 96, 043868, **2017** (58)
URL: <https://link.aps.org/doi/10.1103/PhysRevA.96.043868>.

- [35] Debarghya Banerjee, Anton Souslov, Alexander G. Abanov, and Vincenzo Vitelli. *Odd viscosity in chiral active fluids*. **Nature Communications** 8 1, 1573, **2017** (79, 82)
URL: <https://doi.org/10.1038/s41467-017-01378-7>.
- [36] M. Bellec, C. Michel, H. Zhang, S. Tzortzakis, and P. Delplace. *Non-diffracting states in one-dimensional Floquet photonic topological insulators*. **EPL (Europhysics Letters)** 119 1, 14003, **2017** (56, 58)
URL: <https://doi.org/10.1209/0295-5075/119/14003>.
- [37] Christian Brendel, Vittorio Peano, Oskar J. Painter, and Florian Marquardt. *Pseudomagnetic fields for sound at the nanoscale*. **Proceedings of the National Academy of Sciences**, 201615503, **2017** (32)
URL: <https://www.pnas.org/content/early/2017/04/10/1615503114>.
- [38] Pierre Delplace, J. B. Marston, and Antoine Venaille. *Topological origin of equatorial waves*. **Science** 358 6366, 1075–1077, **2017** (55, 79, 82)
URL: <https://science.sciencemag.org/content/358/6366/1075>.
- [39] Liang Feng, Ramy El-Ganainy, and Li Ge. *Non-Hermitian photonics based on parity-time symmetry*. **Nature Photonics** 11 12, 752–762, **2017** (66)
URL: <https://doi.org/10.1038/s41566-017-0031-1>.
- [40] Chandroth P. Jisha, Alessandro Alberucci, Lorenzo Marrucci, and Gaetano Assanto. *Interplay between diffraction and the Pancharatnam-Berry phase in inhomogeneously twisted anisotropic media*. **Phys. Rev. A** 95, 023823, **2017** (33, 40, 56)
URL: <https://doi.org/10.1103/PhysRevA.95.023823>.
- [41] Lukas J. Maczewsky, Julia M. Zeuner, Stefan Nolte, and Alexander Szameit. *Observation of photonic anomalous Floquet topological insulators*. **Nature Communications** 8 1, 13756, **2017** (56)
URL: <https://doi.org/10.1038/ncomms13756>.
- [42] Arvind Murugan and Suriyanarayanan Vaikuntanathan. *Topologically protected modes in non-equilibrium stochastic systems*. **Nature Communications** 8 1, 13756, **2017** (55)
URL: <https://doi.org/10.1038/ncomms13881>.
- [43] Jiho Noh, Sheng Huang, Daniel Leykam, Y. D. Chong, Kevin P. Chen, and Mikael C. Rechtsman. *Experimental observation of optical Weyl points and Fermi arc-like surface states*. **Nature Physics** 13 6, 611–617, **2017** (67)
URL: <https://doi.org/10.1038/nphys4072>.

- [44] D. Zeb Rocklin, Shangnan Zhou, Kai Sun, and Xiaoming Mao. *Transformable topological mechanical metamaterials*. **Nature Communications** 8 1, 14201, **2017** (32)
URL: <https://doi.org/10.1038/ncomms14201>.
- [45] J. J. Sakurai and Jim Napolitano. *Modern Quantum Mechanics*. **2017** (3, 37)
URL: <https://doi.org/10.1017/9781108499996>.
- [46] Anton Souslov, Benjamin C. van Zuiden, Denis Bartolo, and Vincenzo Vitelli. *Topological sound in active-liquid metamaterials*. **Nature Physics** 13 11, 1091–1094, **2017** (55)
URL: <https://doi.org/10.1038/nphys4193>.
- [47] Alessandro Alberucci, Chandroth P. Jisha, Sergei Slussarenko, Bruno Piccirillo, Enrico Santamato, Lorenzo Marrucci, and Gaetano Assanto. “A new waveguiding mechanism based upon geometric phase.” In: *Frontiers in Optics 2016*. Optical Society of America, 2016, FF3H.3. URL: <http://www.osapublishing.org/abstract.cfm?URI=FiO-2016-FF3H.3> (56).
- [48] Hari Krishna Bisoyi and Quan Li. *Light-Driven Liquid Crystalline Materials: From Photo-Induced Phase Transitions and Property Modulations to Applications*. **Chemical Reviews** 116 24, 15089–15166, **2016** (67)
URL: <https://doi.org/10.1021/acs.chemrev.6b00415>.
- [49] Bryan Gin-gé Chen, Bin Liu, Arthur A. Evans, Jayson Paulose, Itai Cohen, Vincenzo Vitelli, and C. D. Santangelo. *Topological Mechanics of Origami and Kirigami*. **Phys. Rev. Lett.** 116, 135501, **2016** (32)
URL: <https://link.aps.org/doi/10.1103/PhysRevLett.116.135501>.
- [50] Michel Fruchart. “Topological phases of periodically driven crystals.” Theses. Université de Lyon, 2016. URL: <https://tel.archives-ouvertes.fr/tel-01398614> (52).
- [51] Yubing Guo, Miao Jiang, Chenhui Peng, Kai Sun, Oleg Yaroshchuk, Oleg Lavrentovich, and Qi-Huo Wei. *High-Resolution and High-Throughput Plasmonic Photopatterning of Complex Molecular Orientations in Liquid Crystals*. **Advanced Materials** 28 12, 2353–2358, **2016** (33, 67)
URL: <https://onlinelibrary.wiley.com/doi/abs/10.1002/adma.201506002>.
- [52] Sebastian D. Huber. *Topological mechanics*. **Nature Physics** 12 7, 621–623, **2016** (55)
URL: <https://doi.org/10.1038/nphys3801>.

- [53] Anne S. Meeussen, Jayson Paulose, and Vincenzo Vitelli. *Geared Topological Metamaterials with Tunable Mechanical Stability*. **Phys. Rev. X** 6, 041029, **2016** (32)
URL: <https://link.aps.org/doi/10.1103/PhysRevX.6.041029>.
- [54] Hoi Chun Po, Yasaman Bahri, and Ashvin Vishwanath. *Phonon analog of topological nodal semimetals*. **Phys. Rev. B** 93, 205158, **2016** (32)
URL: <https://link.aps.org/doi/10.1103/PhysRevB.93.205158>.
- [55] D. Zeb Rocklin, Bryan Gin-ge Chen, Martin Falk, Vincenzo Vitelli, and T. C. Lubensky. *Mechanical Weyl Modes in Topological Maxwell Lattices*. **Phys. Rev. Lett.** 116, 135503, **2016** (32)
URL: <https://link.aps.org/doi/10.1103/PhysRevLett.116.135503>.
- [56] Sergei Slussarenko, Alessandro Alberucci, Chandroth P. Jisha, Bruno Piccirillo, Enrico Santamato, Gaetano Assanto, and Lorenzo Marrucci. *Guiding light via geometric phases*. **Nature Photonics** 10 9, 571–575, **2016** (34, 40, 41, 56, 67, 68, 70)
URL: <https://doi.org/10.1038/nphoton.2016.138>.
- [57] Roman Süsstrunk and Sebastian D. Huber. *Classification of topological phonons in linear mechanical metamaterials*. **Proceedings of the National Academy of Sciences** 113 33, E4767–E4775, **2016** (32)
URL: <https://www.pnas.org/content/113/33/E4767>.
- [58] Benjamin C. van Zuiden, Jayson Paulose, William T. M. Irvine, Denis Bartolo, and Vincenzo Vitelli. *Spatiotemporal order and emergent edge currents in active spinner materials*. **Proceedings of the National Academy of Sciences** 113 46, 12919–12924, **2016** (79, 82)
URL: <https://www.pnas.org/content/113/46/12919>.
- [59] Victor V. Albert, Leonid I. Glazman, and Liang Jiang. *Topological Properties of Linear Circuit Lattices*. **Physical Review Letters** 114 17, 173902, **2015** (55)
URL: <https://doi.org/10.1103/physrevlett.114.173902>.
- [60] K. Y. Bliokh, F. J. Rodríguez-Fortuño, F. Nori, and A. V. Zayats. *Spin-orbit interactions of light*. **Nature Photonics** 9 12, 796–808, **2015** (7, 42)
URL: <https://doi.org/10.1038/nphoton.2015.201>.
- [61] Marin Bukov, Luca D’Alessio, and Anatoli Polkovnikov. *Universal high-frequency behavior of periodically driven systems: from dynamical stabilization to Floquet engineering*. **Advances in Physics** 64 2, 139–226, **2015** (10, 34, 39, 50, 61, 74)
URL: <https://doi.org/10.1080/00018732.2015.1055918>.

- [62] Pierre A. Deymier, Keith Runge, Nick Swintek, and Krishna Muralidharan. *Torsional topology and fermion-like behavior of elastic waves in phononic structures*. **Comptes Rendus Mécanique** 343 12, 700–711, **2015** (32)
URL: <http://www.sciencedirect.com/science/article/pii/S1631072115000789>.
- [63] Toshikaze Kariyado and Yasuhiro Hatsugai. *Manipulation of Dirac Cones in Mechanical Graphene*. **Scientific Reports** 5 1, 18107, **2015** (13, 14, 25)
URL: <https://doi.org/10.1038/srep18107>.
- [64] Alexander B. Khanikaev, Romain Fleury, S. Hossein Mousavi, and Andrea Alù. *Topologically robust sound propagation in an angular-momentum-biased graphene-like resonator lattice*. **Nature Communications** 6 1, 8260, **2015** (32)
URL: <https://doi.org/10.1038/ncomms9260>.
- [65] L. Lu, Z. Wang, D. Ye, L. Ran, L. Fu, J. D. Joannopoulos, and M. Soljačić. *Experimental observation of Weyl points*. **Science** 349 6248, 622–624, **2015** (67)
URL: <https://doi.org/10.1126/science.aaa9273>.
- [66] T C Lubensky, C L Kane, Xiaoming Mao, A Souslov, and Kai Sun. *Phonons and elasticity in critically coordinated lattices*. **Reports on Progress in Physics** 78 7, 073901, **2015** (9)
URL: <https://doi.org/10.1088/0034-4885/78/7/073901>.
- [67] S. Hossein Mousavi, Alexander B. Khanikaev, and Zheng Wang. *Topologically protected elastic waves in phononic metamaterials*. **Nature Communications** 6 1, 8682, **2015** (32, 55)
URL: <https://doi.org/10.1038/ncomms9682>.
- [68] Lisa M. Nash, Dustin Kleckner, Alismari Read, Vincenzo Vitelli, Ari M. Turner, and William T. M. Irvine. *Topological mechanics of gyroscopic metamaterials*. **Proceedings of the National Academy of Sciences** 112 47, 14495–14500, **2015** (32, 55)
URL: <https://www.pnas.org/content/112/47/14495>.
- [69] Jia Ningyuan, Clai Owens, Ariel Sommer, David Schuster, and Jonathan Simon. *Time- and Site-Resolved Dynamics in a Topological Circuit*. **Physical Review X** 5 2, 021031, **2015** (55)
URL: <https://doi.org/10.1103/physrevx.5.021031>.
- [70] Jayson Paulose, Bryan Gin-ge Chen, and Vincenzo Vitelli. *Topological modes bound to dislocations in mechanical metamaterials*. **Nature Physics** 11 2, 153–156, **2015** (32)
URL: <https://doi.org/10.1038/nphys3185>.

- [71] Jayson Paulose, Anne S. Meeussen, and Vincenzo Vitelli. *Selective buckling via states of self-stress in topological metamaterials*. **Proceedings of the National Academy of Sciences** 112 25, 7639–7644, **2015** (32)
URL: <https://www.pnas.org/content/112/25/7639>.
- [72] Charles Poli, Matthieu Bellec, Ulrich Kuhl, Fabrice Mortessagne, and Henning Schomerus. *Selective enhancement of topologically induced interface states in a dielectric resonator chain*. **Nature Communications** 6 1, 6710, **2015** (31)
URL: <https://doi.org/10.1038/ncomms7710>.
- [73] Roman Süsstrunk and Sebastian D. Huber. *Observation of phononic helical edge states in a mechanical topological insulator*. **Science** 349 6243, 47–50, **2015** (32, 55)
URL: <https://science.sciencemag.org/content/349/6243/47>.
- [74] Pai Wang, Ling Lu, and Katia Bertoldi. *Topological Phononic Crystals with One-Way Elastic Edge Waves*. **Phys. Rev. Lett.** 115, 104302, **2015** (32)
URL: <https://link.aps.org/doi/10.1103/PhysRevLett.115.104302>.
- [75] Meng Xiao, Wen-Jie Chen, Wen-Yu He, and C. T. Chan. *Synthetic gauge flux and Weyl points in acoustic systems*. **Nature Physics** 11 11, 920–924, **2015** (32)
URL: <https://doi.org/10.1038/nphys3458>.
- [76] Zhaoyu Yang, Fei Gao, Xihang Shi, Xiao Lin, Zhen Gao, Yidong Chong, and Baile Zhang. *Topological Acoustics*. **Phys. Rev. Lett.** 114, 114301, **2015** (32)
URL: <https://link.aps.org/doi/10.1103/PhysRevLett.114.114301>.
- [77] Bryan Gin-gu Chen, Nitin Upadhyaya, and Vincenzo Vitelli. *Nonlinear conduction via solitons in a topological mechanical insulator*. **Proceedings of the National Academy of Sciences** 111 36, 13004–13009, **2014** (32)
URL: <https://www.pnas.org/content/111/36/13004>.
- [78] Liang Feng, Zi Jing Wong, Ren-Min Ma, Yuan Wang, and Xiang Zhang. *Single-mode laser by parity-time symmetry breaking*. **Science** 346 6212, 972–975, **2014** (31)
URL: <https://science.sciencemag.org/content/346/6212/972>.
- [79] N. Goldman and J. Dalibard. *Periodically Driven Quantum Systems: Effective Hamiltonians and Engineered Gauge Fields*. **Phys. Rev. X** 4, 031027, **2014** (10, 34, 39, 50)
URL: <https://link.aps.org/doi/10.1103/PhysRevX.4.031027>.

- [80] Álvaro Gómez-León, Pierre Delplace, and Gloria Platero. *Engineering anomalous quantum Hall plateaus and antichiral states with ac fields*. **Phys. Rev. B** 89, 205408, **2014** (61)
URL: <https://link.aps.org/doi/10.1103/PhysRevB.89.205408>.
- [81] Hossein Hodaei, Mohammad-Ali Miri, Matthias Heinrich, Demetrios N. Christodoulides, and Mercedeh Khajavikhan. *Parity-time-symmetric microring lasers*. **Science** 346 6212, 975–978, **2014** (31)
URL: <https://science.sciencemag.org/content/346/6212/975>.
- [82] C. L. Kane and T. C. Lubensky. *Topological boundary modes in isostatic lattices*. **Nature Physics** 10 1, 39–45, **2014** (8, 9, 32)
URL: <https://doi.org/10.1038/nphys2835>.
- [83] Ling Lu, John D. Joannopoulos, and Marin Soljačić. *Topological photonics*. **Nature Photonics** 8, 821–829, **2014** (32, 55, 56)
URL: <https://doi.org/10.1038/nphoton.2014.248>.
- [84] Nanfang Yu and Federico Capasso. *Flat optics with designer metasurfaces*. **Nature Materials** 13 2, 139–150, **2014** (33)
URL: <https://doi.org/10.1038/nmat3839>.
- [85] M. Hafezi, S. Mittal, J. Fan, A. Migdall, and J. M. Taylor. *Imaging topological edge states in silicon photonics*. **Nature Photonics** 7, 1001–1005, **2013** (32, 55)
URL: <https://doi.org/10.1038/nphoton.2013.274>.
- [86] Alexander B. Khanikaev, S. Hossein Mousavi, Wang-Kong Tse, Mehdi Kargarian, Allan H. MacDonald, and Gennady Shvets. *Photonic topological insulators*. **Nature Materials** 12, 233–239, **2013** (32, 55)
URL: <https://doi.org/10.1038/nmat3520>.
- [87] I. Mahboob, K. Nishiguchi, A. Fujiwara, and H. Yamaguchi. *Phonon Lasing in an Electromechanical Resonator*. **Phys. Rev. Lett.** 110, 127202, **2013** (32)
URL: <https://link.aps.org/doi/10.1103/PhysRevLett.110.127202>.
- [88] Mikael C. Rechtsman, Julia M. Zeuner, Yonatan Plotnik, Yaakov Lumer, Daniel Podolsky, Felix Dreisow, Stefan Nolte, Mordechai Segev, and Alexander Szameit. *Photonic Floquet topological insulators*. **Nature** 496, 196–200, **2013** (13, 32, 44, 55, 56, 61, 67, 73, 74)
URL: <https://doi.org/10.1038/nature12066>.
- [89] Henning Schomerus and Nicole Yunger Halpern. *Parity Anomaly and Landau-Level Lasing in Strained Photonic Honeycomb Lattices*. **Phys. Rev. Lett.** 110, 013903, **2013** (13, 31)
URL: <https://link.aps.org/doi/10.1103/PhysRevLett.110.013903>.

- [90] Filippo Casadei, Tommaso Delpero, Andrea Bergamini, Paolo Ermanni, and Massimo Ruzzene. *Piezoelectric resonator arrays for tunable acoustic waveguides and metamaterials*. **Journal of Applied Physics** 112 6, 064902, **2012** (13)
URL: <https://doi.org/10.1063/1.4752468>.
- [91] Liang Feng, Ye-Long Xu, William S. Fegadolli, Ming-Hui Lu, José E. B. Oliveira, Vilson R. Almeida, Yan-Feng Chen, and Axel Scherer. *Experimental demonstration of a unidirectional reflectionless parity-time metamaterial at optical frequencies*. **Nature Materials** 12 2, 108–113, **2012** (66)
URL: <https://doi.org/10.1038/nmat3495>.
- [92] Kenjiro K. Gomes, Warren Mar, Wonhee Ko, Francisco Guinea, and Hari C. Manoharan. *Designer Dirac fermions and topological phases in molecular graphene*. **Nature** 483 7389, 306–310, **2012** (13)
URL: <https://doi.org/10.1038/nature10941>.
- [93] Ming Kang, Tianhua Feng, Hui-Tian Wang, and Jensen Li. *Wave front engineering from an array of thin aperture antennas*. **Opt. Express** 20 14, 15882–15890, **2012** (33)
URL: <http://www.opticsexpress.org/abstract.cfm?URI=oe-20-14-15882>.
- [94] Oleg Yaroshchuk and Yuriy Reznikov. *Photoalignment of liquid crystals: basics and current trends*. **J. Mater. Chem.** 22 2, 286–300, **2012** (67)
URL: <https://doi.org/10.1039/c1jm13485j>.
- [95] Nina Berg, Kira Joel, Miriam Koolyk, and Emil Prodan. *Topological phonon modes in filamentary structures*. **Phys. Rev. E** 83, 021913, **2011** (32)
URL: <https://link.aps.org/doi/10.1103/PhysRevE.83.021913>.
- [96] Xiao-Liang Qi and Shou-Cheng Zhang. *Topological insulators and superconductors*. **Rev. Mod. Phys.** 83, 1057–1110, **2011** (2)
URL: <https://link.aps.org/doi/10.1103/RevModPhys.83.1057>.
- [97] Liang-Yu Wu and Lien-Wen Chen. *An acoustic bending waveguide designed by graded sonic crystals*. **Journal of Applied Physics** 110 11, 114507, **2011** (13)
URL: <https://doi.org/10.1063/1.3664856>.
- [98] Nanfang Yu, Patrice Genevet, Mikhail A. Kats, Francesco Aieta, Jean-Philippe Tetienne, Federico Capasso, and Zeno Gaburro. *Light Propagation with Phase Discontinuities: Generalized Laws of Reflection and Refraction*. **Science** 334 6054, 333–337, **2011** (7, 8)
URL: <https://science.sciencemag.org/content/334/6054/333>.

- [99] F. Guinea, M. I. Katsnelson, and A. K. Geim. *Energy gaps and a zero-field quantum Hall effect in graphene by strain engineering*. **Nature Physics** 6 1, 30–33, **2010** (13, 28)
URL: <https://doi.org/10.1038/nphys1420>.
- [100] M. Z. Hasan and C. L. Kane. *Colloquium: Topological insulators*. **Rev. Mod. Phys.** 82, 3045–3067, **2010** (2, 13, 55, 63, 91)
URL: <https://link.aps.org/doi/10.1103/RevModPhys.82.3045>.
- [101] N. Levy, S. A. Burke, K. L. Meaker, M. Panlasigui, A. Zettl, F. Guinea, A. H. Castro Neto, and M. F. Crommie. *Strain-Induced Pseudo-Magnetic Fields Greater Than 300 Tesla in Graphene Nanobubbles*. **Science** 329 5991, 544–547, **2010** (13)
URL: <https://science.sciencemag.org/content/329/5991/544>.
- [102] Ardavan F. Oskooi, David Roundy, Mihai Ibanescu, Peter Bermel, J.D. Joannopoulos, and Steven G. Johnson. *Meep: A flexible free-software package for electromagnetic simulations by the FDTD method*. **Computer Physics Communications** 181 3, 687–702, **2010** (43)
URL: <http://www.sciencedirect.com/science/article/pii/S001046550900383X>.
- [103] Christian E. Rüter, Konstantinos G. Makris, Ramy El-Ganainy, Demetrios N. Christodoulides, Mordechai Segev, and Detlef Kip. *Observation of parity-time symmetry in optics*. **Nature Physics** 6 3, 192–195, **2010** (66)
URL: <https://doi.org/10.1038/nphys1515>.
- [104] Alexander Szameit and Stefan Nolte. *Discrete optics in femtosecond-laser-written photonic structures*. **Journal of Physics B: Atomic, Molecular and Optical Physics** 43 16, 163001, **2010** (10, 34)
URL: <https://doi.org/10.1088/0953-4075/43/16/163001>.
- [105] Guenter Ahlers, Siegfried Grossmann, and Detlef Lohse. *Heat transfer and large scale dynamics in turbulent Rayleigh-Bénard convection*. **Rev. Mod. Phys.** 81, 503–537, **2009** (79)
URL: <https://doi.org/10.1103/RevModPhys.81.503>.
- [106] Michael Cross and Henry Greenside. *Pattern Formation and Dynamics in Nonequilibrium Systems*. **2009** (79, 80, 91)
URL: <https://webhome.phy.duke.edu/~hsg/pattern-formation-book/>.
- [107] Andrii B. Golovin and Oleg D. Lavrentovich. *Electrically reconfigurable optical metamaterial based on colloidal dispersion of metal nanorods in dielectric fluid*. **Applied Physics Letters** 95 25, 254104, **2009** (67)
URL: <https://doi.org/10.1063/1.3278442>.

- [108] S. Longhi. *Quantum-optical analogies using photonic structures*. **Laser & Photonics Review** 3 3, 243–261, **2009** (10, 34)
URL: <https://doi.org/10.1002/lpor.200810055>.
- [109] Emil Prodan and Camelia Prodan. *Topological Phonon Modes and Their Role in Dynamic Instability of Microtubules*. **Phys. Rev. Lett.** 103, 248101, **2009** (8, 9, 32)
URL: <https://link.aps.org/doi/10.1103/PhysRevLett.103.248101>.
- [110] Konstantin Y. Bliokh, Yuri Gorodetski, Vladimir Kleiner, and Erez Hasman. *Coriolis Effect in Optics: Unified Geometric Phase and Spin-Hall Effect*. **Phys. Rev. Lett.** 101, 030404, **2008** (7, 42)
URL: <https://link.aps.org/doi/10.1103/PhysRevLett.101.030404>.
- [111] Konstantin Y. Bliokh, Avi Niv, Vladimir Kleiner, and Erez Hasman. *Geometrodynamics of spinning light*. **Nature Photonics** 2 12, 748–753, **2008** (7, 42)
URL: <https://doi.org/10.1038/nphoton.2008.229>.
- [112] V.G. Chigrinov, V.M. Kozenkov, and H.S. Kwok. *Photoalignment of Liquid Crystalline Materials: Physics and Applications*. Wiley Series in Display Technology. **2008** (67)
URL: <https://onlinelibrary.wiley.com/doi/book/10.1002/9780470751800>.
- [113] F. D. M. Haldane and S. Raghu. *Possible Realization of Directional Optical Waveguides in Photonic Crystals with Broken Time-Reversal Symmetry*. **Phys. Rev. Lett.** 100, 013904, **2008** (8)
URL: <https://link.aps.org/doi/10.1103/PhysRevLett.100.013904>.
- [114] John D. Joannopoulos, Steven G. Johnson, Joshua N. Winn, and Robert D. Meade. *Photonic Crystals: Molding the Flow of Light (Second Edition)*. **2008** (8, 34)
URL: <https://press.princeton.edu/books/hardcover/9780691124568/photonic-crystals>.
- [115] S. Raghu and F. D. M. Haldane. *Analogs of quantum-Hall-effect edge states in photonic crystals*. **Phys. Rev. A** 78, 033834, **2008** (8)
URL: <https://link.aps.org/doi/10.1103/PhysRevA.78.033834>.
- [116] Tomoyuki Sasaki, Hiroshi Ono, and Nobuhiro Kawatsuki. *Anisotropic photonic structures induced by three-dimensional vector holography in dye-doped liquid crystals*. **Journal of Applied Physics** 104 4, 043524, **2008** (67)
URL: <https://doi.org/10.1063/1.2970172>.
- [117] J. D. Scheel. *The amplitude equation for rotating Rayleigh–Bénard convection*. **Physics of Fluids** 19 10, 104105, **2007** (90)
URL: <https://doi.org/10.1063/1.2785702>.

- [118] L. Marrucci, C. Manzo, and D. Paparo. *Optical Spin-to-Orbital Angular Momentum Conversion in Inhomogeneous Anisotropic Media*. **Phys. Rev. Lett.** *96*, 163905, **2006** (33)
URL: <https://link.aps.org/doi/10.1103/PhysRevLett.96.163905>.
- [119] Innocent Mutabazi, Jose Eduardo Wesfreid, and Etienne Guyon. *Dynamics of Spatio-Temporal Cellular Structures, Henry Bénard Centenary Review*. **2006** (77)
URL: <https://doi.org/10.1007/b106790>.
- [120] Filippus S. Roux. *Geometric phase lens*. **J. Opt. Soc. Am. A** *23* 2, 476–482, **2006** (33)
URL: <http://josaa.osa.org/abstract.cfm?URI=josaa-23-2-476>.
- [121] Takahiro Fukui, Yasuhiro Hatsugai, and Hiroshi Suzuki. *Chern Numbers in Discretized Brillouin Zone: Efficient Method of Computing (Spin) Hall Conductances*. **Journal of the Physical Society of Japan** *74* 6, 1674–1677, **2005** (63)
URL: <https://doi.org/10.1143/JPSJ.74.1674>.
- [122] C. L. Kane and E. J. Mele. *Quantum Spin Hall Effect in Graphene*. **Phys. Rev. Lett.** *95*, 226801, **2005** (13)
URL: <https://link.aps.org/doi/10.1103/PhysRevLett.95.226801>.
- [123] C. L. Kane and E. J. Mele. *Quantum Spin Hall Effect in Graphene*. **Phys. Rev. Lett.** *95*, 226801, **2005** (13)
URL: <https://link.aps.org/doi/10.1103/PhysRevLett.95.226801>.
- [124] Philip Russell. *Photonic Crystal Fibers*. **Science** *299* 5605, 358–362, **2003** (34)
URL: <https://science.sciencemag.org/content/299/5605/358>.
- [125] H. Kawamoto. *The history of liquid-crystal displays*. **Proceedings of the IEEE** *90* 4, 460–500, **2002** (33)
URL: <https://doi.org/10.1109/JPROC.2002.1002521>.
- [126] Jie Liu, Libin Fu, Bi-Yiao Ou, Shi-Gang Chen, Dae-Il Choi, Biao Wu, and Qian Niu. *Theory of nonlinear Landau-Zener tunneling*. **Phys. Rev. A** *66*, 023404, **2002** (93, 94)
URL: <https://link.aps.org/doi/10.1103/PhysRevA.66.023404>.
- [127] David R. Nelson. *Defects and Geometry in Condensed Matter Physics*. **2002** (8)
URL: <http://www.cambridge.org/9780521801591>.
- [128] “Fiber Optics.” In: *Fundamentals of Photonics*. John Wiley Sons, Ltd, 2001. Chap. 8, 272–309. ISBN: 9780471213741. URL: <https://onlineLibrary.wiley.com/doi/abs/10.1002/0471213748.ch8> (34).

- [129] Biao Wu and Qian Niu. *Nonlinear Landau-Zener tunneling*. **Phys. Rev. A** 61, 023402, **2000** (93, 94)
URL: <https://link.aps.org/doi/10.1103/PhysRevA.61.023402>.
- [130] Franco Dalfovo, Stefano Giorgini, Lev P. Pitaevskii, and Sandro Stringari. *Theory of Bose-Einstein condensation in trapped gases*. **Rev. Mod. Phys.** 71, 463–512, **1999** (91)
URL: <https://link.aps.org/doi/10.1103/RevModPhys.71.463>.
- [131] Franco Gori. *Measuring Stokes parameters by means of a polarization grating*. **Opt. Lett.** 24 9, 584–586, **1999** (33)
URL: <http://ol.osa.org/abstract.cfm?URI=ol-24-9-584>.
- [132] Jeff. Hecht. *City of light : the story of fiber optics*. **1999** (43)
URL: <https://nla.gov.au/nla.cat-vn17702>.
- [133] Carl M. Bender and Stefan Boettcher. *Real Spectra in Non-Hermitian Hamiltonians Having PT Symmetry*. **Physical Review Letters** 80 24, 5243–5246, **1998** (64)
URL: <https://doi.org/10.1103/physrevlett.80.5243>.
- [134] Rajendra Bhandari. *Polarization of light and topological phases*. **Physics Reports** 281 1, 1–64, **1997** (2)
URL: <http://www.sciencedirect.com/science/article/pii/S0370157396000294>.
- [135] Martin van Hecke and Wim van Saarloos. *Convection in rotating annuli: Ginzburg-Landau equations with tunable coefficients*. **Phys. Rev. E** 55, R1259–R1262, **1997** (93)
URL: <https://link.aps.org/doi/10.1103/PhysRevE.55.R1259>.
- [136] J. D. Joannopoulos, Pierre R. Villeneuve, and Shanhui Fan. *Photonic crystals: putting a new twist on light*. **Nature** 386, 143–149, **1997** (8, 34)
URL: <https://doi.org/10.1038/386143a0>.
- [137] A. Smerzi, S. Fantoni, S. Giovanazzi, and S. R. Shenoy. *Quantum Coherent Atomic Tunneling between Two Trapped Bose-Einstein Condensates*. **Phys. Rev. Lett.** 79, 4950–4953, **1997** (94)
URL: <https://link.aps.org/doi/10.1103/PhysRevLett.79.4950>.
- [138] P. M. Chaikin and T. C. Lubensky. *Principles of Condensed Matter Physics*. **1995** (8)
URL: <https://doi.org/10.1017/CB09780511813467>.
- [139] T.J. Shepherd. *Full 2-D photonic bandgaps in silica/air structures*. **Electronics Letters** 31, 1941–1943(2), **1995** (34)
URL: https://digital-library.theiet.org/content/journals/10.1049/eL_19951306.

- [140] M. C. Cross and P. C. Hohenberg. *Pattern formation outside of equilibrium*. **Rev. Mod. Phys.** 65, 851–1112, **1993** (11, 79–81, 88)
URL: <https://link.aps.org/doi/10.1103/RevModPhys.65.851>.
- [141] Pierre-Gilles De Gennes and Jacques Prost. *The Physics of Liquid Crystals*. **1993** (33, 34)
URL: <https://doi.org/10.1063/1.2808028>.
- [142] R. E Ecke, Fang Zhong, and E Knobloch. *Hopf Bifurcation with Broken Reflection Symmetry in Rotating Rayleigh-Bénard Convection*. **Europhysics Letters (EPL)** 19 3, 177–182, **1992** (79, 81)
URL: <https://doi.org/10.1209%2F0295-5075%2F19%2F3%2F005>.
- [143] K. R. Elder, Jorge Viñals, and Martin Grant. *Dynamic scaling and quasicrystalline states in the two-dimensional Swift-Hohenberg equation*. **Phys. Rev. A** 46, 7618–7629, **1992** (80)
URL: <https://link.aps.org/doi/10.1103/PhysRevA.46.7618>.
- [144] M. A. Ablowitz and P. A. Clarkson. *Solitons, Nonlinear Evolution Equations and Inverse Scattering*. London Mathematical Society Lecture Note Series. **1991** (91)
URL: <https://doi.org/10.1017/CB09780511623998>.
- [145] Eberhard Bodenschatz, John R. de Bruyn, Guenter Ahlers, and David S. Cannell. *Transitions between patterns in thermal convection*. **Phys. Rev. Lett.** 67, 3078–3081, **1991** (81)
URL: <https://link.aps.org/doi/10.1103/PhysRevLett.67.3078>.
- [146] Fang Zhong, Robert Ecke, and Victor Steinberg. *Asymmetric modes and the transition to vortex structures in rotating Rayleigh-Bénard convection*. **Phys. Rev. Lett.** 67, 2473–2476, **1991** (79)
URL: <https://link.aps.org/doi/10.1103/PhysRevLett.67.2473>.
- [147] Alfred Shapere and Frank Wilczek. *Gauge kinematics of deformable bodies*. **American Journal of Physics** 57 6, 514–518, **1989** (1)
URL: <https://doi.org/10.1119/1.15986>.
- [148] Alfred Shapere and Frank Wilczek. *Geometric phases in physics*. **1989** (2)
URL: <https://doi.org/10.1142/0613>.
- [149] J. Zak. *Berry's phase for energy bands in solids*. **Phys. Rev. Lett.** 62, 2747–2750, **1989** (85)
URL: <https://link.aps.org/doi/10.1103/PhysRevLett.62.2747>.
- [150] M V Berry and J H Hannay. *Classical non-adiabatic angles*. **Journal of Physics A: Mathematical and General** 21 6, L325–L331, **1988** (6)
URL: <https://doi.org/10.1088%2F0305-4470%2F21%2F6%2F002>.

- [151] F. D. M. Haldane. *Model for a Quantum Hall Effect without Landau Levels: Condensed-Matter Realization of the "Parity Anomaly"*. **Phys. Rev. Lett.** 61, 2015–2018, **1988** (10, 56, 61)
URL: <https://doi.org/10.1103/PhysRevLett.61.2015>.
- [152] R. Jackiw. *Three Elaborations on Berry's Connection, Curvature and Phase*. **International Journal of Modern Physics A** 03 02, 285–297, **1988** (3)
URL: <https://doi.org/10.1142/S0217751X88000114>.
- [153] R. B. Laughlin. *Superconducting Ground State of Noninteracting Particles Obeying Fractional Statistics*. **Phys. Rev. Lett.** 60, 2677–2680, **1988** (2)
URL: <https://link.aps.org/doi/10.1103/PhysRevLett.60.2677>.
- [154] Christopher W. Meyer, David S. Cannell, Guenter Ahlers, J. B. Swift, and P. C. Hohenberg. *Pattern Competition in Temporally Modulated Rayleigh-Bénard Convection*. **Phys. Rev. Lett.** 61, 947–950, **1988** (8i)
URL: <https://link.aps.org/doi/10.1103/PhysRevLett.61.947>.
- [155] M.V. Berry. *The Adiabatic Phase and Pancharatnam's Phase for Polarized Light*. **Journal of Modern Optics** 34 11, 1401–1407, **1987** (1, 2, 7, 56)
URL: <https://doi.org/10.1080/09500348714551321>.
- [156] D. R. Jenkins. *Rolls versus squares in thermal convection of fluids with temperature-dependent viscosity*. **Journal of Fluid Mechanics** 178, 491–506, **1987** (89)
URL: <https://doi.org/10.1017/S0022112087001332>.
- [157] Klaus von Klitzing. *The quantized Hall effect*. **Rev. Mod. Phys.** 58, 519–531, **1986** (2)
URL: <https://link.aps.org/doi/10.1103/RevModPhys.58.519>.
- [158] L.M. Pismen. *Inertial effects in long-scale thermal convection*. **Physics Letters A** 116 5, 241–244, **1986** (82)
URL: <http://www.sciencedirect.com/science/article/pii/0375960186901416>.
- [159] M V Berry. *Classical adiabatic angles and quantal adiabatic phase*. **Journal of Physics A: Mathematical and General** 18 1, 15–27, **1985** (2)
URL: <https://doi.org/10.1088%2F0305-4470%2F18%2F1%2F012>.
- [160] J H Hannay. *Angle variable holonomy in adiabatic excursion of an integrable Hamiltonian*. **Journal of Physics A: Mathematical and General** 18 2, 221–230, **1985** (2, 6)
URL: <https://doi.org/10.1088%2F0305-4470%2F18%2F2%2F011>.

- [161] Michael Victor Berry. *Quantal phase factors accompanying adiabatic changes*. **Proceedings of the Royal Society of London. A. Mathematical and Physical Sciences** 392 1802, 45–57, **1984** (1, 56)
URL: <https://royalsocietypublishing.org/doi/abs/10.1098/rspa.1984.0023>.
- [162] H. S. Greenside and W. M. Coughran. *Nonlinear pattern formation near the onset of Rayleigh-Bénard convection*. **Phys. Rev. A** 30, 398–428, **1984** (80)
URL: <https://link.aps.org/doi/10.1103/PhysRevA.30.398>.
- [163] R. Jackiw. *Fractional charge and zero modes for planar systems in a magnetic field*. **Phys. Rev. D** 29, 2375–2377, **1984** (19, 28, 86)
URL: <https://link.aps.org/doi/10.1103/PhysRevD.29.2375>.
- [164] D. R. Jenkins and M. R. E. Proctor. *The transition from roll to square-cell solutions in Rayleigh-Bénard convection*. **Journal of Fluid Mechanics** 139, 461–471, **1984** (89)
URL: <https://doi.org/10.1017/S0022112084000458>.
- [165] Gordon W. Semenoff. *Condensed-Matter Simulation of a Three-Dimensional Anomaly*. **Phys. Rev. Lett.** 53, 2449–2452, **1984** (19)
URL: <https://link.aps.org/doi/10.1103/PhysRevLett.53.2449>.
- [166] J. E. Avron, R. Seiler, and B. Simon. *Homotopy and Quantization in Condensed Matter Physics*. **Phys. Rev. Lett.** 51, 51–53, **1983** (2)
URL: <https://link.aps.org/doi/10.1103/PhysRevLett.51.51>.
- [167] Barry Simon. *Holonomy, the Quantum Adiabatic Theorem, and Berry's Phase*. **Phys. Rev. Lett.** 51, 2167–2170, **1983** (4)
URL: <https://link.aps.org/doi/10.1103/PhysRevLett.51.2167>.
- [168] T. Suhara, K. Kobayashi, H. Nishihara, and J. Koyama. *Graded-index Fresnel lenses for integrated optics*. **Appl. Opt.** 21 11, 1966–1971, **1982** (34)
URL: <http://ao.osa.org/abstract.cfm?URI=ao-21-11-1966>.
- [169] D. J. Thouless, M. Kohmoto, M. P. Nightingale, and M. den Nijs. *Quantized Hall Conductance in a Two-Dimensional Periodic Potential*. **Phys. Rev. Lett.** 49, 405–408, **1982** (2, 6, 63)
URL: <https://link.aps.org/doi/10.1103/PhysRevLett.49.405>.
- [170] K. v. Klitzing, G. Dorda, and M. Pepper. *New Method for High-Accuracy Determination of the Fine-Structure Constant Based on Quantized Hall Resistance*. **Phys. Rev. Lett.** 45, 494–497, **1980** (2, 5, 6)
URL: <https://link.aps.org/doi/10.1103/PhysRevLett.45.494>.
- [171] N. D. Mermin. *The topological theory of defects in ordered media*. **Rev. Mod. Phys.** 51, 591–648, **1979** (8)
URL: <https://link.aps.org/doi/10.1103/RevModPhys.51.591>.

- [172] W. P. Su, J. R. Schrieffer, and A. J. Heeger. *Solitons in Polyacetylene*. **Phys. Rev. Lett.** 42, 1698–1701, **1979** (10, 21, 23, 32, 56, 58, 60, 81, 91)
URL: <https://link.aps.org/doi/10.1103/PhysRevLett.42.1698>.
- [173] M V Berry and J H Hannay. *Umbilic points on Gaussian random surfaces*. **Journal of Physics A: Mathematical and General** 10 11, 1809–1821, **1977** (8)
URL: <https://doi.org/10.1088%2F0305-4470%2F10%2F11%2F009>.
- [174] J. Swift and P. C. Hohenberg. *Hydrodynamic fluctuations at the convective instability*. **Phys. Rev. A** 15, 319–328, **1977** (11, 80)
URL: <https://link.aps.org/doi/10.1103/PhysRevA.15.319>.
- [175] R. Jackiw and C. Rebbi. *Solitons with fermion number $\frac{1}{2}$* . **Phys. Rev. D** 13, 3398–3409, **1976** (21, 23, 86, 87)
URL: <https://link.aps.org/doi/10.1103/PhysRevD.13.3398>.
- [176] Hideo Samba. *Steady States and Quasienergies of a Quantum-Mechanical System in an Oscillating Field*. **Phys. Rev. A** 7, 2203–2213, **1973** (52)
URL: <https://link.aps.org/doi/10.1103/PhysRevA.7.2203>.
- [177] A. Yariv. *Coupled-mode theory for guided-wave optics*. **IEEE Journal of Quantum Electronics** 9 9, 919–933, **1973** (56)
URL: <https://doi.org/10.1109/jqe.1973.1077767>.
- [178] Alan C. Newell and J. A. Whitehead. *Finite bandwidth, finite amplitude convection*. **Journal of Fluid Mechanics** 38 2, 279–303, **1969** (91)
URL: <https://doi.org/10.1017/S0022112069000176>.
- [179] H. T. Rossby. *A study of Bénard convection with and without rotation*. **Journal of Fluid Mechanics** 36 2, 309–335, **1969** (79)
URL: <https://doi.org/10.1017/S00221120690001674>.
- [180] F. H. Busse. *The stability of finite amplitude cellular convection and its relation to an extremum principle*. **Journal of Fluid Mechanics** 30 4, 625–649, **1967** (81)
URL: <https://doi.org/10.1017/S0022112067001661>.
- [181] A. Schlüter, D. Lortz, and F. Busse. *On the stability of steady finite amplitude convection*. **Journal of Fluid Mechanics** 23 1, 129–144, **1965** (81, 89)
URL: <https://doi.org/10.1017/S0022112065001271>.
- [182] Jon H. Shirley. *Solution of the Schrödinger Equation with a Hamiltonian Periodic in Time*. **Phys. Rev.** 138, B979–B987, **1965** (40)
URL: <https://link.aps.org/doi/10.1103/PhysRev.138.B979>.
- [183] R. G. Chambers. *Shift of an Electron Interference Pattern by Enclosed Magnetic Flux*. **Phys. Rev. Lett.** 5, 3–5, **1960** (2)
URL: <https://link.aps.org/doi/10.1103/PhysRevLett.5.3>.

- [184] Enok Palm. *On the tendency towards hexagonal cells in steady convection.* **Journal of Fluid Mechanics** 8 2, 183–192, **1960** (81)
URL: <https://doi.org/10.1017/S0022112060000530>.
- [185] Y. Aharonov and D. Bohm. *Significance of Electromagnetic Potentials in the Quantum Theory.* **Phys. Rev.** 115, 485–491, **1959** (1, 2)
URL: <https://link.aps.org/doi/10.1103/PhysRev.115.485>.
- [186] S. Pancharatnam. *Generalized theory of interference, and its applications.* **Proceedings of the Indian Academy of Sciences - Section A** 44 5, 247–262, **1956** (1, 2, 6, 56)
URL: <https://doi.org/10.1007/BF03046050>.
- [187] Shiing-shen Chern. *On the Curvatura Integra in a Riemannian Manifold.* **Annals of Mathematics** 46 4, 674–684, **1945** (6)
URL: <http://www.jstor.org/stable/1969203>.
- [188] V.V. Vladimirkii. *The rotation of polarization plane for curved light ray.* **Dokl. Akad. Nauk. USSR** 21, 222, **1941** (7, 56).
- [189] S.M. Rytov. *Transition from wave to geometrical optics.* **Dokl. Akad. Nauk. USSR XVIII**, 263, **1938** (7, 56).
- [190] Conyers Herring. *Accidental Degeneracy in the Energy Bands of Crystals.* **Phys. Rev.** 52, 365–373, **1937** (25)
URL: <https://link.aps.org/doi/10.1103/PhysRev.52.365>.
- [191] Erich Hückel. *Quantentheoretische Beiträge zum Benzolproblem.* **Zeitschrift für Physik** 70 3, 204–286, **1931** (58)
URL: <https://doi.org/10.1007/BF01339530>.
- [192] Lev Shubnikov and Wander Johannes de Haas. *Magnetische Widerstandsvergrößerung in Einkristallen von Wismut bei tiefen Temperaturen.* **Comm. Phys. Lab. Univ. Leiden** 207a, 3–6, **1930** (32)
URL: <https://www.dwc.knaw.nl/DL/publications/PU00015868.pdf>.
- [193] Paul Adrien Maurice Dirac and Ralph Howard Fowler. *The quantum theory of the electron.* **Proceedings of the Royal Society of London. Series A, Containing Papers of a Mathematical and Physical Character** 117 778, 610–624, **1928** (9)
URL: <https://royalsocietypublishing.org/doi/abs/10.1098/rspa.1928.0023>.

Summary

Geometric phases lead to a nontrivial interference result when an electron's different quantum mechanical paths choices encircle a magnetic coil in an Aharonov-Bohm experiment. They are also responsible for the daily precession of a Foucault pendulum in Paris. A dynamical shape change induces a geometric phase, which, for instance, cats use to rotate when falling and swimmers use to swim forward. A modern application of such geometric phases has led to the notion of topological phases, which are described by a global property of the system. These phases are very different from the classical phases of matter, which are characterized by a local order parameter. A topological phase transition is therefore a fundamentally different process compared to a classical one as in a liquid-gas transition, because the former requires a change of a global topological index of the system. Topological phases can, for example, lead to the presence of traveling electronic modes which are robust against being backscattered by obstacles at the boundary of an insulator. This thesis describes some applications of geometric and topological phases in soft-matter systems.

Chapter 2 focuses on a mechanical metamaterial which is modeled as a network of beads that are connected by means of elastic rods. A designer shape deformation or a spatial variation of the elastic modulus is shown to lead to topologically nonequivalent states in such systems. A boundary between two such nonequivalent systems is predicted to host a domain-bound vibrational mode. This mode amounts to half of the beads vibrating, while the other half are nearly stationary through breaking of a sublattice symmetry of such modes. An application of such a phenomenon is presented as a recipe to enhance this topological mode over all other vibrational modes of the system by damping the vibrations of the second half of the beads. A specific case of such domain-bound modes is extracted as a zeroth Landau-level state by a formulation that maps the dynamical evolution of the vibrational modes of this system to the quantum-mechanical motion of an electron in a magnetic field.

The third and fourth chapters study the light propagation in a liquid-crystal medium. Liquid crystals are complex fluids that combine a unique ability to manipulate light with the reconfigurability of soft materials. They are at the core of modern display technology. Chapter 3 exploits a spatially varying nematic pattern in such systems to find light waveguides that act similar to an optical fiber. An explanation of such waveguiding regimes is through a modifying term to Snell's refraction law due to a spatial inhomogeneity of the geometric Pancharatnam-Berry phase that light acquires by passing through a liquid crystal medium.

Chapter 4 suggests that nematic liquid crystals can also be used as building blocks of topological materials that are key to realize protected unidirectional waveguides, sensors and lasers. Building on recent advances in liquid-crystal technology, it proposes that suitable spatial modulations of the nematic director field are sufficient to assemble topological photonic materials. These ideas pave the way for fully reconfigurable photonic devices based on topologically protected states.

Chapter 5 shifts the focus to convective hydrodynamic systems. Rotating Rayleigh-Bénard experiments as a prototypical model of rotating convective systems are analyzed and the results of an ongoing study on the topological origin of the so-called wall modes in such systems are presented. Simulations of a simplified Swift-Hohenberg model shows wall modes that are robust against severe boundary changes. A linearization of this model around its non-equilibrium steady state in one dimension shows signatures of the topological origin of this protection against backscattering through a non-trivial topological index. A full description of such an out-of-equilibrium system requires a generalization of this topological index for nonlinear models.

Samenvatting

In een Aharonov-Bohm experiment leiden geometrische fasen tot niet-triviale interferentie wanneer de verschillende kwantummechanische paden van een elektron een magnetische spoel omringen. Deze zijn ook verantwoordelijk voor de dagelijkse precessie van de Foucault slinger in Parijs. Een dynamische vormverandering veroorzaakt een geometrische fase die bijvoorbeeld katten gebruiken om te draaien als ze vallen of zwemmers gebruiken om vooruit te zwemmen. Een moderne toepassing van de geometrische fase heeft tot het begrip geleid van een topologische fase, die door een globale eigenschap van het systeem wordt beschreven. Deze topologische fase is iets heel anders dan het klassieke begrip van de fase van materie die wordt gekenmerkt door een lokale ordeparameter. Een topologische faseovergang is daarom een fundamenteel ander proces vergeleken met een klassieke, zoals bijvoorbeeld een vloeistof-gasovergang, omdat bij de eerste een globale topologische index van het systeem moet veranderen. Topologische fasen kunnen bijvoorbeeld ook leiden tot de aanwezigheid van zich voortplantende elektronische modes die robuust zijn tegen terugverstrooiing door obstakels op de grens van een isolator. Dit proefschrift beschrijft enkele toepassingen van geometrische en topologische fasen in zogenaamde zachte-materie systemen.

Hoofdstuk twee richt zich op een mechanisch metamateriaal dat gemodelleerd wordt als een netwerk van kralen die door elastische staven verbonden zijn. Een slim ontworpen vervorming of een ruimtelijke variatie van de elasticiteitsmodulus blijkt tot topologisch niet-equivalente toestanden in dergelijke systemen te leiden. Er wordt voorspeld dat de grens tussen twee van dergelijke niet-equivalente systemen een domeingebonden trillingsmode herbergt. Het komt erop neer dat in deze mode de helft van de kralen trilt, terwijl de andere helft bijna stationair is, een gevolg van het breken van een subrooster-symmetrie. Als toepassing van een dergelijk fenomeen wordt voorgesteld om deze topologische mode ten opzichte van alle andere vibratiemodes van het systeem te versterken door de demping van de trillingen van de tweede helft van de kralen te vergroten. Een specifiek geval van zo een domeingebonden

mode blijkt equivalent aan het nulde Landau-niveau, in een formulering die de dynamische evolutie van de vibratiemodes van een dergelijk systeem afbeeldt op de kwantummechanische beweging van een elektron in een magnetisch veld.

In het derde en vierde hoofdstuk beschrijf ik de voortplanting van licht in een vloeibaar kristal medium. Vloeibare kristallen zijn complexe vloeistoffen die een uniek vermogen hebben om licht met behulp van de herconfigureerbaarheid van zachte materialen te manipuleren. Ze staan aan de basis van moderne beeldscherm technologie. Hoofdstuk drie maakt gebruik van een ruimtelijk variërend nematisch patroon in dergelijke systemen om lichtgolfgeluiders te vinden die vergelijkbaar zijn met een optische fiber. De golfgeleiding kan verklaard worden door een term aan te passen in de brekingswet van Snellius als gevolg van een ruimtelijke inhomogeniteit van de geometrische Pancharatnam-Berry fase die het licht verkrijgt als het door een vloeibaar kristalmedium heen gaat.

Hoofdstuk vier suggereert dat nematische vloeibare kristallen ook kunnen worden gebruikt als bouwstenen van topologische materialen om beschermde éénrichtings-golfgeluiders, sensoren en lasers te realiseren. Op basis van recente ontwikkelingen in de vloeibaarkristaltechnologie, stellen we voor dat geschikte ruimtelijke modulaties van de nematische as voldoende zijn om topologische fotonische materialen samen te stellen. Deze ideeën kunnen de weg banen voor volledig instelbare fotonische structuren op basis van topologisch beschermde toestanden.

Hoofdstuk vijf focust op convectieve hydrodynamische systemen. Draaiende Rayleigh-Bénard vloeistoffen kunnen als een prototypisch model van roterende convectie systemen worden geanalyseerd en de resultaten van een studie naar de topologische oorsprong van de zogenaamde wand modes in dergelijke systemen worden gepresenteerd. Simulaties van een vereenvoudigd Swift-Hohenberg model tonen wand modes die goed tegen ernstige grensveranderingen kunnen. Een linearisatie van dit model rond zijn niet-evenwicht stabiele toestand in één dimensie toont signaturen van de topologische oorsprong van deze bescherming tegen terugverstrooiing in de vorm van een niet-triviale topologische index. Een volledige beschrijving van een dergelijk systeem dat niet in evenwicht is, vereist een generalisatie van deze topologische index voor niet-lineaire modellen.

List of publications

- ▶ Hamed Abbaszadeh, Michel Fruchart, Wim van Saarloos, and Vincenzo Vitelli. *Liquid-crystal-based topological photonics*, ***Proceedings of the National Academy of Science (in press)***. arXiv: 2005.02476.
[Chapters 3 and 4].
- ▶ Hamed Abbaszadeh, Anton Souslov, Jayson Paulose, Henning Schomerus, and Vincenzo Vitelli. *Sonic Landau Levels and Synthetic Gauge Fields in Mechanical Metamaterials*. **Phys. Rev. Lett.** 119, 195502, **2017**.
URL: <https://link.aps.org/doi/10.1103/PhysRevLett.119.195502>.
[Chapter 2].

Curriculum vitæ

I was born in 1991 in Amol, Iran. I stayed in my hometown until the end of high school. During the third year of high school I participated in the National Physics Olympiad, for which I received a silver medal.

In 2009, I moved to Tehran, Iran and started my bachelor studies at Sharif University of Technology, where five years later, I graduated with honors with a double major in Physics and Mathematics. During my fourth year, I won a gold medal at the National Collegiate Physics Olympiad. I have also spent most of the weekends in these years to prepare high-school students for the physics olympiads in various places in Iran.

In 2014, I joined the MSc program in theoretical physics at Leiden University with a LExS Platinum scholarship. With great joy I moved to Leiden, where I have spent most of the past 6 years of my life. For my master thesis, I joined the Soft-Matter theory group of Prof. Vincenzo Vitelli, and worked on mechanical analogues of Landau levels. In 2016, I graduated *cum laude* for the MSc degree, and continued in Prof. Vitelli's group in Leiden as a PhD candidate. During the four years of my PhD, I have attended schools and seminars in the Netherlands, Germany, Italy, and the United States. Since prof. Vitelli moved to the University of Chicago in the fall of 2017, I have spent the fall quarter of 2019 in his new group at the James Franck Institute as a visiting graduate student.

During my bachelor and PhD I was a teaching assistant for courses in Statistical Physics and Theory of General Relativity. After my PhD, I will stay at Leiden Institute of Physics as a postdoctoral researcher and a tutor for the MSc physics program.

Acknowledgments

I would like to express my gratitude and respect for my supervisors, Vincenzo Vitelli and Wim van Saarloos. Vincenzo, your passion for physics and your originality have always been an inspiration. Wim, your care helped me pass through quite a few bottlenecks during the past years. I have been astounded about how you always managing to find time for me.

Chapters three, four, and five of this thesis were done under supervision of Michel Fruchart. Michel, I was fortunate to have you as my daily supervisor during your time in Leiden, and I missed that after you moved to Chicago. You indeed have a way of seeing things from viewpoints which are both precise and different, and the last four years have been a great opportunity for me to learn from you.

Chapter two of this thesis was done under supervision of Anton Souslov and Jayson Paulose. Jayson and Anton, I enjoyed very much my first experience in exploring a research question under your guidance.

I would like to thank Eric Eliel for helping me to address some of the important questions regarding my career. It is still ongoing, and I hope it will settle to a job that includes love and passion.

I appreciate the interaction with the members of the Vitelli group, both in Leiden and Chicago. Benny, thanks for being in touch about my progress, and also for providing me with the \LaTeX typeset of this thesis. I thank Debu and Ming for giving me more insights about the academic career, and Colin, Jonathan, Richard, and Ryo for interesting discussions.

I would like to thank the Lorentz Institute for hosting me during these years. Fran, you have always been a great help for the formal aspects of this job which I still have to learn well. I appreciate helps from Leonardo Lenoci and the (X)maris cluster, which played a crucial role in a major part of the results in the third and fourth chapters.

Life in Netherlands and Chicago has brought me in contact with many good friends, all of whom I look forward to seeing again after the Covid-19 restrictions. I especially thank Ehsan, Emad, and Saeid for the dialogues between us which have opened up new insights about how things work. I appreciate memorable times (which usually accompanied delicious foods) from Qi, Ireth, and Bahareh.

Many thanks to my Dutch family, Debbie and Youssef, for treating me as part of their family and being there in my life events.

My gratitude goes to my family of origin. Your support and love from far away have always been a major source of encouragement for me. Reaching to a point where I can help you all stays as a strong motivation in me.

In the end, I thank you my dearest Hamraz. It has been such a great adventure of life with you. This thesis in the current format owes a lot to you. I love growing alongside you and I am happy with your presence.